Curved crystal surfaces:
fabrication, characterization and growth of cobalt nanostructures

ANA MAGAÑA

2015

eman ta zabal zazu
Universidad del País Vasco
Euskal Herriko Unibertsitatea

Contents

Introduction

This work was aimed to develop the technology of polishing metallic single crystals to obtain shallow cylindrical segments and use such curved crystals to study the microstructure of their surfaces, the mode of growth of the cobalt overlayers and their magnetic properties.

Well-prepared surfaces of metallic or semiconducting single-crystal materials cut parallel to one of the low-index crystallographic planes consist of wide atomically flat terraces. The average area of these terraces depends on the density of the surface defects (atomic steps). The height of the atomic steps is an integer multiple of the distance between the atomic planes comprising the terraces while the shape and the average distance between the steps depends on many factors, especially on the crystallographic orientation of the surface and the way it is prepared [1-3].

Atomic steps are interesting objects playing important role in many surface phenomena. For example, atomic steps can catalyze various chemical processes [4,5] or affect the growth of other materials on the surfaces [6,7]. Detailed study of the atomic steps is more convenient if the steps are not distributed randomly but ordered in some periodic structure. A vicinal surface features arrays of parallel (in average), uniformly separated atomic steps [8,9]. In practice, it is fabricated by cutting at small (miscut) angle from the low-index crystallographic plane. Its stepped shape appears owing to the spontaneous reconstruction which lowers the surface free energy [1-3]. The average step-step distance on the vicinal surface is defined by the miscut angle (it is bigger when the miscut angle is smaller).

Since many properties of vicinal surfaces depend on the average step separation, their experimental investigation may be accomplished using a series of samples having different miscut angles. Nevertheless, a single sample polished in a smooth cylindrical shape features various vicinal surfaces, which is very convenient for experimental investigation of the step arrays. Curved crystals were punctually used to study electronic [10,11] and catalytic [12-14] properties, or the effect of the steps of the substrate on the magnetic properties of thin films and small clusters [15-17].

Two curved crystals have been polished for this work: cPd(111)and cNi(111). Both of these metals have face-centered cubic (fcc) crystal structure. The shaping was performed so that the terraces comprising a vicinal surface are made of (111) atomic planes and the steps run along one of the densely packed atomic rows ($[\bar{1}10]$ direction). This orientation favors formation of the straight atomic steps.

cNi(111) and cPd(111) were chosen to study their clean vicinal surfaces which can be used for further investigation of the electronic and catalytic properties [18-20], and because of their suitability for the growth of the Co nanostructures with out-of-plane (OOP) magnetic anisotropy [21-23].

Since the oblate magnetic objects have a shape anisotropy, which is stronger than the usual magnetocrystalline anisotropy and favors the in-plane orientation of the magnetic moment, the OOP anisotropy usually observed in some systems reveals the presence of the additional contribution. It was shown that ultrathin (few atomic monolayers (ML) thick) cobalt and iron films epitaxially grown on various metallic surfaces possess the OOP anisotropy. The origin of this anisotropy is still not understood completely. Some authors attribute it to the altered splitting of the atomic orbitals of Co and Fe in the crystal field of the reduced symmetry (a size effect). Meanwhile another reason can be a stress generated in the epilayers due to the lattice mismatch between the film and the substrate (interface effect) [21].

The lattice cell of fcc Co is bigger than the cell of Ni and smaller than the cell of Pd. The lattice mismatch in the case of Co/Pd(111) amounts to 9.1% [23], while it is less than 1% for the Co/Ni(111) [22]. Cobalt grows on flat Ni(111) in a layer-by-layer mode, but a three-dimensional growth was reported for the Co/Pd(111) system [22, 23]. Ascending atomic steps of the substrate are the places of preferential adsorption for both of these systems (because of higher coordination of the adatom at the step than on the terrace) which favors a step-decoration growth mode of Co on the stepped surfaces of Pd(111) and Ni(111). Since for the constant effective coverage the amount of Co per unit length of the atomic step decreases with decreasing width of the terraces, using of the curved crystals allows to achieve a smooth change of the dimensionality of the Co nanostructures from 2D islands on the wide terraces to the 1D stripes in the narrow terraces at higher miscut angles. At the same time utilization of the substrates with different lattice mismatch gives a possibility to trace the effect of stress on the magnetic properties of Co nanostructures.

This thesis is organized in the next way: following the Introduction, the second part presents the experimental techniques and necessary theoretical background. The polishing procedure is described in the third part. The fourth part summarizes properties of the clean surfaces of the cPd(111) and cNi(111). The fifth part presents details of Co growth, and its magnetic properties are reported in the sixth part.

2.1 Vicinal surfaces

The boundary between a solid and a fluid (or vacuum) phases is called surface. The main parameter defining the majority of its properties is the surface free energy γ. It represents an excess of free energy per unit area and it can be defined as the reversible work required for the formation of a unit area of a surface or interface while the crystal volume and number of constituent atoms are kept constant [1].

The surface free energy γ of crystals can be represented as a function of the orientation of the plane (hkl) by means of the so-called Wulff plot [24]. Originally it was used to find graphically the Equilibrium Crystal Shape (ECS). The 2D Wulff construction is a polar plot (figure 2.1) of the scalar surface energy γ(hkl) as a function of the angle θ, which represents the angle between a fixed direction and the normal direction to the (hkl) plane. It turns out that the atomic planes which make up an inner envelope of the Wulff plot meet the condition

$$\int \gamma(hkl)dA = minimum$$

known as the Wulff theorem, and therefore, only these planes compose the surface of the crystal in equilibrium. For example scanning electron microscopy images of the pure nickel crystals have revealed that its equilibrium crystal shape is a polyhedron composed of {111}, {110}, {110}, {210} and {320} sharp surfaces (see figure 2.2).

Figure 2.1 shows that surface energy depends on the crystallographic orientation of the surface. The points of minimum of this plot correspond to the low index surfaces and any other surfaces have higher surface energy. This simple fact has important consequences in the case of the vicinal surfaces (a crystal surface cut at small (miscut) angle to the low index crystallographic plane). It turns out that in many cases the energy of the vicinal atomic plane is higher than the energy of the stepped surface which has the same average orientation and consists of the terraces of the nearest low

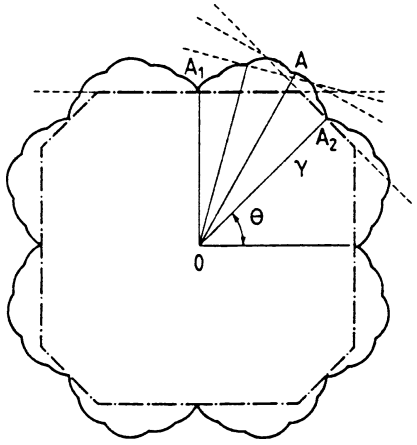

Figure 2.1: Diagram illustrates the Wulf construction and determination of the ECS of a crystal [24].

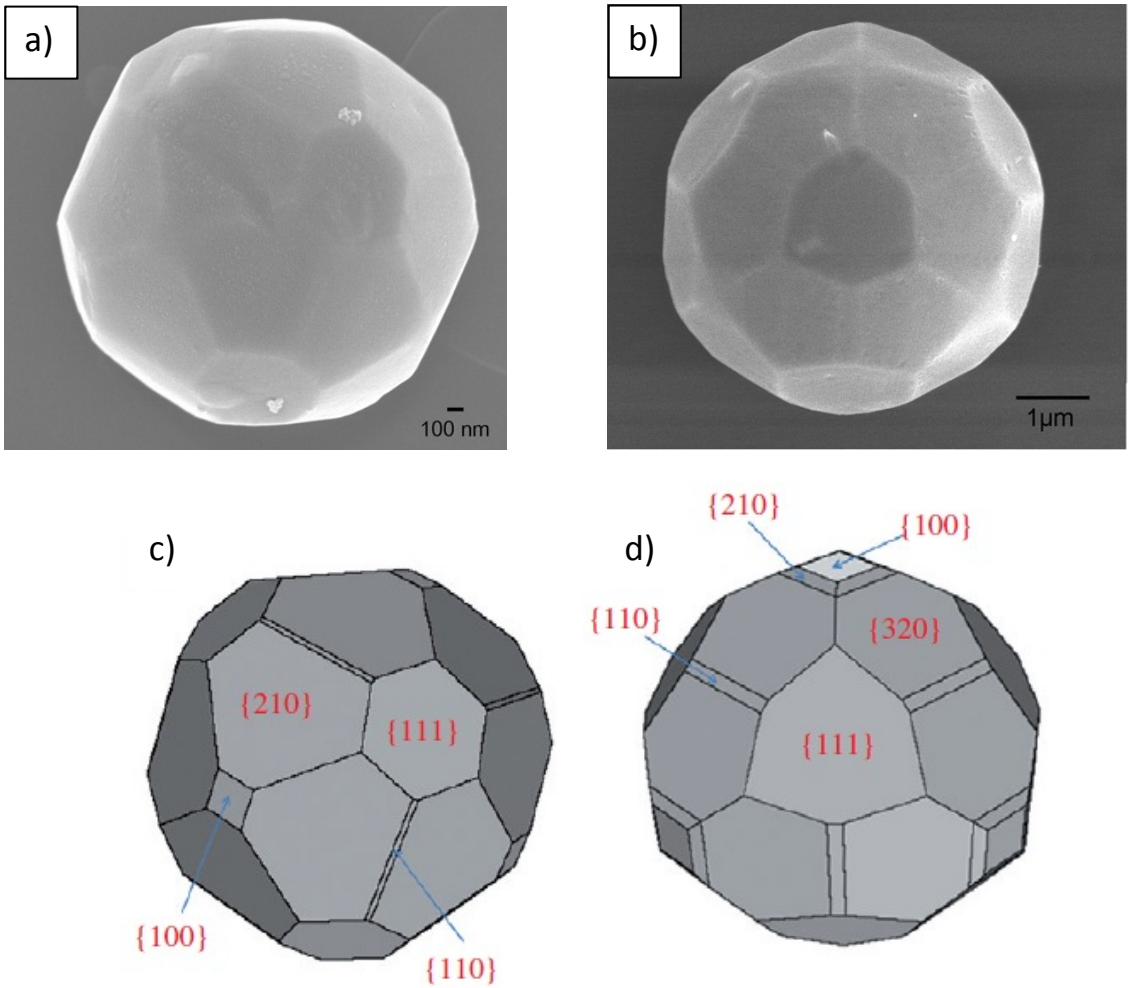

Figure 2.2 Experimental (a), (b) and software-generated (c), (d) ECS of pure Ni [25].

index plane separated by atomic steps. Since the stability of the surface configuration depends on its surface energy, these atomic planes are unstable and the respective vicinal surfaces have stepped shape schematically presented in the figure 2.3 [26].

The total energy of a vicinal surface plane can be represented by the surface energy of the low index plane γ_0, the energy of the step γ_1 and the step density $\tan\alpha/h$ [24]:

$$\gamma(\alpha) = \cos\alpha\left[\gamma_0 + \gamma_1\frac{\tan\alpha}{h}\right] \qquad (1)$$

This equation shows that the gain in energy due to the exposing the low index instead of any arbitrary plain is counterbalanced by the energy spent for creation of the steps. The latter term grows with increasing of miscut angle until the sum of both equals to the energy of the respective plane which becomes a new stable facet.

Actually equation (1) does not contain a contribution of the step-step interactions which becomes important with decreasing of the average terrace width (smaller step-step separation). It was shown that the energy of the step-step interactions may be expressed as quadratic and higher order terms in the expansion of the surface energy in series of the $\tan\alpha$ powers [27]:

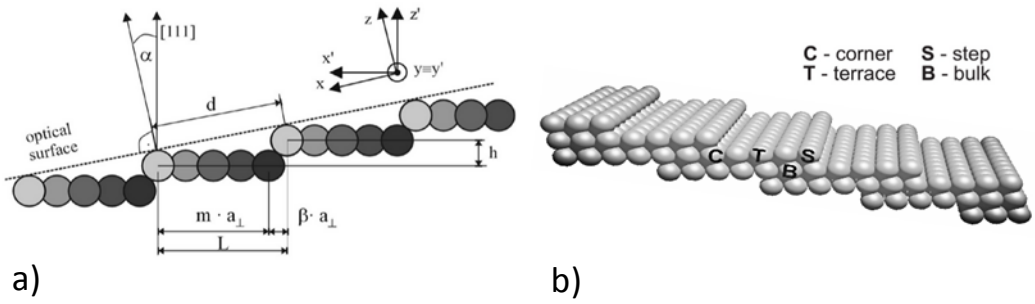

Figure 2.3: Schematic representation of the stepped structure of a vicinal surface [26].

$$\gamma(\alpha) = \cos\alpha \left[\gamma_0 + \frac{\gamma_1}{h}\tan\alpha + \gamma_2(\tan\alpha)^2 + \cdots\right] \qquad (2)$$

The step-step interactions may be of energetic or statistical origin. Indeed, formation of kinks allows the step to wander but this process is limited by the high energy cost of the step crossing. It results in unequal probability of the appearance of the kinks towards to and apart from the adjacent step which looks like an effective (so-called entropic) repulsion [28]. Overlapping of the strain fields from the neighboring steps leads to the increasing of the surface energy which also generates step-step repulsion. Eventually, redistribution of the electric charge near the steps (Smoluchowski smoothing) leads to the formation of the line dipole parallel to the step and gives rise to the electrostatic step-step interaction (see figure 2.4). It can be repulsive of attractive depending on the mutual orientation of the dipole moments.

The implicit assumption that the steps are one atom high (have a height of only one interplane distance) is justified within the model of broken bonds which releases the excess in energy with reduced coordination of atoms. Nevertheless there are some predictions that a double-height step may be energetically more favorable than a regular step because of the bond formation on the step edge [28]. Furthermore, a step-step interaction term in the equation (2) can be smaller for the multilayer steps because of the bigger step-step separation. Therefore probability of the formation of these steps can grow with increasing of the miscut angle [28].

The reconstruction of the terrace can stabilize some certain values of the terrace width and lead to the formation of more complex structures (faceting). For example in

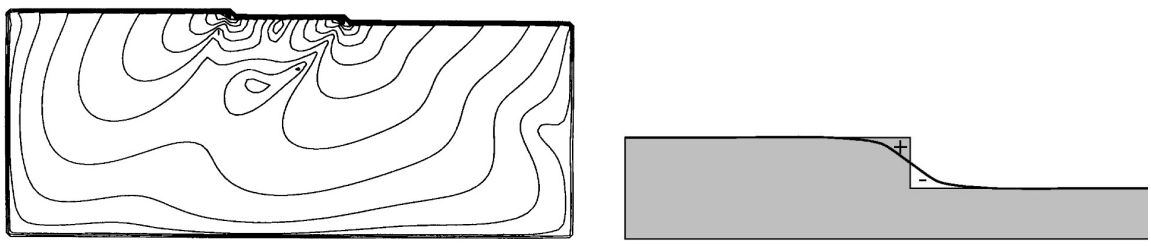

Figure 2.4: Strain fields generated by the steps in a vicinal surface, and the Smoluchowski line dipole in an atomic step [26].

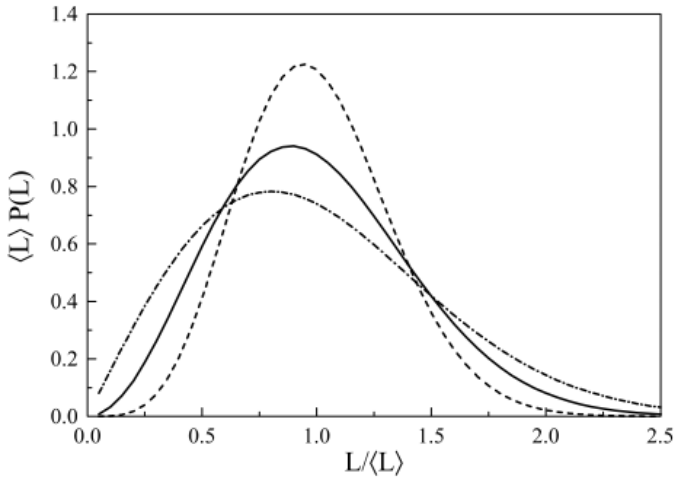

Figure 2.5: Terrace-width distributions for repulsive interaction (dashed line), purely entropic interaction (solid line) and attractive interaction (dot-dashed line) between steps [29].

Au(11,9,9) and Au(4,3,3), (111) terraces are separated by 10° vicinal facets, while the surfaces of Au(4,5,5) and Au(5,7,7) consist of periodic repetition of the facets, characteristic of the miscut angles of 4 and 10° [30].

The average terrace width of the stepped surface is defined by the miscut angle whereas the distribution of the terrace width (the distribution of the distances between the neighbor steps) depends on the interaction between the steps. Strong repulsive interactions result in narrow and symmetric distributions which can be well approximated with a Gaussian peak (see figure 2.5). Meanwhile entropic interactions produce wide asymmetric distributions [1,2].

In the last decades interaction between steps has attracted interest and many experimental works related to this topic have been carried out. In particular, Giesen [29, 31, 32] and Einstein [33] investigated the dynamics of steps in solid/vacuum interfaces and the effect of the step-step interactions on the terrace width distribution. The evolution of the surface morphology has been studied in terms of motion of steps and phase separation observed on vicinal Pt(001) [1] or the faceting of the vicinal Si (111) at different temperatures [34]. Other authors have studied the dynamics of steps on vicinal surfaces using models, such as Jeong et al. [35] and their relation with the equilibrium crystal shape [36]. Vicinal surfaces have attracted also interest for testing fundamental properties of electrons, such as the electronic surface states studied by Corso et al [11] on the curved Au(111) and the effect of the periodic step structure on the surface bands in curved Cu(111) and Ag(111) [10]. Kuhnke [7] and Rousset [6] have shown that regular array of steps can be useful as nanotemplates for the growth of low-dimensional structures on vicinal Pt(111) and Au(111), respectively.

2.2 LEED and STM

Low Energy Electron Diffraction (LEED) is an experimental surface sensitive technique used to study the crystallography of solid surfaces. Qualitative information about the symmetry, the periodic arrangement of atoms and quality of the surface can be obtained from the LEED diffraction pattern. The experiment basically consists in the observation of the backscattering of a beam of electrons directed perpendicular to the surface using an electron sensitive (phosphorous) screen. Diffraction spots yield information from the elastically scattered electrons whereas the background intensity is related to the inelastically scattered electrons. The coherence length of electrons used in the LEED experiments is typically about 10 nm but the spot size of the electron beam is around 0.1 mm therefore the diffraction pattern is an average of many patterns originated from the domains with diameter of ~10 nm (LEED is spatially averaging technique). Sharp spots (their intensity is proportional to the number of electrons in the corresponding beams) with high contrast and low background intensity indicate long range crystalline order (within the diameter of the electron beam).

The LEED technique is aimed to probe surface properties and therefore the information should be collected from the surface and not from the atoms composing the bulk. Taking this into account the probing radiation must have short penetration range and then, the energy of the electron beam should be appropriated. Figure 2.6 shows the dependence of the escape depth of the electrons on the kinetic energy of the incident beam. It can be seen that in the energy range from 20 eV to 300 eV the escape depth is between 5 and 15 Å and thus only few top atomic layers are involved in the formation of the LEED diffraction pattern. Furthermore, for this range of energy the wavelength of the electrons is of the order of the interatomic distances which makes possible the diffraction on the periodic crystal structure.

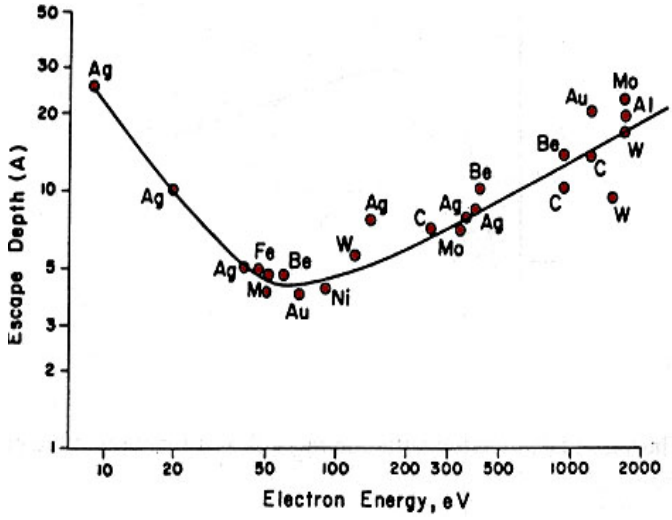

Figure 2.6: Universal curve for the escape depth of the electrons from a solid versus the kinetic energy of the electrons [37].

Main features of the LEED pattern can be understood in the frame of the kinematic theory [24]. It does not take into account the multiple scattering events and therefore fails to predict the exact distribution of the intensity of the diffracted beam but suffices to give a correct symmetry of the pattern and allows the use of the easy geometrical technique. Considering the diffraction on the ideal 2D periodic structure the condition for the occurrence of an elastic Bragg spot in the pattern is given by the Laue equation:

$$\mathrm{K_{II}} = \mathrm{k_{II}^{'}} - \mathrm{k_{II}} = \mathrm{G}_{hk} \quad (3)$$

where $\mathrm{k_{II}^{'}}$ and $\mathrm{k_{II}}$ are respectively the projections of the outgoing and incoming electron momentum parallel to the surface, $\mathrm{G_{hk}}$ is the vector of the 2D reciprocal lattice [24]. The condition $K_{II} = G_{hk}$ can be shown in the Ewald sphere (figure 2.7). The geometry of the sphere is constructed in such a way that the wave vector k of the incident beam is positioned with its end pointing to the (0, 0) reciprocal lattice point, the absolute value of the incident and scattered momentum is constant and equals to the radius of the Ewald sphere.

Although equation (3) is written for the projections of the momentum on the 2D plane of the reciprocal space it is more convenient to extend this space in 3D drawing the rods perpendicular to the plane. In this case the condition $\mathrm{K_{II}} = \mathrm{G}_{hk}$ means that the resulting vector K ends up in arbitrary point of the rod passing through the point G_{hk}. In the example shown in the Figure 2.7 complete geometrical construction is done for the (1, 0) reciprocal lattice point, but the diffraction pattern will include also the spots corresponding to the $(\overline{3}, 0)$, $(\overline{2}, 0)$ etc points.

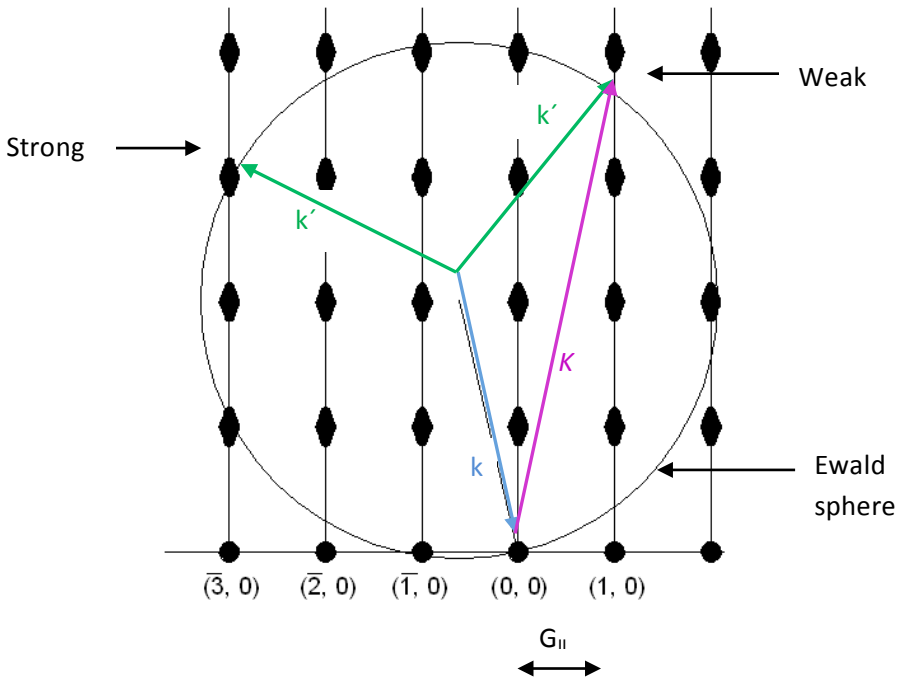

Figure 2.7: Ewald construction for elastic scattering. Rods normal to the surface represent the 3D system

For a real LEED experiment the electron beam penetrates in the sample a few atomic layers deep, and the Laue equation must be taken into account. The rods of 3D reciprocal space will be modulated periodically and in the limit of the infinite penetration depth they will become the points. The intensity of the spots appearing in the diffraction pattern according to the equation (3) will also be modulated. As seen from the example in the figure 2.7, direction corresponding to the $(\overline{3}, 0)$ rod of reciprocal space gives a spot of high intensity, whereas (1, 0) reflection would be weak.

Random defects on the surface do not perturb the LEED pattern due to the small coherence length of the electrons (10 nm) however any periodic structure on the surface will alter the Laue conditions (3) and therefore modify the respective diffraction pattern. Figure 2.8 illustrates the simplest case of a surface with a regular array of monoatomic steps resembling the microstructure of a vicinal surface. The step height creates an inclination angle between the main lattice plane and the macroscopic surface (optical plane) shown by the dashed line. The regular step array is defined by the step height (h) and periodicity in the optical plane (d).

The Ewald sphere for a regular step array is constructed in such a way that the lattice periodicity and the periodicity of the step array, given by the inclination of the average surface, are superimposed. The reciprocal lattice periodicity is given by 2π/a corresponding to the distance between the rods whereas the second periodicity arises from the average surface and is given by 2π/d.

Since the terraces have a finite width the rods become slightly delocalized which is

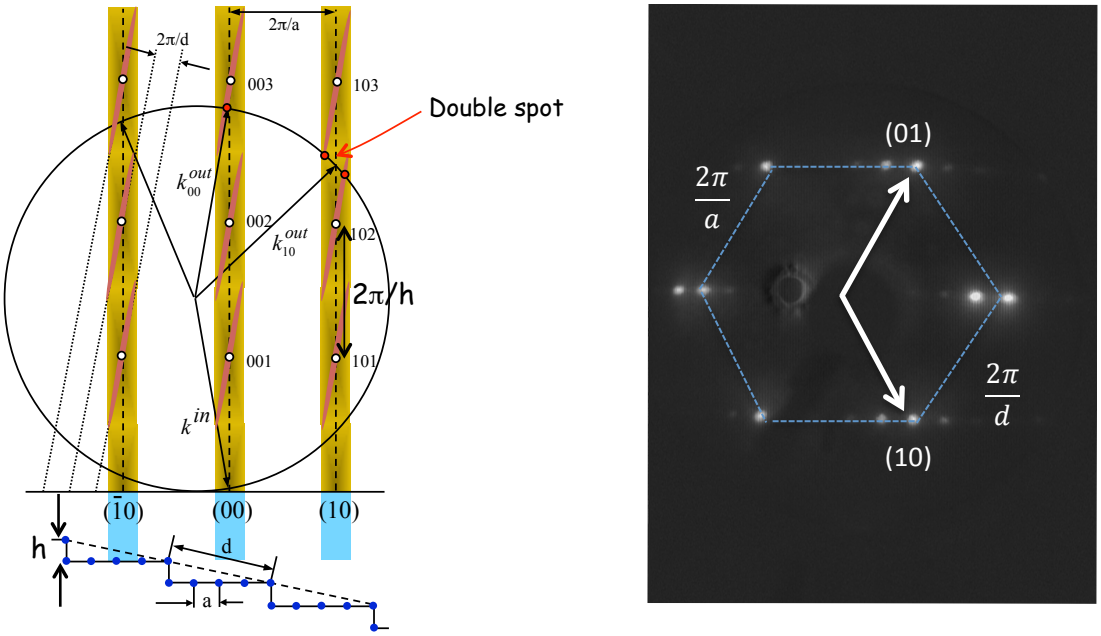

Figure 2.8: Ewald construction (left) and LEED pattern (right) for a vicinal surface. The energy of the incoming beam is defined by the length of k_{in} and gives rise to the Ewald sphere for the LEED pattern. Intersection of the step array and the atomic lattice rod causes the splitting of the spot at (10) while single spot is observed at (00) and $(\bar{1}0)$. The LEED shows an hexagonal pattern of the (111) surface of an fcc lattice. Clear and separated spot splitting indicates a regular step array

shown in the figure 2.8 (left) as a finite width of the stripes. The modulation of intensity due to the non-zero penetration depth of the electrons is shown as a variable color of the stripes. If the Ewald sphere passes through the point where the stripe crosses the rod corresponding to the stepped structure the respective spot will appear in the diffraction pattern. In some cases the sphere can pass through the two (or more) crossing points as it happened for the (10) point of the reciprocal space then respective spot is split in two as well (see the figure 2.8 (right)). The distance between the split spots is equal to $2\pi/d$ and therefore gives the possibility to calculate the terrace width. Clear and separated split spots appear for a regular step array and the direction of the splitting is perpendicular to the steps.

The LEED experimental set up (see figure 2.9) basically consists of an electron gun providing beam energy in the range of 40-400 eV and a fluorescence phosphorous screen where the Bragg spots are visualized. The operation mode of the LEED system is the following: the filament is heated and emitted electrons pass through some optical apertures that are used for the acceleration and focusing of the electron beam. The electrons reach the sample and after reflection they pass through a set of semispherical grids. Two of the grids are connected to ground to avoid fields near the sample which would deviate the trajectory of the electrons and other grid is set to a positive potential slightly lower than the incident beam energy. This grid is referred to as the suppressor and is aimed to filter out the inelastically scattered electrons.

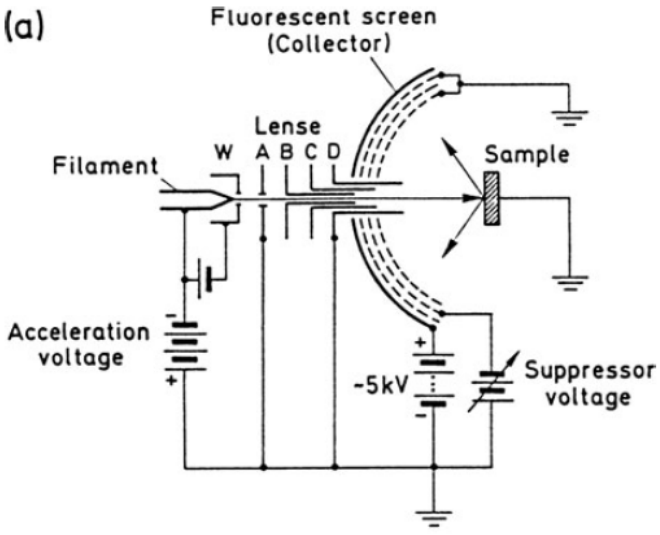

Figure 2.9: Standard LEED setup with main components indicated [24].

Scanning Tunneling Microscopy (STM) is a scanning probe technique that allows to obtain real space images of a semiconductor or metallic surface with atomic resolution. The image is obtained by recording the electron tunnel current between the tiny metallic tip, which is moved across the surface, and the sample surface.

The STM is based on the quantum mechanical effect of tunneling, and is a consequence of the wavelike properties of the particles. In contrast to a classical picture, the tunneling effect basically states that a particle impinging a potential barrier with energy lower than the height of the potential barrier can penetrate through this barrier and reappear at the other side. The distance between the tip and the sample is represented by the width of the barrier while the height of this barrier is given by the work function, which is the minimum energy required to remove an electron from a metallic surface. This work function is usually in the range 2-5 eV [41] and depends on the material and on the crystallographic orientation of the surface.

To initiate the tunneling a metallic sharp tip is brought very close (5-10 Å) to the sample surface [39]. Due to the proximity of two conducting electrodes (sample and tip) an overlapping of the wave functions of the electrons occurs through the vacuum region (potential barrier) [40]. Then, the applied voltage (positive or negative) to the sample establishes a quantum tunneling current of electrons between the tip and the sample surface. A scheme of a scanning tunneling microscope is shown in figure 2.10.

The tunneling current occurs at atomic-scale distances and depends exponentially on the distance between the tip and the sample according to the formula [24]:

$$I_T \propto \frac{U}{d} \exp\left(-Kd\sqrt{\bar{\phi}}\right)$$

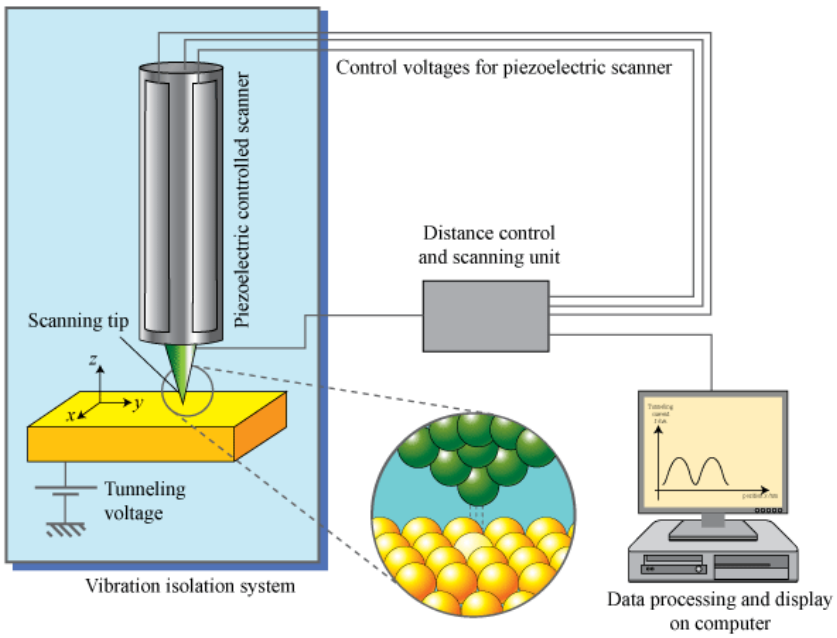

Figure 2.10: Simplified structure of a scanning tunneling microscope [38].

where U is the applied voltage between the two electrodes (tip and sample), $\overline{\phi}$ the average work function ($\overline{\phi}$>>eU) and K, a constant. The exponential dependence of I_T on d and $\overline{\phi}$ functions gives high sensitivity to the instrument. I_T usually changes one order of magnitude for changes of 1 Å in the distance d, due to corrugation of the surface or a local variation of the work function.

The direction of the tunneling current depends on the sign of the voltage between the sample and the tip. When no voltage is applied, Fermi levels of the tip and the sample are equalized and both are in thermodynamic equilibrium. However, application of the voltage shifts (upwards or downwards) the energy levels [42]. If positive voltage is applied the tunneling current can only occur in the direction from the metal tip to the sample (figure 2.11a). More precisely, there is a flow of electrons from the occupied metal states into empty states of the sample. On the contrary, when negative voltage is applied to the sample the current flows from occupied surface states of the sample (figure 2.11b). Therefore, according to the sign of the voltage empty states (positive bias) or occupied states (negative bias) of the sample can be probed.

Regarding the instrument, the movements (x,y,z) of the tip are controlled by electric signals applied to the piezoelectric transducers (see figure 2.12). By means of these transducers variation of voltage of 1 mV gives the movement with accuracy in the Å range. However, the shape of the tip plays an important role for the correct performance of the STM since the radius of the tip affects the lateral resolution of the STM image.

In general, the STM can work in two different operation modes: constant height (d) or constant current (I_T) mode. Our STM operates in the constant current mode in the following way. The tip scans over the surface with a constant I_T current, usually in the 0,5-5 nA range, and this I_T is compared with a preset value (Io) in a feedback loop [43]. The difference between both currents is converted into a correction of the voltage and sent to the piezo-electric transducer. The current is kept constant by approaching or retracting the tip from the sample and, therefore, the correction signal is related to the

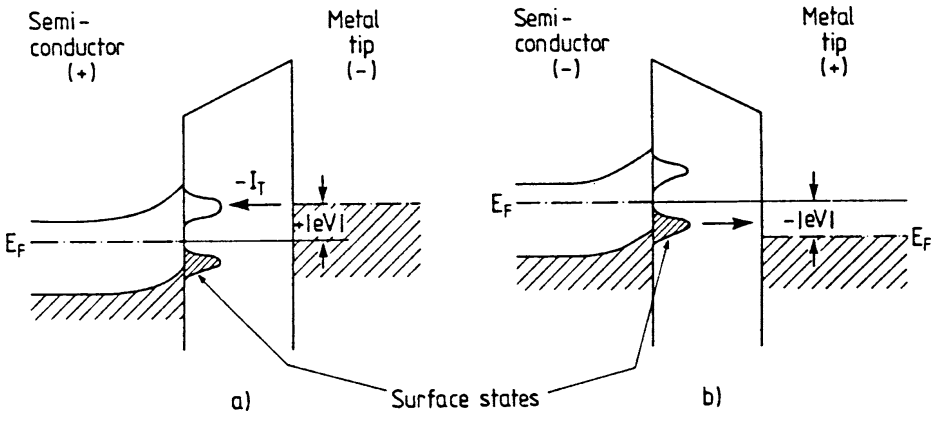

Figure 2.11: Energy band scheme of the tunneling junction for two opposite values of bias voltage. The "semiconductor" refers to the sample [24].

topography of the sample. However since the tunneling current is influenced by the local density of states (LDOS) of the sample surface interpretation of the topography map is not straightforward.

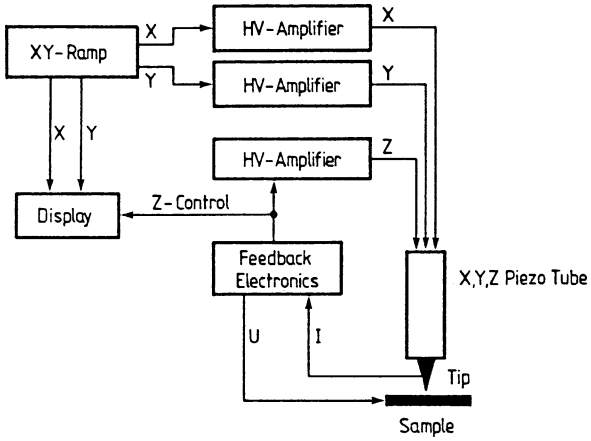

Figure 2.12: Main components of the electronics of a STM. The tunneling current between the simple and the tip controls the movement of the tip in the z direction via feedback electronics and HV amplifiers [24].

2.3 Single-domain particles

Since the magnetic objects studied in this work (continuous atomic layers and islands of few monolayers height) have at least one of the characteristic dimensions in the range of 1 nm, the effect of the reduced size on the magnetic properties of materials is briefly reviewed. The first obvious consequence of the decreasing of the characteristic dimensions is a disappearance of the magnetic domains. Indeed, for small ferromagnetic particles there is a critical size below which the energy cost of the creation of a domain wall is higher than the energy gain due to elimination of the dipolar energy. Thus, below certain size the particles in thermodynamic equilibrium are in single domain state. The critical radius r_c is given by [44]

$$r_c \approx 9\frac{(AK_u)^{1/2}}{\mu_0 M_s^2}$$

where A is the exchange constant, K_u the uniaxial anisotropy constant, μ_0 the vacuum permeability and M_s the saturation magnetization. Typical r_c values for Fe and Co are 15nm and 35nm, respectively.

One of the most common techniques of magnetic measurements is tracing the magnetization reversal by applying a external magnetic field. This process can be represented as a plot of the projection of the magnetic moment on the field direction versus the field strength (magnetization loops). The virtue of the single-domain particles is that the magnetisation reversal at zero temperature looks like a coherent rotation of the effective macrospin. In the case of the uniaxial anisotropy

$$\mathrm{E_a} = \mathrm{K}\sin^2\theta$$

this approximation is called Stoner-Wohlfarth model [45] and the implicit equation for the magnetization loop can be derived analytically.

Considering the particle (figure 2.13) in which all atomic moments always stay parallel and make up a total moment M_s the total energy in the magnetic field is:

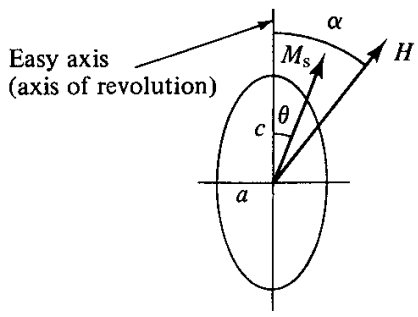

Figure 2.13: Rotation of the magnetization by H applied field in a single-domain ellipsoid [46].

$$E = E_a + E_p = Ksin^2\theta - HM_s\cos(\alpha - \theta)$$

Here the applied field H makes an angle α with the easy axis and θ is the angle between M_s and the easy axis [46]. An angle θ defining the orientation of M_s is found by means of minimization of E:

$$\frac{dE}{d\theta} = 2K\ sin\theta\ cos\theta - HM_s\sin(\alpha - \theta) = 0 \quad (1)$$

while the component of magnetization in the field direction is

$$\mathrm{M} = \mathrm{M_s}\cos(\alpha - \theta) \quad (2)$$

A more compact form of these equations, usually used in the micromagnetic calculations, is obtained substituting the field and the magnetization by the their unitless normalized counterparts h and m:

$$\mathrm{h} = \frac{\mathrm{H}}{\mathrm{H_K}} = \mathrm{H}\left(\frac{\mathrm{M_s}}{2\mathrm{K}}\right),\ \mathrm{m} = \frac{\mathrm{M}}{\mathrm{M_s}}$$

$$\sin\theta\cos\theta - \mathrm{h}\sin(\alpha - \theta) = 0 \quad (3)$$

Magnetization loops calculated using equation (3) for various orientations of the external field are shown in the figure 2.14. The two extreme cases are the magnetic field applied normal to the easy axis ($\alpha=90^0$) and parallel to the easy axis ($\alpha=0^0$). The first leads to zero remanent magnetization, zero coercive field and linear variation of the magnetization when the external field is lower than the saturation field

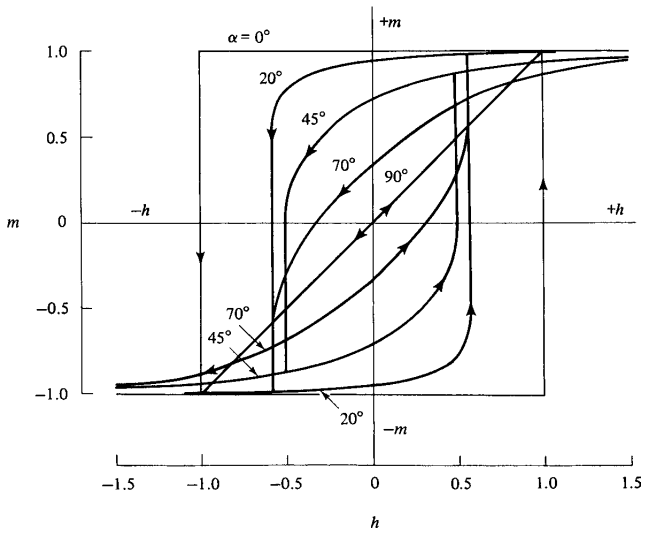

Figure 2.14: Hysteresis loops for single-domain particles with uniaxial anisotropy. α is the angle between the easy axis and the field [46].

$$H_s = \frac{2K}{M_s} \quad (4)$$

In contrast, the magnetization reversal in the field parallel to the easy axis is characterized is by the value of the remanent magnetization equal to the saturation magnetization, and coercive field equal to the saturation field (4).

- Superparamagnetic particles

In the previous section, magnetization reversal was considered for the case of zero temperature. However, in small particles the anisotropy energy that defines the direction of the magnetic moment is comparable with the energy of thermal agitation, which changes the parameters of the loops calculated within the Stoner-Wohlfarth model. A uniaxial single domain particle in a zero applied field has an anisotropy energy given by

$$E = KVsin^2\theta$$

where V is the volume of the particle and θ is the angle between the magnetization direction and the easy axis. According to this expression θ=0 or π are the directions of minimum energy separated by an energy barrier ΔE_B=KV. The dependence of the energy on the angle θ is shown in figure 2.15. In the absence of perturbing forces that could make the magnetization cross over the barrier, the magnetization would remain stable pointing in one of the directions (θ=0 or π). However, thermal agitation can provide enough energy to cross over the barrier. This can occur if the volume of the particle is small, so that the height of the barrier is lowered, or also if the temperature is high. In any of those cases the fluctuations of the magnetic moment would

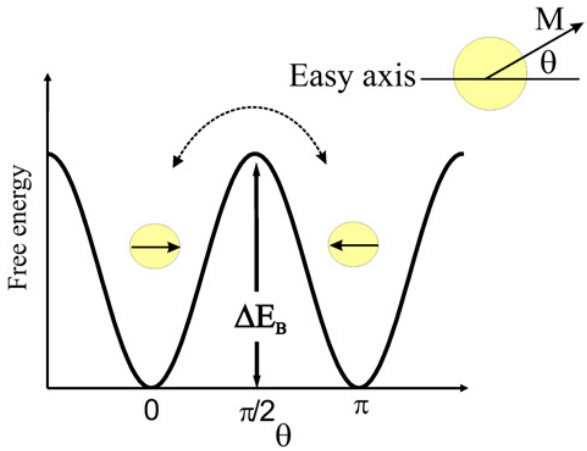

Figure 2.15: Scheme of the free energy of a single-domain particle with uniaxial anisotropy as a function of magnetization [47].

overcome the anisotropy energy and spontaneously reverse the direction of magnetization without any external field. The characteristic feature of this so-called superparamagnetic state is a zero value of the time-averaged of the remanent magnetization. The critical value of transition temperature from blocked to unblocked superparamagnetic regime (blocking temperature) is given by [48]:

$$T_B = \frac{KV}{25k}$$

where k is the Boltzmann constant. If the temperature is lower than T_b and, the magnetic moment of the particle is blocked, thermal agitation facilitates magnetization reversal in external field, decreasing the coercive field. The respective equation is called Sharrock's law [49]:

$$\mathrm{H_c} = \mathrm{H_0}\left[1 - \left(\frac{\mathrm{T}}{\mathrm{T_b}}\right)^{2/3}\right]$$

where H_0 is a coercive field at zero temperature (4).

- Surface anisotropy

Experimentally it is found that anisotropy of thin magnetic films is inversely proportional to their thickness t [21], so that the plot of K*t vs t is linear (see figure 2.16). Therefore the (effective) anisotropy K of a thin magnetic film with thickness t can be represented by the sum of the surface anisotropy (K_S) and volume anisotropy (K_V) contributions [21]:

$$K = K_{eff} = K_V + 2K_S/t \quad (5)$$

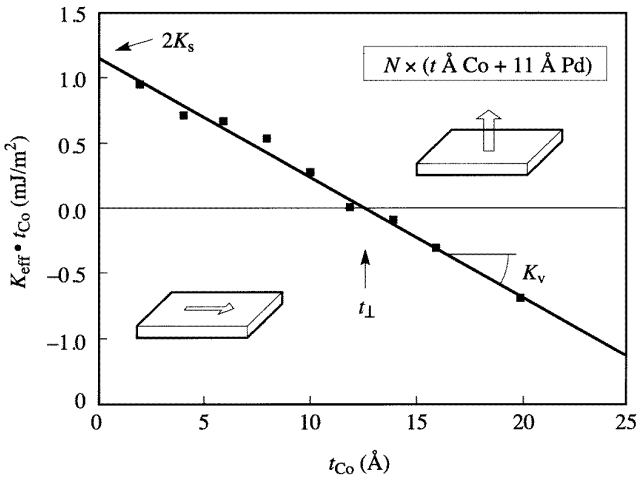

Figure 2.16: Plot of the preferred direction of magnetization (in plane or out-of-plane) as a function of the thickness [21].

The prefactor 2 included in the relation shows that the film is bounded by two identical interfaces. Both values K_S and K_V can be found from the plot 2.16 as a crossing point with the vertical axis and a tangent, respectively. For the majority of magnetic films, the volume contribution of magnetic anisotropy is dominated by the shape anisotropy term, which facilitates in-plane orientation of the easy magnetisation direction (negative value of K). Nevertheless the surface anisotropy is positive in many cases and stronger than the volume part [21]. It results in overall positive value of the K_{eff} and out-of-plane direction of the easy magnetic axis, as it happens, for example, in the case of Co/Pd(111) and Co/Ni(111). Since the second term in the equation (5) decreases with thickness, volume contribution becomes bigger at some critical value t and the spin reorientation transition from OOP to IP easy axis occurs. Typical values of the critical thickness for cobalt are 5-15 atomic monolayers depending on the substrate [21].

2.4 XMCD technique

X-ray Magnetic Circular Dichrosim (XMCD) can be defined as the difference in the absorption intensity between parallel and antiparallel orientation of the magnetization direction of the sample with respect to the helicity of the exciting circularly polarized light. When the angular momentum points in the direction of the wavevector *k* photons have positive *+ħ* helicity (the so- called right circularly polarized light) while negative *–ħ* helicity is referred to the angular momentum pointing in the direction of *-k* (the so-called left circularly polarized light). The XMCD signal can be expressed as [50]:

$$\Delta I = I^{\uparrow\downarrow} - I^{\uparrow\uparrow} = I^{-} - I^{+}$$

Synchrotron radiation is generally used to perform XMCD measurements. Synchrotron radiation provides white light with a broad wavelength spectrum [54] and the required wavelength (λ) is selected by the monochromator. X-ray energy is given by ħω, being the angular frequency ω inversely proportional to the wavelength λ as $\omega = 2\pi c/\lambda$. According to this, monochromatic light with tunable energy is used for the XMCD experiments.

In practice XMCD experiments can be done in two ways (see figure 2.17). One can perform the experiment, by saturating the magnetization of the sample along the direction of k and then keeping the photon helicity +ħ. Once the X-ray Absorption Spectrum (XAS) is measured, the magnetization direction is maintained and the photon helicity is switched to -ħ in order to measure a second spectrum. Finally the XMCD spectrum is obtained by subtraction of both XAS spectra. Inversely to this, the other alternative is to switch the magnetization direction (±H) for a given photon helicity. In both cases, the magnetization is saturated for maximum XMCD effect.

From the experimental point of view, when x-rays interact with matter, the incident photon is absorbed so that a core hole is created and an electron from the core level is excited. Tus XMCD is an element specific technique. It involves the electronic transition of a core electron, which is strongly localized in the atom, to the empty

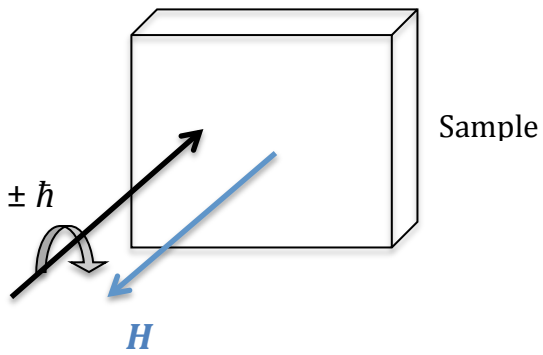

Figure 2.17: For this XMCD experiment the helicity of the light is changed to measure both XAS spectra while the direction of the magnetic field remains constant [53].

valence shell. According to this, near the resonant absorption edge a peak is observed in the XAS spectrum. This peak corresponds to the binding energy of the core electron to the atom and is associated with specific transition from the core state to empty valence state of the element. The core hole has a total angular momentum j given by [52]

$$j = l + s$$

where l is the orbital momentum and s is the spin angular momentum.

The spin angular momentum of each core can be either ½ or -½ and the orbital angular momentum relates each core level with an specific number as denoted in table 2.1:

Core level	*l*
s	0
p	1
d	2
f	3

Table 2.1: Orbital angular momentum for the different core levels

For the specific transition from a 2p core state to 3d valence state two sum rules were proposed [51]. The sum rules allow quantitative separated calculation of spin and orbital magnetic moments from XMCD spectra. An example for the Fe XAS spectra is shown in figure 2.18. The two peaks correspond to the L_3 (first peak) and L_2 edges (second peak).

The intensity of the peaks represents the number of photons absorbed per atom divided by the number of incident photons per unit area. This is defined as the x-ray absorption cross section. The corresponding height for each of the peaks is associated with the quantum degeneracy and this is defined by the number of states 2j+1. j representing the total angular momentum is an integer value between j=l+s and j=l-s. For the specific 2p to 3d transition, the p core level corresponds to l=1 orbital angular momentum and therefore j is given by:

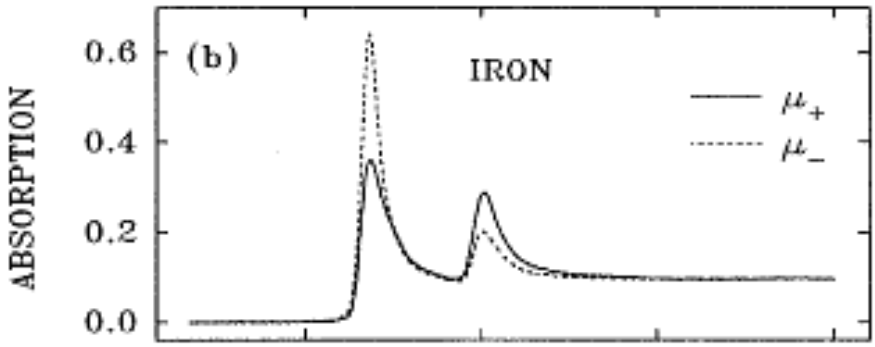

Figure 2.18: XAS absorption spectra for Iron taken at two opposite saturation magnetizations [51].

$$j = l + s = 1 + \frac{1}{2} = \frac{3}{2} \ (L_3\ peak)$$

$$j = l - s = 1 - \frac{1}{2} = \frac{1}{2} \ (L_2\ peak)$$

The first peak in the XAS spectrum is called the L_3 peak and corresponds to the $2p_{3/2}$ configuration (j=3/2). The second peak is called the L_2 peak and corresponds to the $2p_{1/2}$ configuration (j=1/2). According to the 2j+1 quantum degeneracy four states correspond to the first peak and two states correspond to the second peak. These six states are related to the six electrons that occupy the p orbitals. The intensity ratio between the L_3 and L_2 peaks is 2:1 respectively if the spin-orbit split states are only considered. At the L_3 edge x-rays with positive photon spin excite more spin up electrons than x-rays with negative photon spin while at the L_2 edge the opposite is observed.

One requirement for the application of the sum rules is that the 3d valence states must be separated from other final states. In the near edge region the x-ray excitations are associated with transitions from core states to empty valence states. However, outside the near-edge resonance region the photoelectron is directly excited into continuum states and the excitation cross section varies smoothly with energy. The latter is represented by the background, which is assumed to contain all the continuum transitions, and consists of one function represented with an edge step followed by a constant cross section.

The edge step function of the background is normalized to 1. It consists of two steps corresponding to the L_3 and L_2 peaks with 2/3 and 1/3 height of the averaged normalized intensity, respectively. The fractions of the first peak (2/3) and second absorption peak (1/3) are associated with the number of electrons, 4 and 2 of the total six electrons characteristic of the p orbitals.

For the application of the sum rules XAS and XMCD spectra are required. Spin and orbital magnetic moments can be calculated from two equations (6) and (7) that are determined by three parameters p, q and r. The r value (see figure 2.19) represents the integral of the summed XAS spectra for both right and left circularly polarized light of L_2 and L_3 peaks after removal of the edge step function. p and q values are obtained from the XMCD spectrum, as shown in figure 2.20. p represents the integration for the L_3 edge and is calculated at the onset of the L_2 peak. q is obtained from integration of L_2 and L_3 peaks at the same value of energy than r value in the XAS spectrum.

In addition to the values obtained from the XAS and XMCD spectra there is another term involved in the two equations for the sum rules. This term is the 3d electron occupation number (n_{3d}). It is obtained from theoretical calculations and associated with the specific transition metal. Therefore, the equations to calculate the orbital and

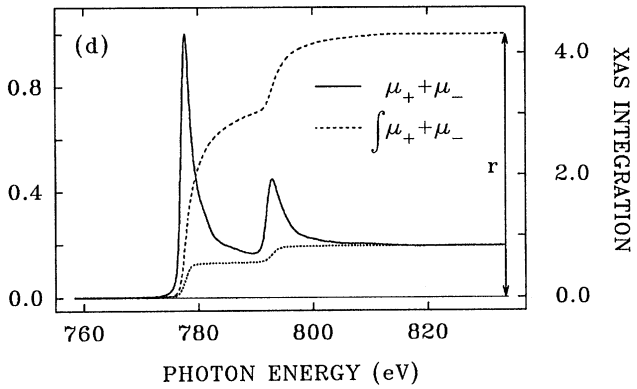

Figure 2.19: Representation of the summed XAS spectra, the integral of the summed XAS spectra after removal of the two-step like function (r value) and the two-step like function (dotted line) for the edge jump removal before the integration [51].

spin magnetic moments respectively are the following [51]:

$$m_{orb} = -\frac{4\int_{L_3+L_2}(\mu_+ - \mu_-)d\omega}{3\int_{L_3+L_2}(\mu_+ + \mu_-)d\omega}(10 - n_{3d}) \quad (6)$$

$$m_{spin} = -\frac{6\int_{L_3}(\mu_+ - \mu_-)d\omega - 4\int_{L_3+L_2}(\mu_+ - \mu_-)d\omega}{\int_{L_3+L_2}(\mu_+ + \mu_-)d\omega}(10 - n_{3d})\left(1 + \frac{7\langle T_z\rangle}{2\langle S_z\rangle}\right)^{-1} \quad (7)$$

The term $\langle T_z \rangle$ obtained from theoretical calculations is small for the transition metals and can be omitted. These two equations can be summarized in:

$$m_{orb} = -\frac{4q}{3r}(10 - n_{3d})$$

$$m_{spin} = -\frac{(6p - 4q)}{r}(10 - n_{3d})$$

The sum rules can only be applied according to the dipole selection rules. These rules correspond to allowed transitions between states of the form $|n, l, m_l, s, m_s\rangle$ and obey [50]:

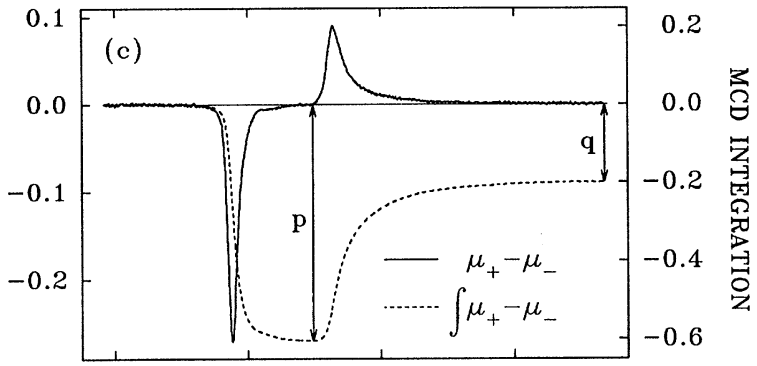

Figure 2.20: XMCD spectrum (black line) and integration of the XMCD spectrum (dotted line) with indication of p and q values [51].

$$\Delta l = l' - l = \pm 1$$
$$\Delta m_l = m_l' - m_l = 0, \pm 1$$
$$\Delta s = s' - s = 0$$
$$\Delta m_s = m_s' - m_s = 0$$

It can be seen from these equations that the dipole operator does not act on the spin, and thus spin is preserved in the allowed transitions. It is assumed that the size of the absorbing atomic shell is small relative to the x-ray wavelength, then $|\mathrm{r}| \ll 1/|\mathrm{k}| = \lambda/2\pi$ and the electric field which drives the electronic transition is constant over the atomic volume. Taking into account the transitions from 2p core shell of radius $|\mathrm{r}| \simeq 0.01\ \mathrm{nm}$ and the photon energy range ($\leq 1000\ \mathrm{eV}$) which corresponds to a wavelength $\lambda \geq 1.2\ \mathrm{nm}$, $|\mathrm{r}| \simeq 0.01\ \mathrm{nm} \ll \frac{\lambda}{2\pi} \simeq 0.2\mathrm{nm}$. This confirms that the assumption is reasonable and the dipole approximation can be used for the calculation of x-ray absorption intensity.

XAS spectra not only provide information to calculate the spin and magnetic moments. The element specific hysteresis loop that relates the applied magnetic field with its magnetization can also be measured. Magnetism through the hysteresis loop can thus be investigated for the specific element by monitoring the XAS at the element´s maximum absorption edge. This corresponds to the energy of the L_3 peak. The method is the following: the helicity is chosen, for example +ħ, and kept fixed while XAS is measured as a function of the applied magnetic field (from +H to –H). The same procedure is repeated with -ħ helicity for the XAS measurement. Finally, the XMCD hysteresis loop is obtained by subtraction of both XAS measurements.

The results of the XMCD measurements shown in this thesis were carried out in two synchrotron beamlines:

- DEIMOS (Dichroism Experimental Installation for Magneto-Optical Spectroscopy) in SOLEIL synchrotron
- BL29-BOREAS (Resonant Absorption and Scattering) in ALBA synchrotron

DEIMOS beamline allows to perform XMCD measurements in the 350-2500 eV energy range. The end-station is provided with cryomagnets so that ±7T (in the direction of the beam) and ±2 T (perpendicular to the beam) can be achieved. Sample temperature measurements between 1.5 K and 350 K can be performed [55].

There are two preparation chambers (RAOUL and MBE) connected to the beamline. Both are used under UHV conditions (in the low 10^{-10} mbar) for sample preparation and sample analysis. RAOUL chamber is used for organic material deposition with a sample storage and transfer to MBE chamber, water cooled effusion cell and a quartz crystal microbalance. MBE chamber is dedicated to metal deposition with two electron beam heated evaporators and a quartz crystal microbalance. Here, sample treatment can be carried out by ion sputtering and annealing up to 1500 K and sample analysis

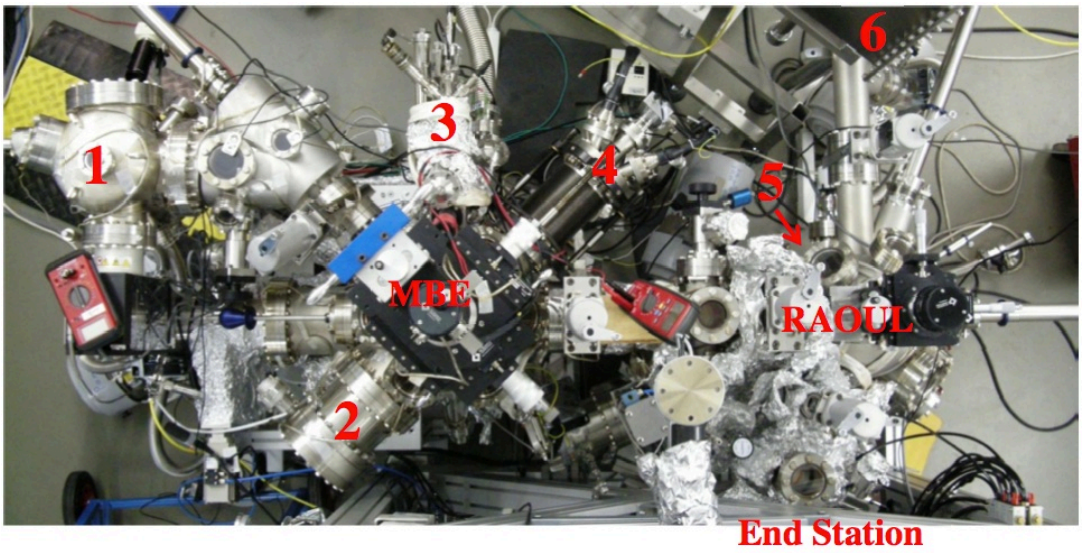

Figure 2.21: Sample preparation chambers (MBE and RAOUL) environment with their main parts indicated [55].

can be performed by AES and LEED. One of the flanges of this chamber is connected to a variable temperature STM where measurements in the 50-500 K can be carried out. The main parts of the MBE and RAOUL chambers are more clearly shown in figure 2.21. These parts are:

1- Variable temperatura STM
2- LEED
3- Two electron beam evaporators
4- Auger
5- Effusion cells for organics
6- Glove box

BL29-BOREAS beamline is equipped with two end-stations, HECTOR and MARES, for Dichroism and Scattering techniques, respectively. Our XMCD experiments were performed in HECTOR end-station (see figure 2.22). Absorption spectra of the photons in the 80-4000 eV energy range can be acquired [56]. HECTOR end-station is equipped by vector magnet and connected to the sample preparation and characterization facility distributed between 3-chamber (load-lock, buffer and main chamber) setup. The load-lock is used for fast sample change, the buffer chamber allows smooth transition of the pressure from high vacuum of the load-lock chamber to UHV (the base pressure is of the order of 10^{-10} mbar) of the main chamber. It is provided with a parking for up to four samples. The main chamber is used for sample preparation and main components are the ion sputtering gun, the heating stage and the evaporators for metals and organic molecules. It is just situated below the center of the HECTOR magnet. The cryomagnet consists of three ortogonal superconductong coils allowing maximum fields of 6 T (in the direction of the beam) and 2 T (in horizontal and vertical planes perpendicular to the beam). The sweep rate is of 0.6 T/min in the direction of

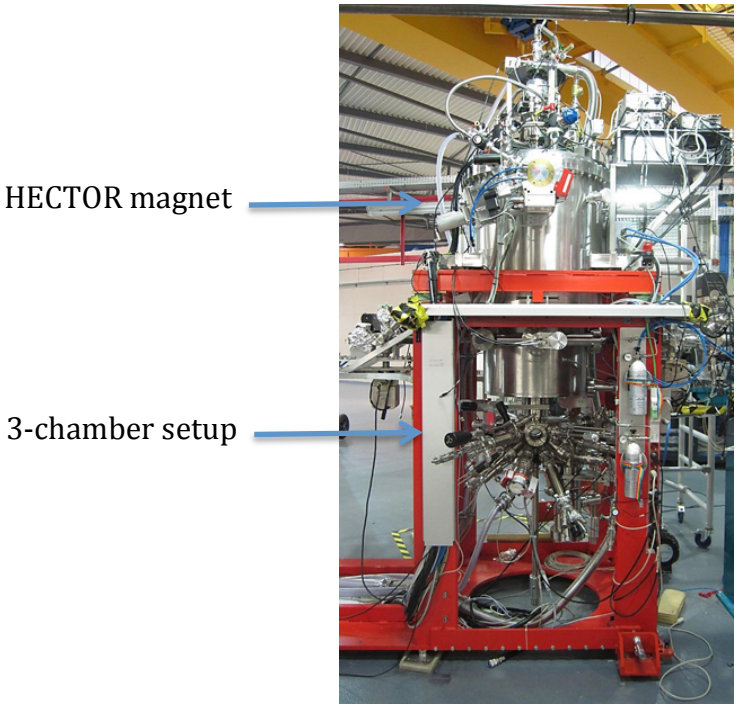

Figure 2.22: Dichroism HECTOR end-station in BL29-BOREAS beamline [56].

the beam and 0.4 T/min in the other two directions. When the sample is ready for the measurements it is mounted on a sample holder attached to the cold finger of the cryostat. Measurements between 2 K and 350 K can be performed.

2.5 Local experimental setup

A surface magneto-optic Kerr effect (MOKE) setup for measurements in ultrahigh vacuum (UHV) has been constructed. This system combines in situ MOKE, LEED (Low Energy Electron Diffraction) and STM (Scanning Tunneling Microscopy) in two separated UHV chambers and then allows the preparation, characterization and magneto-optic measurements of the samples without distortion of the vacuum conditions. Vacuum plays a main role for the study of clean surfaces. Due to the low base pressure ($p=1x10^{-10}$ mbar) inside the system it is possible to perform experiments for time enough with the sample surface free of contaminants. Pressure of 10^{-10} mbar allows experiments during one day without contamination of the surface. Thus, a variety of pumps are used to reach UHV pressure. First, a scroll pump is used for pumping down to a pre-vacuum pressure of 10^{-2} mbar. Then, the system is further pumped down to about 10^{-7} mbar by two turbomolecular pumps (PFEIFFER TMU 261 and PFEIFFER TMU 071) with 200 l/s and 50 l/s average pumping speed of the gases, respectively. At this stage, other type of pump is required to further improvement of the pressure. In our case, the titanium ion pump (Gamma Vacuum 150 T) with 150 l/s pumping speed allows reaching $1x10^{-10}$ mbar UHV vacuum pressure.

An important feature for the construction of the experimental setup is that all materials must be UHV compatible and bakeable at 150 ºC. Furthermore, the components of the manipulator are non magnetic in order to avoid effects in the MOKE signal. Molibdenum and titanium bolts were used for fixing different parts of the manipulator, tantalum stripes for fixing the sample on the sample plate and ceramics were required for electrical insulation.

Next, we will describe the characteristics of each of the chambers separately. Chamber

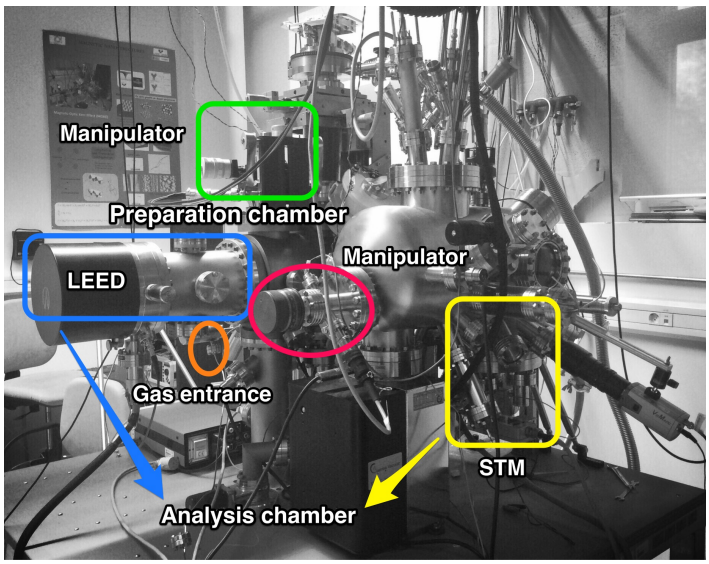

Figure 2.23: Front view of the UHV system with Chamber 1 (STM) and Chamber 2 (MOKE and LEED). MOKE part is not shown in this figure

Figure 2.24: Omicron 25K VT STM model used for the experimental STM images taken for this thesis [57].

1 (see figure 2.23) has been constructed for the preparation and characterization of the samples. The preparation is carried out in the sample manipulator in the temperature range from 300 K to 1000 K. The position of the manipulator (indicated with red circle) inside the chamber is fixed but 360º rotation is allowed. This makes possible facing the sample with the evaporators located in different positions of the chamber. The evaporation is carried out with the MBE (molecular beam epitaxial) technnique that allows the growth of thin films. The experimental setup incorporates two types of evaporators. One of the evaporator integrates a flux monitor (Omicron EFM 3) and the evaporation is carried out by electron bombardment heating of the bar, rod or crucible. Voltage in the range 800-1000 V is usually applied in this evaporator. The second evaporator (Specs EBE-4) also uses electron bombardment to produce intense localized heating. It is provided with four different materials; two of them are evaporated from their rod form and the other two from the crucibles. Electrons can be accelerated up to 2 kV allowing the emission of up to 150 mA of electron current. This chamber is also complemented with a quartz microbalance for the calibration of the materials. Calibration is required to prepare the samples in order to have an approximated control of the coverage deposited on the sample.

Characterization of the growth nanostructures is carried out by a Variable Temperature STM (Omicron 25 K VT STM) in the range from 25 K up to 1500 K. The STM model used for the experimental STM images obtained in this thesis is shown in figure 2.24. In order to achieve high resolution of the scanning images isolation of the vibration is required. Therefore, the base plate is suspended by four soft springs that are protected by surrounding columns. The surface under study is grounded and faced

down and the tip is floating. The tungsten tip (home-made) is driven by an electrode inside a scanner tube that allows scanning across the sample surface with z-resolution (height) up to 0.1 Å. The maximum scan range for the tip is about 10 µm x 10 µm.

Next, we will introduce Chamber 2 (figure 2.25). It has been constructed for characterization and measurements of the samples by LEED and MOKE techniques, respectively. Each of the techniques is performed in two different manipulators with a distance separation of 300 mm. The LEED model is shown in figure 2.26 (Omicron SPECTALEED). It incorporates an integral electron source which operates up to 3,5 keV and the filament operating current is approximately 1,7 A. In order to avoid damage of the filament during operation the pressure in the chamber should be below $1x10^{-7}$ mbar. The manipulator used for the LEED was also used for common surface preparation methods such as sputtering and annealing cycles. Sputtering is carried out with an ion gun, and annealing temperatures up to 1000K can be reached. This manipulator consists of two sample stages that can be rotated and also moved in the three main directions (x,y,z).

MOKE is a common technique for studying thin film and surface magnetism. The constructed MOKE setup allows application of magnetic fields up to 0.1 T at any angle β in the plane XY, as it is shown in figure 2.27. The magnetic field is generated by means of four pairs of water-cooled coils, each pair 45^0 off the horizontal and located outside the UHV chamber. Each of the coils consists of 950 spaced turns and produces a field of 0.08 T at a maximum applied current of 5 A. On top of each of the flanges,

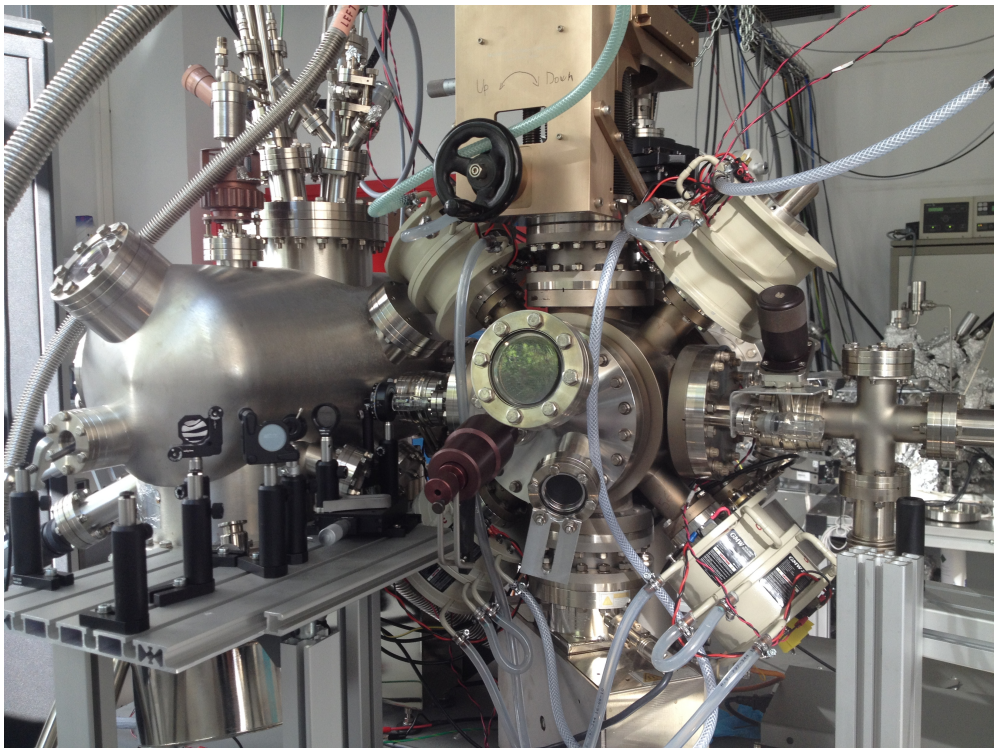

Figure 2.25: Backside view of Chamber 2 where the MOKE setup is shown

Figure 2.26: Omicron SPECTALEED is the LEED model used for the experimental LEED patterns shown in this thesis [58].

two coils are situated together. Soft iron (ARMCO) poles are welded to each of the four flanges inside the UHV chamber in order to bring the magnetic field to the sample. These poles have been constructed to create maximum and homogeneous magnetic field in the center of the sample.

The optimization in the design of the poles was carried out by COMSOL Multiphysics [48] finite element analysis, solverand simulation software. The AC/DC module of this software was used for modeling the electromagnetic system and demonstrated that minimum distance between poles is the most important factor for maximizing the magnetic field. The distance between the poles is 34 mm. It is the minimum that allows passing with the horizontal transfer bar from one chamber to the other one.

Outside the chamber soft iron cylinders continue these poles and pass through the coils. Cylinders are fixed to the flanges by bolts and can be removed for bake-out. The

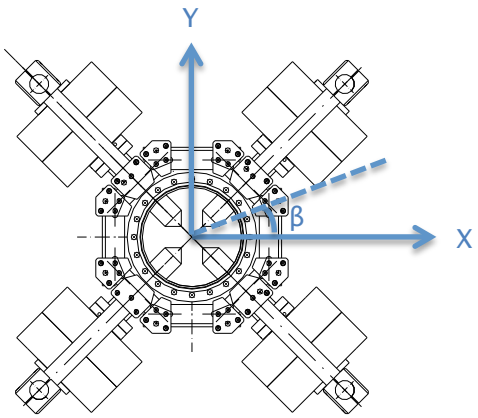

Figure 2.27: The magnetic field is created at any β angle in the XY plane

reason to insert the cylinders in the coils is the permeability of the soft iron that amplifies the magnetic field. ARMCO iron is known to be one of the purest grades of iron. Because of its high purity, motion of the domain walls is not restricted by structural defects presented in the material. In addition to this, an anticorrosive treatment was applied for all ARMCO pieces with a 5 μm thick nickel-phosphor layer. The objective of this treatment has been to prevent oxidation and then to have clean atmosphere for analysis of the sample.

Calibration of the field in horizontal and vertical directions in the central position was performed previous to the measurements. The measured values of the major horizontal and vertical fields were very similar and reached 900Oe as it is shown in figure 2.28. A small remanence was seen when no current passes through the coils. This remanence was due to the ferromagnetism of the iron core and was about 10 Oe. The field close to the center position is homogeneous as it can be in figure 2.29 from the measured values for the horizontal field in all the 3D directions separated 3 mm from this central point. For the maximum applied field the maximum difference was approximately 30 Oe. Thus, the magnetic field is nearly constant in this entire region (maximum variation≈3%) which agreed well with the objective of homogeneity of the field. The calibration of the field was carried out wit a Hall probe (MICRO SWITCH SS94A2C). The estimation of the error in the measurement due to sensitivity of the Hall probe and the acquisition data was around 10 Oe.

The experimental setup allows to perform MOKE measurements in two arrangements for the study of the in-plane and out-of-plane magnetizations. In-plane magnetization can be measured in both longitudinal and transverse MOKE configurations with angle of incidence of 75^0 with respect to the surface normal to the sample. The second arrangement is used for measurement of the out-of-plane magnetization component (the so-called Polar Kerr effect) and the sample is rotated 90^0 with respect to the first arrangement. The angle of incidence is 15^0 with respect to the surface normal to the

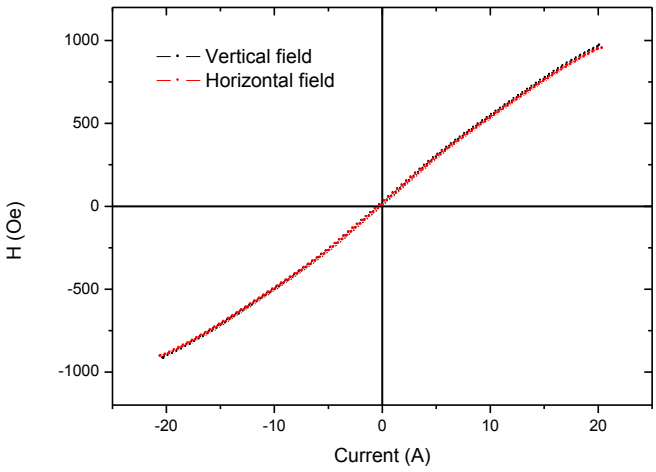

Figure 2.28: Measured vertical and horizontal fields as a function of the current of the coils

sample. In both arrangements the incident beam enters through the same window in the UHV chamber. Transverse Kerr effect can be also measured with the second arrangement if the field is applied in the plane of the sample.

All the optical components of the MOKE setup are mounted outside the chamber. This configuration provides flexibility to use both arrangements (in-pane and out-of-plane) for the MOKE measurements. Birefringence effects were diminished with the use of special windows in the entrance and exit of the beam from the chamber. The intention was to avoid its effect in the MOKE signal.

On the other hand, one of the main advantages of this MOKE setup is the integration of a cryogenic head that is connected to a helium compressor by two gas lines. The cryostat (Advanced Research Systems DE-204P) has a high cooling power and very close to the sample position minimum temperature of 9 K was achieved. In fact, MOKE measurements of 1ML of $GdAu_2$ in the longitudinal configuration have been successfully achieved at this temperature. Cooling down of the system up to 9 K takes approximately 2,5 hours and measurements from 9 K up to a maximum temperature of 350 K can be performed. The system was also designed for maximum isolation of the sample with respect to the cryostat. In order to minimize vibrations four silence blocks were implemented.

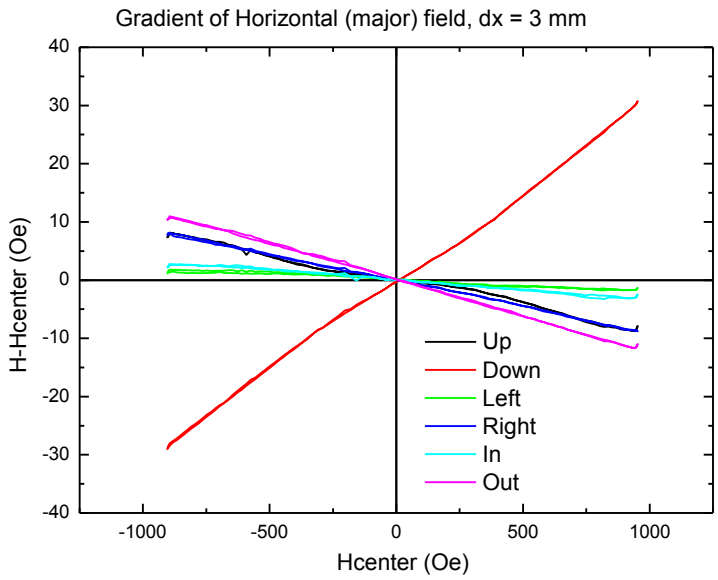

Figure 2.29: Horizontal magnetic field values in different directions 3 mm away from the central position

3. Polishing of the curved crystals

In this chapter, previously to the characterization of the curved crystals with different experimental techniques the main aspects of the procedure for the construction and polishing of the curved crystals are summarized. The development of this new and versatile tool allows to curve crystals within a wide range of materials. Soft and ductile ductile such as copper and palladium, but also hard and brittle materials such as nickel and bismuth respectively, were curved. However, this thesis is only focused on the study of curved Pd(111) and Ni(111) crystals.

These two commercial crystals were initially flat (111) crystals. There are basically two aspects that characterize commercial crystals; the main and the secondary crystallographic directions. The main crystallographic direction is defined by the direction normal to the plane of the surface of cutting. These crystals are oriented with respect to the [111] direction. The secondary crystallographic direction defines the direction of the crystal on the plane of the surface and is used as a reference with respect to one of the edges of the crystal.

The orientation accuracy for the main direction [111] is below 0.1^0. For the secondary direction $[\bar{1}\bar{1}2]$, the deviation of this direction in the (111) surface is below 0.5^0. The quality of the surface is defined by the roughness by means of the R_a parameter. This parameter describes the average of the absolute deviation in the vertical direction of the roughness profile. For commercial crystals R_a is approximately 0.03 microns. Figure 3.1 shows an example of a flat (111) crystal with main directions and dimensions indicated and the same crystal after the curving and polishing process.

For the construction of a curved crystal, all the components of the tool were designed and then fabricated. This tool makes it possible to convert the flat surface into a curved surface with a manual procedure (transference of knowledge of the developed tool and the polishing process was given to Bihurcrystal company). The manual procedure for curving a flat crystal mainly involved two processes, the grinding and the

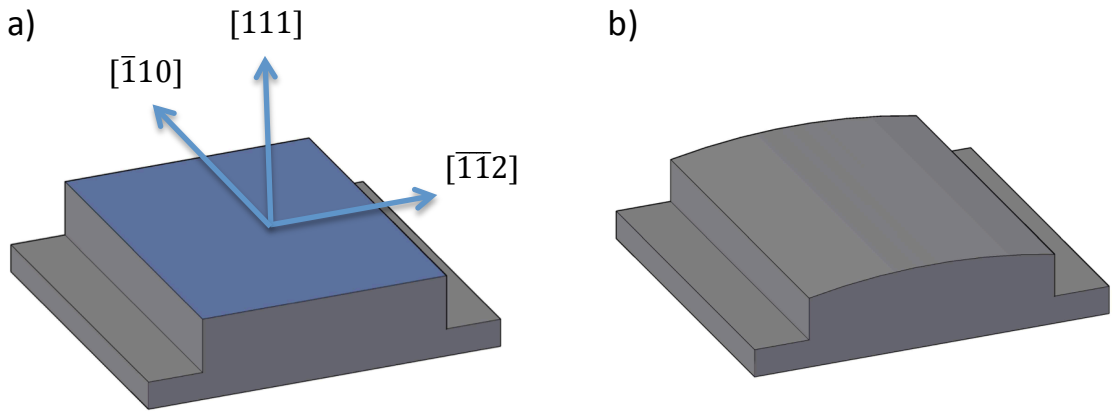

Figure 3.1: Schemes of a) the comercial flat (111) crystal and b) the same crystal after our curving and polishing process

polishing process respectively. Both processes were carried out with the same tool. The majority of the material was removed and the curvature of the crystal was reached with the grinding process. Removal of the material was possible by direct and continuos contact between the sample, the abrasive and the consumables. Then, deformations from the grinding were removed in the polishing process. This process was finished when a highly reflective surface and without any visible imperfection was achieved.

The tool was designed to reach curvatures up to $\pm 15^0$ with respect to the center of the crystal. This angle corresponds to a 12 mm wide sample and this is the maximum posible size, according to the standard sample plates used in an ultra high vacuum system.

Next we will give a little description of the consumables used for the grinding and the polishing processes. The choice of the commercial products depends on the material to be polished. Our lack of experience in the field of polishing samples led to trust on the long experience in metallography of the Struers Company. They are a reference for polishing. In 1970 “Metalog” was publicated. Some years later in 1981 the publication of “Structure” that is the materialographic magazine most diffused in the world, and more recently the “Metalog Guide” helped the work of the metallographic sample preparation.

The choice of the consumables was divided in three main parts: the type of abrasive, the grain size and the cooling liquid. Each of these parts was also different for the grinding and polishing process. Now we will introduce the aspects that were considered for the selection of the consumables.

- *Type of the abrasive*

The grinding process is the first stage in the material removal. Different types of abrasives can be used depending on the hardness and the ductility of the material to be ground. Vicker hardness tests are very common for measurements of metals and the unit of hardness is given by the Vickers Pyramid Number (HV). It gives a value related with the resistance of the material to plastic deformation. For palladium and nickel crystals SiC papers were used since they were appropriate for wet-grinding of materials with 30-800 HV within manual preparation.

For the polishing process the selected abrasive was diamond. It is known as the hardest material (around 8000 HV). Diamonds have demonstrated to efficiently remove scratches caused by grinding without causing excessive deformation. It is crucial that the crystal structure is not damaged during the process and therefore deformation should be minimized as much as possible. The continuous crystal lattice structure with no defects and no grain boundaries of the pure single crystals must be maintained in the entire sample.

Polishing can be carried out with cloths of different elasticity. Polishing cloths are made of carefully selected materials and have separate layers. Depending on their properties with respect to abrasive grain retention and texture a variety of woven,non-woven, and napped cloths can be used. In each case the cloth surface should be, selected to achieve the best performance and the longest lifetime. The selected types of cloths are further detailed.

- *Grain size of the abrasive*

The grinding process is carried out progressively in several steps. Correct choice of the grain size is important for an effective grinding process and to avoid excess of time in each of the stages. Lengthen the time of the process is not recommended to avoid relief or rounding of the borders of the sample.

The diamond suspensions for the polishing process must be selected. The suspensions can be divided into polycrystalline and monocrystalline type, depending on the quality of the sample preparation. Polycrystalline diamonds consist of minute crystallites with small cutting edges that result in a high material removal and low scratch depth. Polycrystalline diamonds were chosen for palladium and nickel crystals since they are best suited for highest requirements and optimum surface quality of the sample. Grain size of the suspensions was also selected. The grain size of the SiC paper must be smaller for the successive steps and the first grain size selected for the polishing must be smaller than the last one used for the grinding process. The successive grain sizes of the diamond products also decreased until the end of the process.

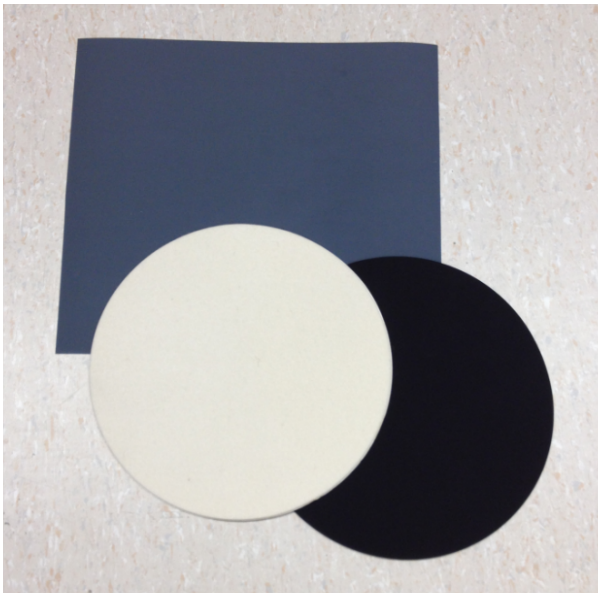

Figure 3.2: Examples of the types of abrasive used in the grinding process (SiC paper) and polishing process (polishing cloth)

- *Cooling*

Cooling is vital in processes of material removal. Water is used as cooling liquid for the SiC papers. The quantity of water used during this process is important for the quality of the surface and also for the lifetime of the paper.

For the polishing process diamond products are used in combination of lubricants, instead of water. Lubricants ensure correct cooling and smearing of the sample surface. According to the material and the stage of the polishing process there are different types of lubricants. It is important to adjust the quantity of diamond in relation to lubricant. There are mainly three reasons for having good lubrication between the surface of the diamond cloth and the sample surface. These are:

. 1) Better cutting: The depth of the scratches and the plastic deformation are lower and therefore the quality of the polished surface is improved by lubrication.
. 2) Reduction of the friction: The friction between the sample and the cloth must be correct. Lack of lubricant causes over heating while too much reduces cutting capacity.
. 3) Cooling: Heat is generated between the sample and the cloth due to the friction. Good lubrication keeps low this heat.

Next, the preparation method with all the consumables used in each of the stages of the grinding and polishing processes is introduced.

Technical specifications of the preparation method in the Metalog Guide from "Struers" was followed [59]. This guide was publicated for samples prepared in automatic rotating plane discs where the cutting force, the rotational speed and time are also specified. In this case the sample preparation was done manually and thus all the requirements from the automatic processing was adapted to the manual grinding and polishing processes.

Struers preparation method depends on two physical properties: the Vickers hardness and the ductility of the material. The hardness is an easy measurable property of the material but it is not enough to determine the preparation method, and ductility which is the ability of the material to be plastically deformed needs to be also considered. The metalogram (figure 3.3) is divided in nine different regions with X-axis corresponding to the Vickers hardness and Y-axis corresponding to the ductility. According to the two criteria the materials are localized in one of the regions. The type of consumables are also specified for each of the regions.

Taking into account our materials, Cu, Pd and Ni are representative of different areas inside the regions B and D (see figure 3.3). Their values of Vickers hardness correspond to areas from left to the right of these regions, respectively. On the other hand, bismuth is a brittle material and has very low value of hardness and therefore it

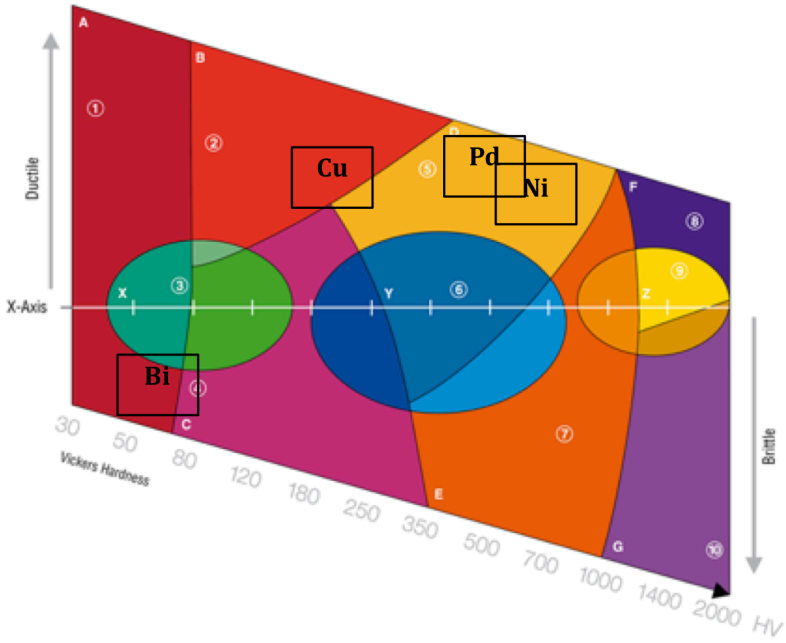

Figure 3.3: Struers metalogram for the preparation method. It is divided in nine regions that depend on the Vickers hardness and the ductility of the material [59]. The materials curved in our laboratory are indicated in their corresponding regions of the metalogram.

corresponds to the leftmost part of the metalogram in the region A. An electrolytic treatment was given to bismuth and copper samples after the polishing process for improvement of their surface quality. This treatment is out of the scope of the thesis. However, some details of the final results are later given.

The manual procedure to curve the surface of the crystals was defined following the specifications derived from the metalogram. As important as achievement of a mirror-like reflective surface without visible imperfections there are other requirements, which must be fulfilled by the MOKE and LEED experimental techniques.

1) MOKE setup: The spot of the incident beam laser must be reflected without distortion of the circular shape of the incident beam.
2) LEED: This technique is used to check the crystallographic quality of the surface by means of the diffraction pattern. The following conditions must be satisfied:

- Sharp spots in the [111] direction (centre of the sample) with high contrast and low background intensity.

- Splitting of the LEED spot into two separated spots when we move from the center to both sides of the crystal. No intensity between the spots indicates good definition of the steps of the surface.

- The hexagonal pattern characteristic of the fcc structure must remain unaltered when moving further along the [111] direction.

- Higher orders of diffraction must be observed when increasing the electron energy Regardless of the energy, the periodic structure must be the same.

All these requirements from both techniques must be satisfied before performing the experiments. Next, the steps followed in each of the stages of the grinding and polishing process are described.

- Grinding process

It was carried out through sequenced and ordered steps by the use of abrasives. SiC papers were used as abrasive and the grain size decreased along the successive steps of the process. The grinding procedure commonly starts with the smallest possible grain size of the abrasive for not damaging the sample.

  - Grinding with SiC paper: P320

The first SiC paper used is called P320 (in the European nomenclature) and it refers to nominal 40.5 microns of the grain size. Grinding with P320 paper was the longest stage of all the process because the majority of the material wass removed and the flat surface was converted into a curved surface.

  - Grinding with SiC paper: P500, P1200, P2400.

Once that the curvature of the crystal was obtained next stages were aimed to progressive reduction of the size of the scratches from the surface. Table 3.1 shows the ordered sequence of the SiC papers used in the process and also their corresponding nominal grain size:

Type of the SiC paper	Grain size (microns)
P500	30.2
P1200	15.3
P2400	6.5

Table 3.1: Ordered sequence of the abrasives with their corresponding grain size

The interval of the grain size between the stages was decreased approximately to half. This criterion was the optimum according to the final result seen on the curved surface. The size of the scratches on the surface was controlled in order to determine the end of the stage corresponding to each of the stages by means of a magnifier.

The process for each of the stages finished when the surface showed a homogeneous pattern with similar size of all the scratches. According to the interval between the grain sizes of the SiC papers, the new scratches had to be reduced approximately to half of the size. The grinding process finished after completing the three stages with P320, P1200 and P2400 SiC papers. Then the polishing process could be started.

- Diamond polishing process

Polishing removed the damage (scratches, embedded grains...) introduced by the grinding process. This was achieved with steps of successively finer abrasive particles. For this purpose, instead of the SiC papers, diamond products were used for the polishing process. Polishing was carried out on polishing cloths and always accompanied by a lubricant. The choice of cloth, diamond grain size and lubricant depends on the material to be polished. The type and characteristics of the consumables selected for the polishing process appears in order in table 3.2.

Diamond polishing consists of the last steps in the sample preparation process and most of the material has already been removed in the grinding process. The idea is to follow a progressive reduction in the size of the scratches in order to get a finer surface in each of the stages. Good cleaning of the cloth and tools during all this process is required for an optimum quality of the curved surface. If not removal of the new created scratches on the surface is more difficult because the size of the diamonds is small in the last stages. Mixing of different size of scratches creates difficulties to advance to the next stage.

The quality of the curved surface was checked at the end of the polishing process by the MOKE and LEED setups.

- MOKE: The surface quality of the curved crystal was tested outside the chamber. The spot of the incident beam had a good reflection from the polished sample, without distorted shape. For the test of the surface laser, lens, polarizer, analyzer and the photodetector were used (see the scheme in figure 3.4). Lens were used to focus the spot on the sample as it is done in practice for the MOKE measurements. Due to the curvature of the crystal the spot size in the horizontal direction elongates. The intensity of the reflected spot was measured with the photodetector. The intensity of the signal in the photodetector for MOKE measurements with flat samples is approximately 4.5 V. The sample was both moved horizontally and rotated for the analysis of the area from one side to the other of the curved crystal. The intensity deviated some tens or up to a maximum of one hundred milivolts which represented only about 1-2% of the total signal. This result was accepted because the deviation was very low. The intensity of the signal in the photodetector would be much smaller if the spot size extended after reflection.

Grain size (microns)	Type of cloth	Lubricant
3	High elasticity	Low protection
1	Low elasticity	High protection
0.25	Low elasticity	High protection

Table 3.2: Characteristics of the consumables for the polishing process

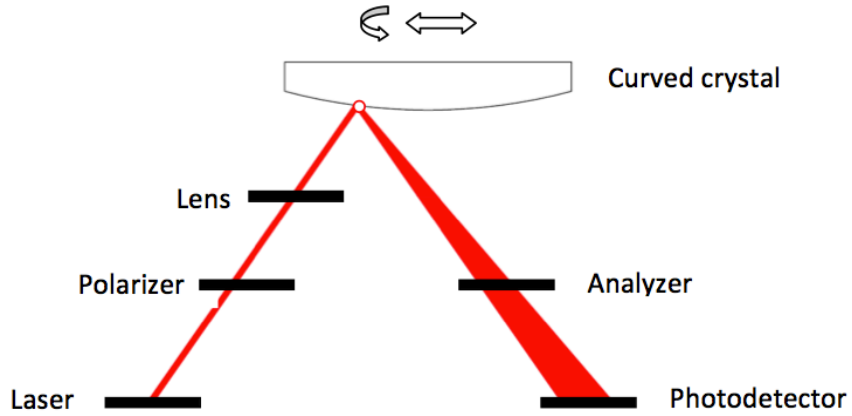

Figure 3.4: MOKE scheme for checking the size of the spot and the intensity of the signal from the polished curved surface

In fact, rough surfaces were tested and showed halo. This made it impossible to measure the MOKE signal by the photodetector.

- LEED: Sharp spots in the hexagonal pattern of the [111] direction and good splitting of the spots when moving to both sides of the crystal was required. The spots showed high contrast and low background intensity.

These two requirements were satisfied by the two polished crystals. The quality of the surface due to the mechanical process was also tested according to the R_a parameter. For this purpose, the curved surface of a Cu(111) single crystal was evaluated in different stages of the grinding process by means of the confocal microscopy technique. The analyzed surface was 3 mm x 3 mm area of the sample. This work was done in collaboration with "Cidetec" technological center and the results are summarized in table 3.3.

The roughness on the surface decreased with the use of finer abrasive papers. This result was expected because the use of progressively finer abrasives is aimed to decrease the size of the scratches on the surface. Two electrochemical polishing experiments were also carried out on this surface at different stages of the grinding and polishing process. The electrochemical polishing is a commonly used technique to achieve smooth surfaces for components used inside the ultra high vacuum system. It avoids excessive outgassing, such that the pressure in the system can be maintained in a low level. One of the most important advantages of this method is that it avoids

Stages of the grinding process	Ra (microns)
P500 (30.2 microns)	0.267
P2500 (6.5 microns)	0.193
1 micron	0.18

Table 3.3: Roughness of the Cu(111) surface for different grinding stages

deformations caused from the mechanical polishing and also risks of damage in the manipulation. This treatment basically consists of circulating a current from the anode to the cathode inside an electrolyte solution. The anode is the Cu single crystal and particles from its surface move to the cathode. An schematic example of the surface before and after the electrochemical process is shown in figure 3.5. The roughness of the electropolished surface was tested and compared with the results obtained only from the mechanical process, as it can be observed in table 3.4.

	Ra (microns)	
	Grinding process P2400 (6.5 microns)	Diamond polishing 1 micron
Mechanical process	0.193	0.18
Mechanical process + electrochemical polishing	0.0527	0.0429

Table 3.4: Roughness values for the grinding and polishing process for the mechanical process and for the mechanical process after the electrochemical treatment.

45nm surface roughness was achieved after the electrochemical polishing. Therefore, improvement of the surface quality was demonstrated with the treatment. There are two important advantages for the implementation of the electrochemical polishing in the process. These are:

1) Saving time
2) Avoiding risk from the mechanical polishing

To sum up, the mechanical process that covers all the grinding and polishing stages without the electrochemical treatment takes approximately 40 hours, as it is shown in figure 3.6. The electrochemical implementation significantly reduces the total time of the process and takes about 10 hours (the grinding process up to the P2400 stage included in the 10 hours) as it can be observed in figure 3.7. Final stages of the polishing process demonstrated to lengthen the total time of the process.

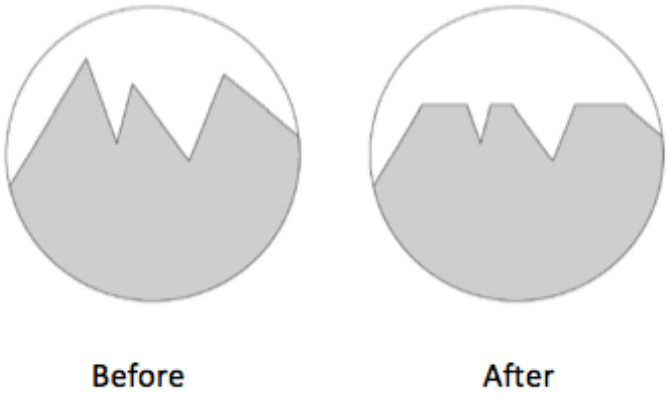

Figure 3.5: Schemes of a sample surface before and after an electrochemical treatment process

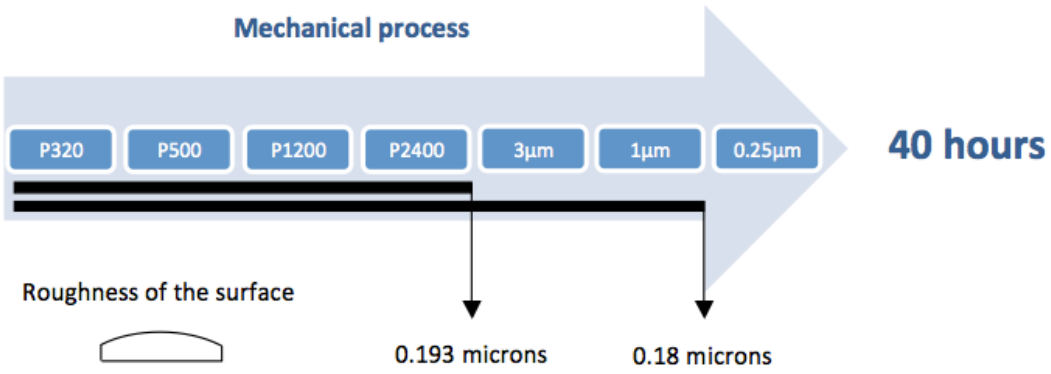

Figure 3.6: Duration of the mechanical process (grinding+polishing) without electrochemical treatment

Looking at the results obtained from the electrochemical experiments use of this technique showed interesting advantages in terms of surface quality and processing time. Excellent roughness values were reached with the analyzed Cu monocrystal. However, this technique in practice presents experimental difficulties since the electrolyte used in the chemical reaction must be tailored for each of the polished materials.

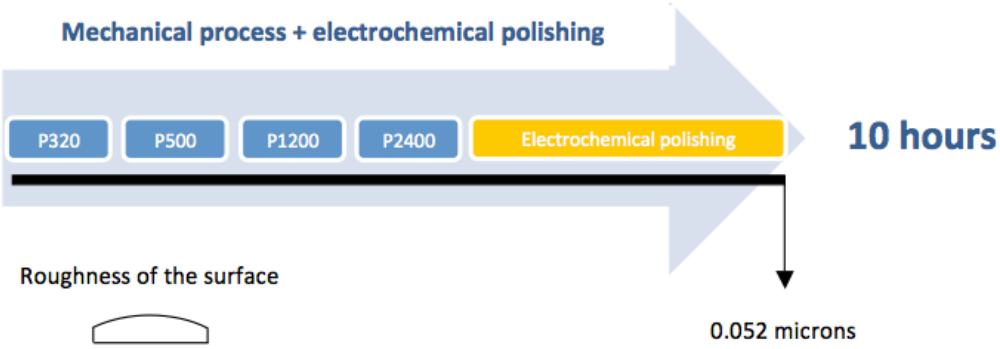

Figure 3.7: Duration of the process with the electrochemical treatment included.

4. Structural characterization of the curved crystals

This chapter is intended to present the results of the investigation of the microstructure of surfaces vicinal to the (111) plane of the single-crystal Pd and Ni. According to the general theory presented in the chapter 2.1 a high index plane making a small (miscut) angle with some low index plane can be unstable. In many cases a more energetically favourable structure having the same average orientation consists of flat terraces built of the closest low index atomic planes separated by atomic steps.

The regular array of steps making up a vicinal surface is shown schematically in the figure 4.1. An effective high index plane (the so-called optical surface) is represented by the dashed line. It is defined by the miscut angle α with respect to the low index surface. Parameters *d*, *L* and *h* stand for the step array periodicity, the terrace width and the step height, respectively.

The step height and the terrace width can be related by means of the miscut angle in the following way:

$$\tan\alpha = \frac{atomic\ step}{Terrace\ width} = \frac{h}{L} \quad (1)$$

The step height represents the distance between two crystallographic planes. According to basic crystallography for a cubic system this distance is given by:

$$h = \frac{a_0}{\sqrt{j^2 + k^2 + l^2}}, \quad (2)$$

where a_0 is the lattice constant and j, k, l are the indices defining the plane orientation. Pd and Ni both have Face Centred Cubic (fcc) crystal structure. This atomic arrangement may be represented as a periodic stacking of three atomic planes along the [111] direction in the sequence ABCABC as it is shown in the figure 4.2. A crosscut of the eight fcc unit cells by one of the (111) planes is shown in the figure 4.3 together with the main crystallographic directions. It is clearly seen that the least separated atomic rows run along the $[\bar{1}10]$, $[\bar{1}01]$ and $[0\bar{1}1]$ directions, therefore, atomic steps

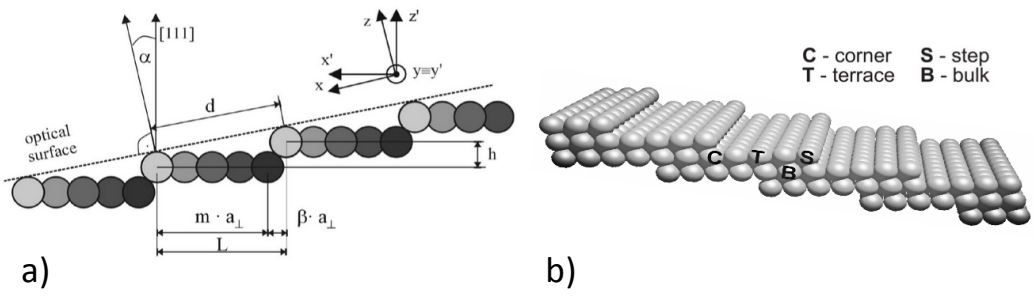

Fig 4.1: a) Side view of a vicinal surface with the most relevant parameters indicated. b) Schematic 3D view of the same surface [26].

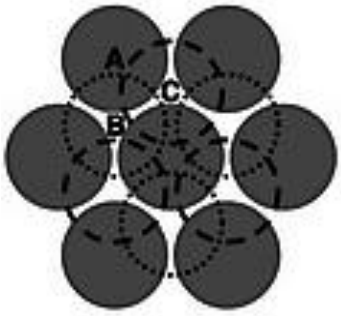

Figure 4.2: Schematic of the ABC stacking sequence for [111] direction of the fcc crystal

belonging to the vicinal planes parallel to one of these directions are less prone to the formation of kinks and tend to stay straight. The crystals used in this work were polished so that all vicinal planes are parallel to the $[\bar{1}10]$ direction. Therefore, the miscut angles are measured between the respective normal and the [111] axis towards $[11\bar{2}]$ or $[\bar{1}\bar{1}2]$ direction (see figure 4.4).

Though the arrangement of the atoms within the (111) plane has a six-fold symmetry the stack of the planes along the [111] direction demonstrates only a three-fold symmetry. The reason of the reduced symmetry is a non-equivalent position of the atoms of the top plane with respect to the lower ones. This non-symmetric behaviour is clearly seen for the descendent atomic steps towards $[\bar{1}\bar{1}2]$ and $[11\bar{2}]$ directions (see the figure 4.5). Depending on the chosen direction the vicinal surface displays two different types of microfacets at steps. In the $[\bar{1}\bar{1}2]$ direction, {100} microfacets appear, while in the $[11\bar{2}]$ direction the microfacets are {111}-like. Towards $[\bar{1}\bar{1}2]$ direction the atoms are arranged for the descendent planes one in front of the other. However, in the $[11\bar{2}]$ direction the position of the atoms does not coincide and each of the top layer atoms is situated between two atoms of the lower plane.

For the chosen geometry and crystal structure the terraces of the vicinal surface are formed by the (111) atomic planes therefore according to the equation (2), the step

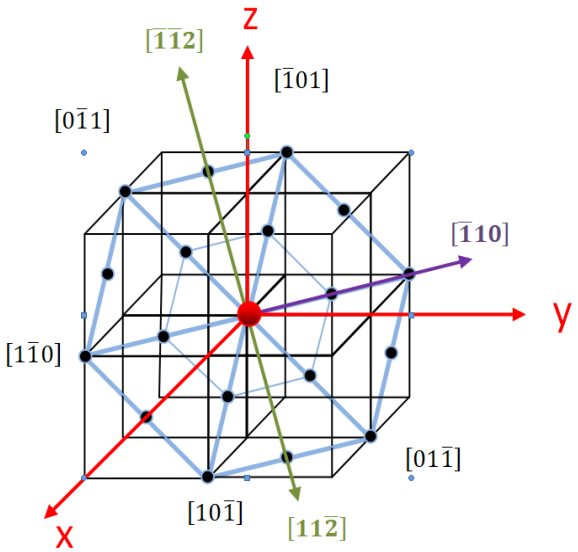

Figure 4.3: Schematic representation of the crosscut by the (111) plane of eight unit cells of the fcc crystal

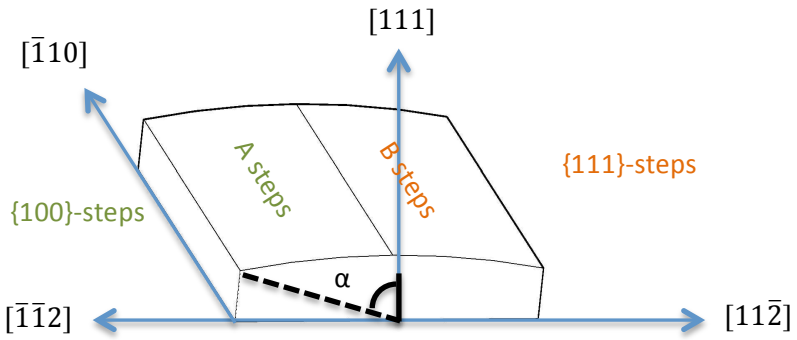

Figure 4.4: Scheme of the curved crystals with indications of main directions and type of steps

height is equal to the respective interplane distance:

$$h = \frac{a_0}{\sqrt{3}} \quad (3)$$

Using equations (1) and (3) the terrace width L can be written as a function of the miscut angle α and the lattice constant a_0 in the following way:

$$\mathrm{L} = \frac{\mathrm{a_0}}{\sqrt{3}\tan\alpha} \quad (4)$$

The terrace width L can also be also expreesed using the effective number of atomic rows $\bar{n}$ in the terrace and the distance between two atomic rows $\mathrm{a}_\perp$:

$$L = \bar{n}\,\mathrm{a}_\perp \quad (5)$$

The asymmetry in the step structure gives rise to the different terrace widths for each type of the steps. According to the mentioned asymmetry, for {100} steps the terrace width can be written as $\mathrm{L} = (\mathrm{n} + 2/3)\mathrm{a}_\perp$, while for {111}-steps the terrace width is $\mathrm{L} = (\mathrm{n} + 1/3)\mathrm{a}_\perp$, where $\mathrm{a}_\perp$ is the interatomic distance in the direction

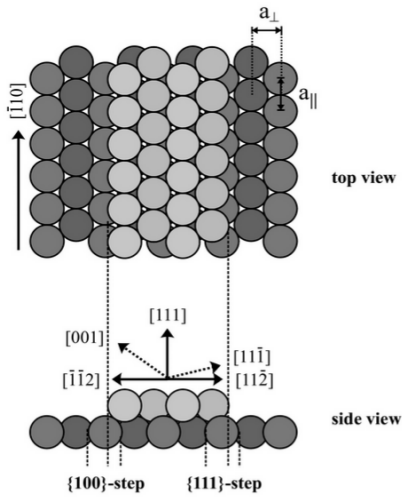

Figure 4.5: Schematic top view and side view of the two microfacets in the crystal. In the direction $[\bar{1}\bar{1}2]$, appear the {100}-microface known as A-type and at the other side, in the $[11\bar{2}]$ direction, the {111}-microface is known as B-type. In both cases, the steps run along $[\bar{1}10]$ direction [26].

perpendicular to the step and n is the number of the atomic rows [26].

Figure 4.3 shows that a crosscut of one fcc unit cell by the (111) plane contains six atoms. Therefore a side of the triangle shown in the figure 4.6 is a diagonal of face of the cubic unit cell which is equal to $a_0\sqrt{2}$ and the distance between the atoms within the atomic row $a_{\parallel}$ is given by:

$$a_{\parallel} = \frac{a_0\sqrt{2}}{2} = \frac{a_0}{\sqrt{2}}$$

Since this triangle is equilateral its height and side are related as follows:

$$\sin 60 = \frac{2a_{\perp}}{a_0\sqrt{2}}$$

and the distance between the rows is given by:

$$a_{\perp} = \frac{\sqrt{3}}{2\sqrt{2}} a_0$$

Eventually, equations (4) and (5) allow to express the terrace size for a certain miscut angle in terms of the number of effective atomic rows $\bar{n}$ in the terrace as follows:

$$\bar{n} = \frac{2\sqrt{2}}{3\tan\alpha} \quad (6)$$

where $\bar{n} = n + 2/3$ and $\bar{n} = n + 1/3$ in the case of {100} steps and {111} steps respectively.

We can also calculate the atomic surface density of the (111) plane of the fcc crystal lattice using the same triangle in the figure 4.6. Since it represents the (111) section of the cubic unit cell of the fcc lattice, the three atoms in the corners contribute 1/6 each and the ones on the side contribute 1/2. Then, there are a total of 2 atoms per area of the equilateral triangle with side of $a_0\sqrt{2}$. The inverse atomic surface density of (111) plane is therefore:

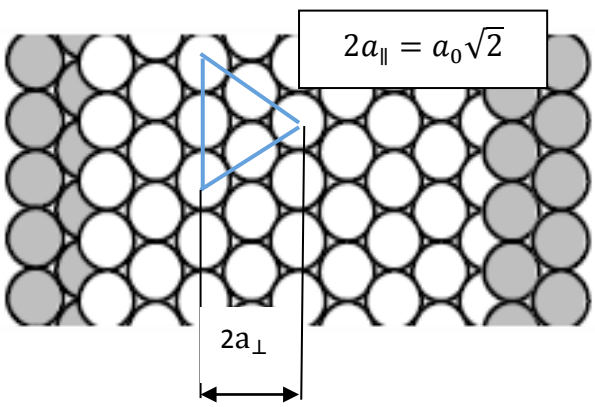

Figure 4.6: Top view of the (111) surface of a fcc crystal

$$S_{atom} = \frac{S_{triangle}}{n_{atoms}} = \frac{\frac{1}{2} a_0 \sqrt{2} 2 a_\perp}{2} = \frac{a_0^2 \sqrt{3}}{4}$$

Relevant crystallographic parameters of the fcc(111) and vicinal surfaces of Pd, Ni and Co are given in table 4.1. Data for cobalt are appended because this information will be used in chapter 5 to discuss the growth of Co islands on both curved crystals.

Equation (1) giving the relationship between the terrace width and the miscut angle of the vicinal surface is correct only when the terraces are separated by the equal (monoatomic) steps. However, our STM data presented in chapters 4.2 and 4.3 show that the real vicinal surfaces feature two- and three-atom high steps therefore a generalization of the equation (1) should be developed. Basic observation which allows to generalize this formula tells that a biatomic step appers when two monoatomic steps merge and the size of the terrace next to this step is roughly twice the size of the regular terrace.

According to figure 4.7 a miscut angle α between the optical plane and the (111) plane can be expressed in the following way:

$$\mathrm{tg}\,\alpha = \frac{H}{L_{total}} = \frac{N_1 h + N_2 2h}{N_1 L_1 + N_2 L_2}$$

where N_1 and N_2 are the number of monoatomic and diatomic steps, *h* is the height of monoatomic step, L_1 and L_2 are the widths of the terraces next to monoatomic and diatomic steps, respectively. If we take the second part of the equation and divide both the numerator and denominator by the total number of terraces (N_1+N_2) it reduces to:

$$\frac{h\left(\frac{N_1}{N_1+N_2} + \frac{2N_2}{N_1+N_2}\right)}{\frac{N_1 L_1 + N_2 L_2}{N_1+N_2}} = \frac{h\left(\frac{N_1}{N_1+N_2} + \frac{2N_2}{N_1+N_2}\right)}{< L >} = \frac{h}{L_{eff}} \qquad (7)$$

where <L> is the mean value of the terrace width for all the terraces (monoatomic and diatomic). The effective terrace width L_{eff} is a function of the miscut angle α. According to (7) L_{eff} is given by:

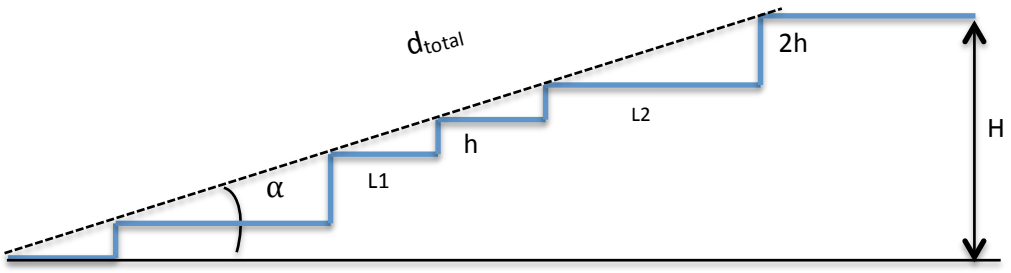

Figure 4.7: Stepped structure featuring one and two atoms high steps

$$< L_{eff} \geq \frac{< L >}{\frac{N_1}{N_1 + N_2} + \frac{2N_2}{N_1 + N_2}} = \frac{< L >}{p_1 + 2p_2} = \frac{< L >}{2 - p_1} \quad (8)$$

$$p_1 + p_2 = 1$$

where p_1 and p_2 are the probabilities of having one and two atoms high steps, respectively. If the stepped surface is formed by monoatomic steps only, p_1 is equal to 1 and L_{eff} is equivalent to the average terrace width L from equation (1). If the vicinal surface contains higher steps the general formula for the effective terrace width obviously reads:

$$< L_{eff} >= \frac{< L >}{p_1 + 2p_2 + 3p_3 + \cdots} \quad (9)$$

where p_i stands for the probability to have the *i* atoms high steps.

Face	a_0(Å)	*d*(Å)	$a_\perp$(Å)	$a_\parallel$(Å)	S_{atom}(Å^2/atom)
fcc(111)		$a_0/\sqrt{3}$	$a_0\sqrt{3/8}$	$a_0/\sqrt{2}$	$a_0^2\sqrt{3}/4$
Pd	3.89	2.24	2.38	2.75	6.55
Ni	3.52	2.03	2.16	2.48	5.36
Co	3.55	2.05	2.17	2.51	5.46

Table 4.1: Crystallographic prameters of the fcc(111) surfaces. a_0 is the lattice constant, *d* the interlayer separation, $a_\perp$ and $a_\parallel$ are respectively the perpendicular and parallel interatomic distances of the steps in the vicinal surface shown in figure 4.4 and S_{atom} is the surface density per atom [26].

4.1 Clean curved Pd(111)

Curved Pd crystal has been polished around the [111] high-symmetry direction in our laboratory (see details of the procedure in the section (3). The size of the sample (9x9mm^2) and its shallow curvature (R=23.2 mm) facilitate mounting on the standard Omicron type sampleholder and guarantee the accessibility with the STM along the curvature of the crystal.

The miscut angle range of $\alpha=\pm 11^0$ enables us to examine the {100} (A-type) step side and {111} (B-type) step side of the stepped surface vicinal to the (111) plane. This surface encompasses the (557) plane at $\alpha=+9.4^0$ (the positive miscut angle has been taken in the $[\bar{1}\bar{1}2]$ direction), which exhibits 13.5 Å wide terraces (5+2/3 atomic rows) at the side of {100}-like (A-type) steps and the (332) plane at α=-10º, with 12.7 Å wide terraces (5+1/3 atomic rows) on the side of {111}-like (B-type) steps. This sample is schematically shown in figure 4.4.

The in situ preparation has been done in the UHV chamber by means of usual cycles of sputtering and annealing. Sputtering has been performed with 1 KeV energy of the argon ion beam, in grazing incidence (60^0 off the normal) with the ion beam incidence plane parallel to the surface steps. Each of the sputtering cycles has been carried out in five different positions within +/-2 mm off the sample's center for 3-5 minutes each in order to guarantee the thorough cleaning of the whole surface. The beam current measured in the grounding circuit was of 3-6 μA at argon pressure of $p=1.10^{-6}$ mbar. The annealing of the vicinal surfaces is more critical than that of the flat surfaces because mobility has to be supplied to atoms of the terraces and also of the steps. Furthermore, the lateral structure of the steps must be maintained in order to create a regular array of steps. The e-beam heating with the voltage of 1 KV and emission current of 30 mA had been used to reach the temperature of 730-760 ºC. The duration of the annealing was of 10 min and the final pressure has been kept below 5.10^{-9} mbar. The structure of the curved surface has been initially explored with Low Energy Electron Diffraction (LEED). For the LEED experiment, we have moved the sample laterally along the $[11\bar{2}]$ direction and taken the images with a step of 0.5-1 mm across the entire curved surface. The energy of the beam was of 82.7 eV.

Figure 4.8 (a-h) shows the hexagonal pattern of the (111) terraces and also exhibits the characteristic splitting of the diffracted spots observed in stepped surfaces (see part 2.2 LEED). In general, figures from (a) to (h) show sharp spots with low background intensity and well defined splitting of the spots, which indicate good crystal quality. The hexagonal structure is indicated in the figure 4.8 (a). The side of the hexagon is given by $2\pi/a_\perp$ where $a_\perp$ is the interatomic distance of the hexagonal pattern in the real space (in the direction perpendicular to the steps). The spots are split due to the diffraction from the step array in the direction perpendicular to the steps. The size of

the splitting is 2π/d which gives the average terraces width in the point of the measurements.

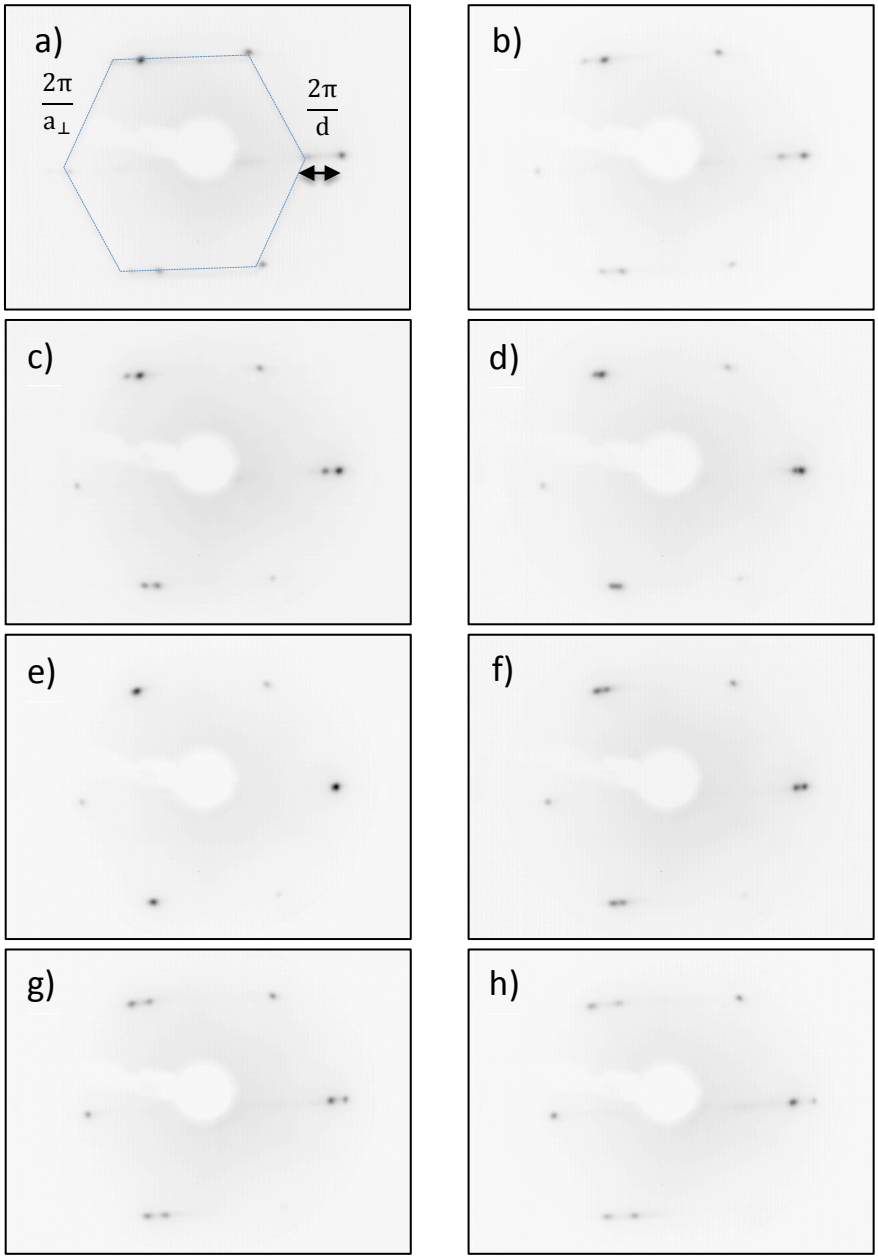

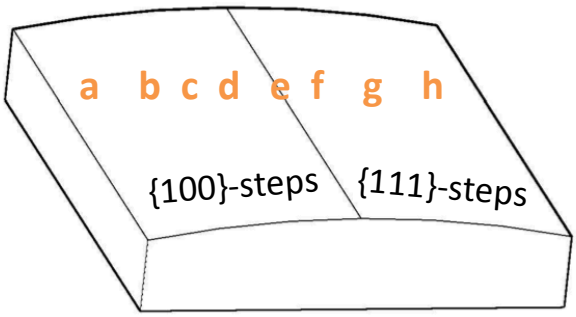

Figure 4.8: LEED patterns measured by scanning across the surface of cPd(111), E_0 = 82.7 eV and indication of the positions of the corresponding LEED patterns on the curved sample.

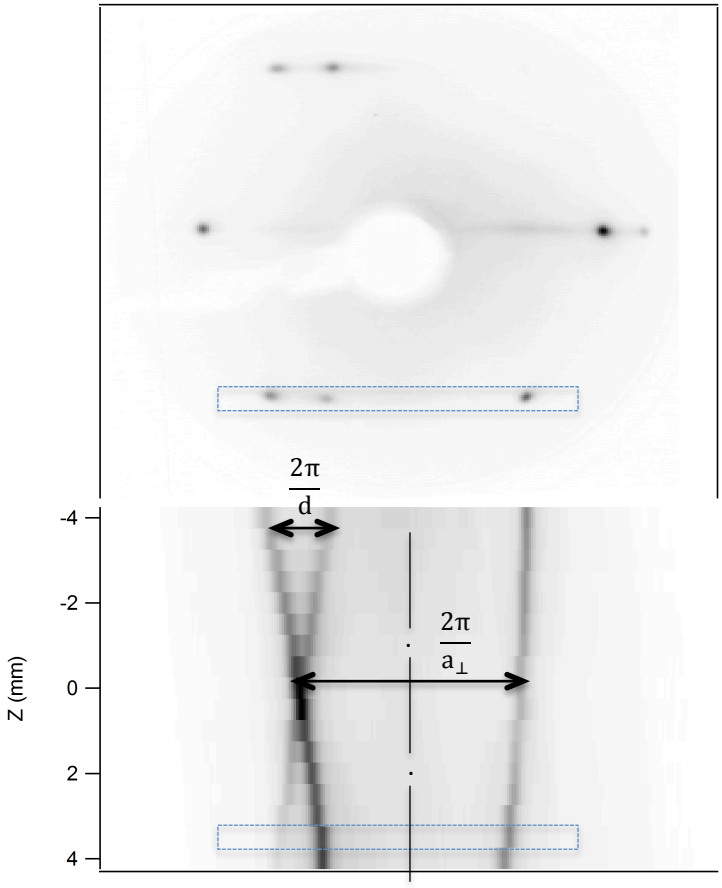

Figure 4.9: a) The top panel shows the LEED pattern taken at 4mm from the center. b) Spatial variation of the splitting. The box indicates the part of the top panel that is selected in the lower panel screen.

Our set of the LEED images allows to trace the variation of the average terrace width as a function of the miscut angle if we follow the value of the splitting of a certain spot. Indeed the upper panel of the figure 4.9 shows a LEED pattern collected in the position 4 mm apart from the center of the crystal (along the $[11\bar{2}]$ direction). The blue rectangle marks two spots which we used to build the spatial profile of the splitting. The lower panel shows the image constructed from the separate LEED patterns. Each horizontal line of the image represents a crosscut of the respective LEED pattern along the marked line. The vertical coordinate of the line shows position of the measurements and horizontal axis gives a value of splitting for all the LEED patterns in the same arbitrary units. If one builds a vertical stack of aligned LEED patterns, making the z coordinate equal to the point of measurements this plot would represent a cut of the stack by a vertical plane containing the (10) and (11) spots of each pattern.

The gradual variation of the spot splitting is seen at both sides of the crystal. Although for shallow curvature and small angles, the miscut angle is a linear function of the position (2.4 ^{0}/mm), the splitting does not change linearly. According to the equation (1) from Section 4 the splitting $2\pi/d$ is proportional to the $\sin\alpha$. It is linear in the limit

of small α but becomes slightly nonlinear when α approaches the values corresponding to the edges of the sample. The clear separation between the split spots indicates that the curved crystal features a regular array of atomic steps in the real space. Moreover, the splitting is homogeneous and symmetric with respect to the center of the crystal. Thus, the curved Pd(111) surface consists of atomic step arrays with smooth variation of the step density and does not show step bunching or faceting.

As it was mentioned in the part 2.2, LEED is a spatially averaging technique that probes an area with diameter of 80-100 microns. Since the averaged data may loose some local features of the surface microstructure we have collected STM images in different points along the curvature of the crystal.

Figure 4.10 shows STM topography image of the central part of the Pd crystal (miscut angle $\alpha=0^0$). Large terraces are separated by relatively straight monoatomic steps. The terrace width is bigger than 100 nm, which is comparable with the terraces of a nominally flat Pd (111) crystal. The image demonstrates that the surface is free of contamination.

Since the terraces are essentially flat, the most interesting information about the microstructure of the stepped surface concerns the shape and the height of the steps. These details are more visible in the derivative plots than in the topography images. Therefore in the next figures only derivative plots are presented together with profiles measured in the original topography images. Respective miscut angles are calculated using the average terrace width obtained from the statistical analysis of the images (see details below).

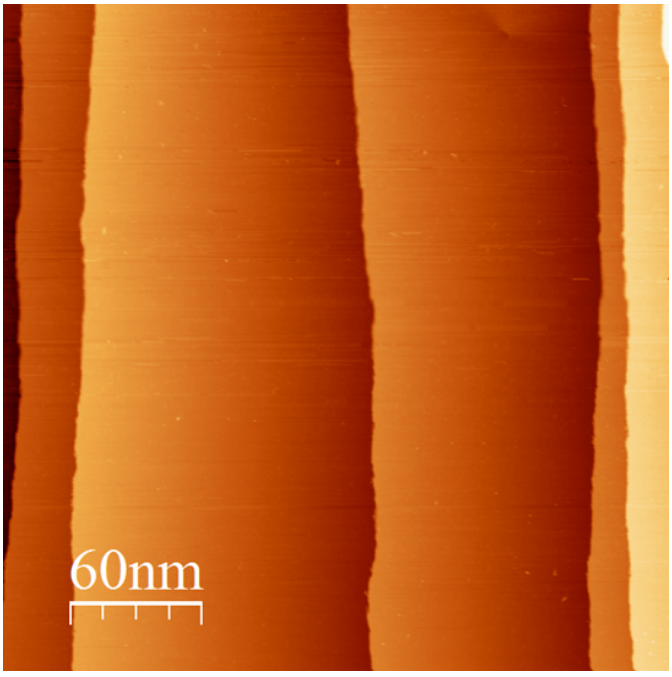

Figure 4.10: STM image (300nmx300nm^2) taken at $\alpha=0^o$ miscut angle of the curved Pd(111)

Figures 4.11 (a), (c) show STM images taken at low miscut angles of 0.8^0 and 1.9^0 along the $[11\bar{2}]$ direction ({111}-type steps) of the curved Pd(111). Both areas are characterized by low density of steps and according to the profiles (figure 4.11 b, d) the surface features only monoatomic steps. Next two STM images (figure 4.12 a,d) are taken along the same direction but further from the center of the crystal at the positions with α of 3.3^0 and 6.3^0. Neither of these images demonstrates faceting which corroborates the results of the LEED measurements.

Nevertheless figure 4.12 (a) shows that in two cases adjacent steps apparently merge which leads to the appearence of the line with more intense color. Zoom of the upper-right corner of the image (figure 4.12 b) and the profile (figure 4.12 c) show that respective step has twice the height of the regular step. Therefore these two darker lines were attributed to the presence of the diatomic steps. Figures 4.12 (d-f) show that a vicinal flat surface with a miscut angle of 6.3^0 presents two-atoms-high steps. Although the number of diatomic steps increases with increasing step density, the relative amount of these steps is still low and does not affect the LEED pattern.

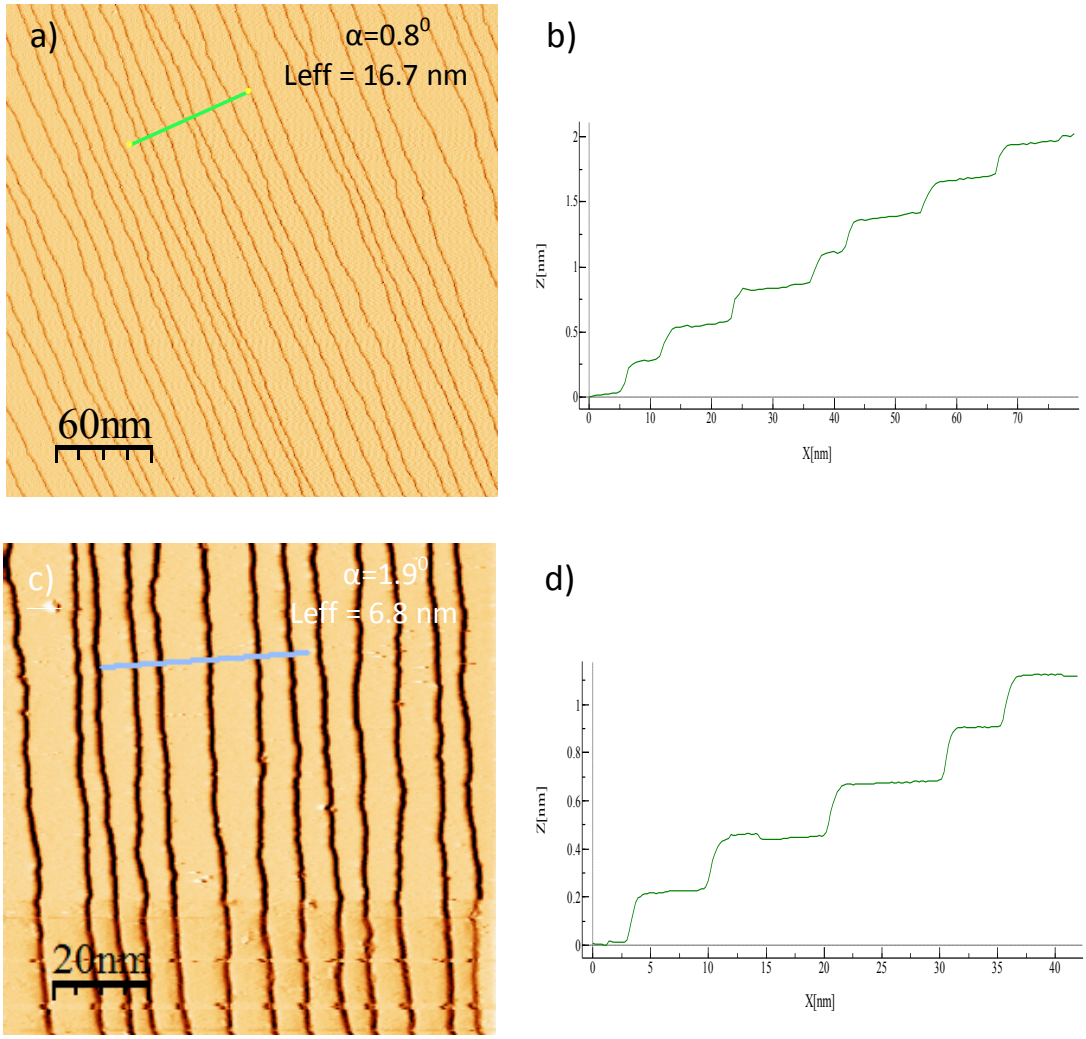

Figure 4.11: a) 300x300nm^2 STM image at α=0.8º miscut angle showing {111}-type steps, b) profile of the figure (a), c) 100x100nm^2 STM image at α=1.9º miscut angle, d) profile of the figure (c)

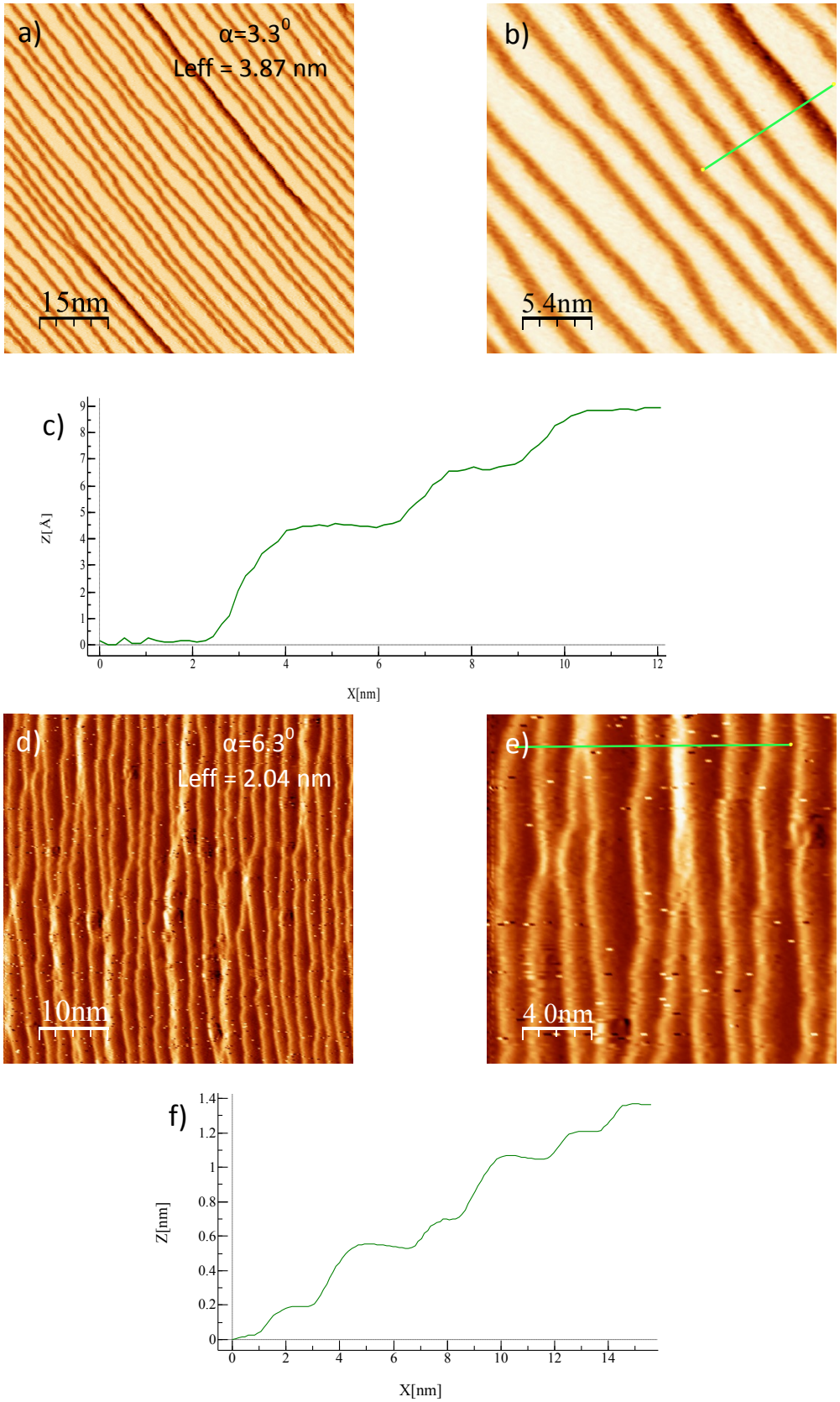

Figure 4.12: a) Derivative of the STM image (75x75nm^2) taken at α=3.3º for the curved Pd(111) at the side of {111} type steps, b) zoom of the figure (a), c) profile of the Figure (b), d) derivative of the STM image (50x50nm^2) taken at α=6.3º, e) zoom of the figure (d), f) profile of the figure (e)

Now we will focus on the side of {100}-type steps which correspond to the $[\overline{11}2]$ direction with respect to the center of the crystal. Figures 4.13 (a, c) show two STM images taken in the central and intermediate regions of the crystal (miscut angles are 1.6^0 and 2.7^0 respectively). As demonstrated by the profiles (Figure 4.13 b, d) in both cases surface features only monoatomic steps. However, the morphology of the steps is completely different in these areas. Closer to the center of the crystal the steps are straight and a variation of the terrace width is concerned with coexistence of wider and narrower terraces. On the contrary, in the intermediate zone steps are prone to meandering and thus the terrace width varies stronger along the terrace.

Figures 4.14 (a,d) illustrate the STM images of the crystal at miscut angles of 3.7^0 and 4.2^0. The higher miscut angle gives rise to smaller average terrace width. Figure 4.14 (a) shows the abundance of the monoatomic step on the surface and rare presence of the diatomic steps. Steps are straight and meandering is not pronounced in these regions. Figure 4.14 (d) represents the area closer to the edge of the crystal. According to the STM image the surface features mainly monoatomic steps but some diatomic steps are also observed. Steps remain relatively straight and once merged they stay coupled on the scale of the STM frame.

The overall results of the STM characterization are compatible with data of LEED. The

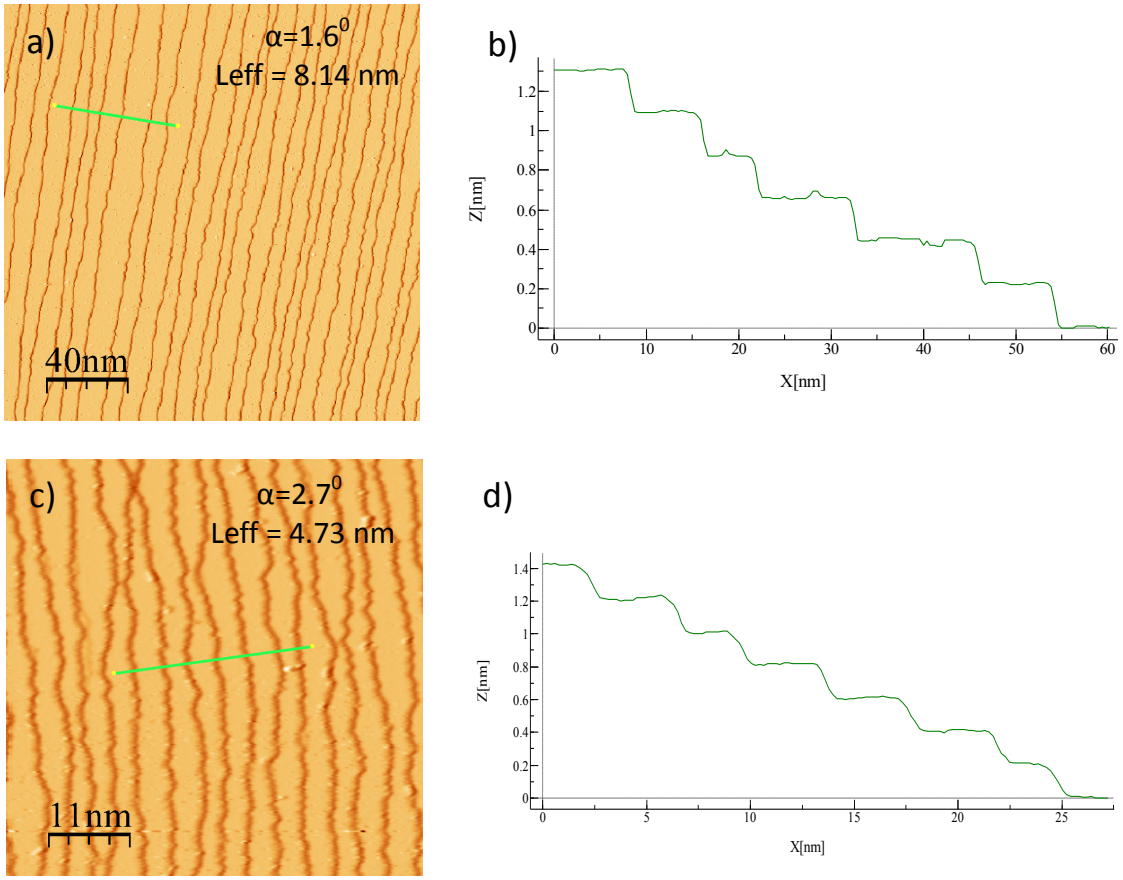

Figure 4.13: a) 200x200nm^2 STM image at α=1.6º miscut angle showing {100}-type steps, b) profile of the figure (a), c) 55x55nm^2 STM image at α=2.7º miscut angle, d) profile of the figure (c)

vicinal surface is found to be a periodic array of flat terraces separated by relatively straight monoatomic steps. The relative amount of diatomic steps is low and therefore they have not been detected in the LEED patterns.

In addition to the local high-resolution data showing the morphology of the surface, STM images allow to obtain a statistical information about the terrace width distribution (TWD) which depends on the type and strength of the step-step interaction (see chapter 1).

The procedure that has been used to extract the statistical information from the STM images consists in individual analysis of each of the STM frames (512x512 pixels) which features between 15 and 30 terraces. Depending on the terrace width the frame sizes

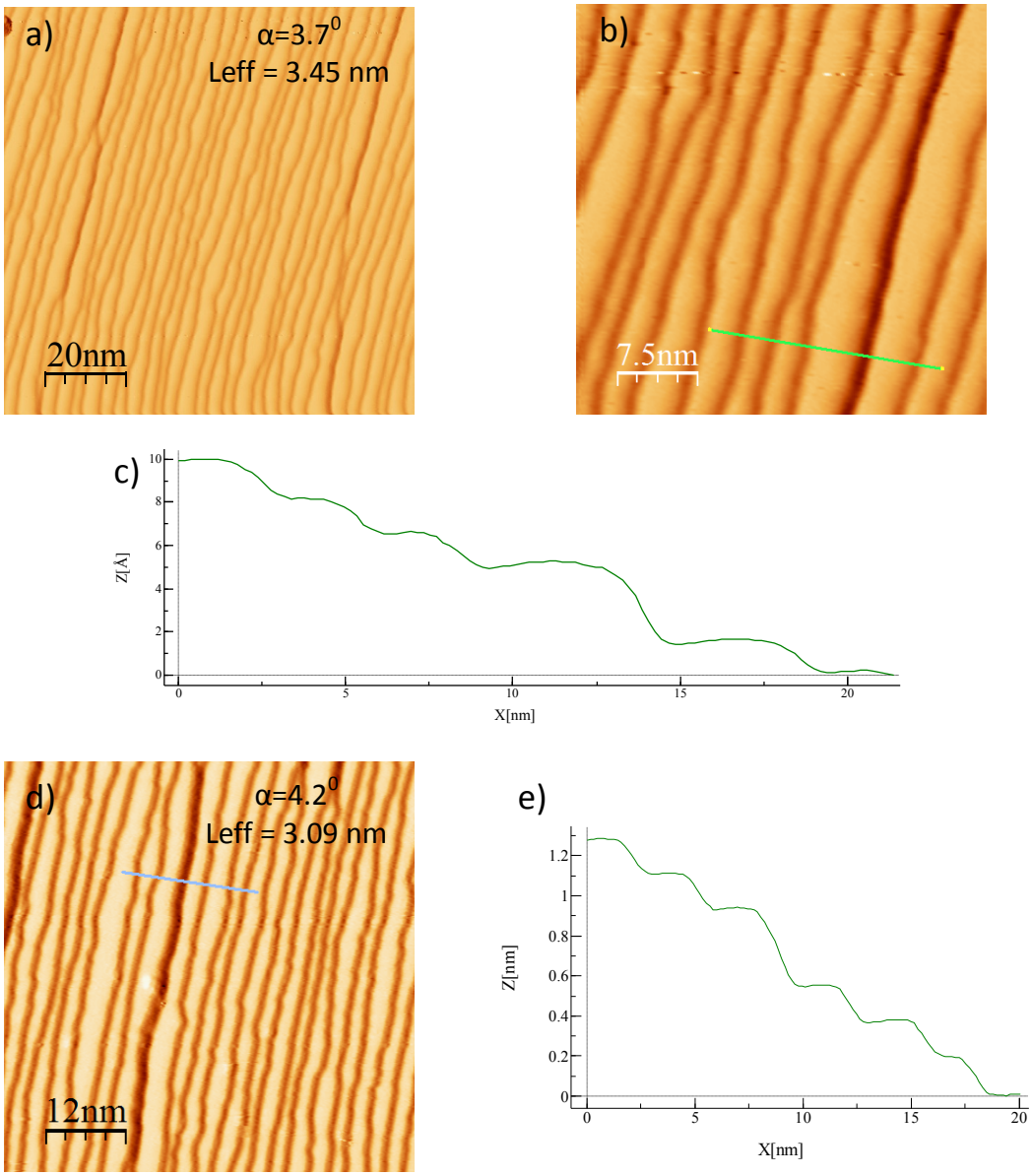

Figure 4.14: a) derivative of the STM image (100x100nm2) taken at α=3.7º for the curved Pd(111) at the side of {100} type steps, b) zoom of the figure (a), c) profile of the figure (b), d) derivative of the STM image (60x60nm2) taken at α=4.2º, e) profile of the figure (d)

were between 40x40 and 300x300 nm^2. We take the STM topography image (costant current mode) and apply the derivative filter (see figure 4.15 c and e). The program for the automatic processing of the individual STM images extracts the profile of each scan and calculates the distances between the adjacent steps. Figure 4.15 (d) and (f) show the profiles of both the topography and derivative images, respectively. It is clearly seen that the steps in the topography image are converted in the dips of the derivative

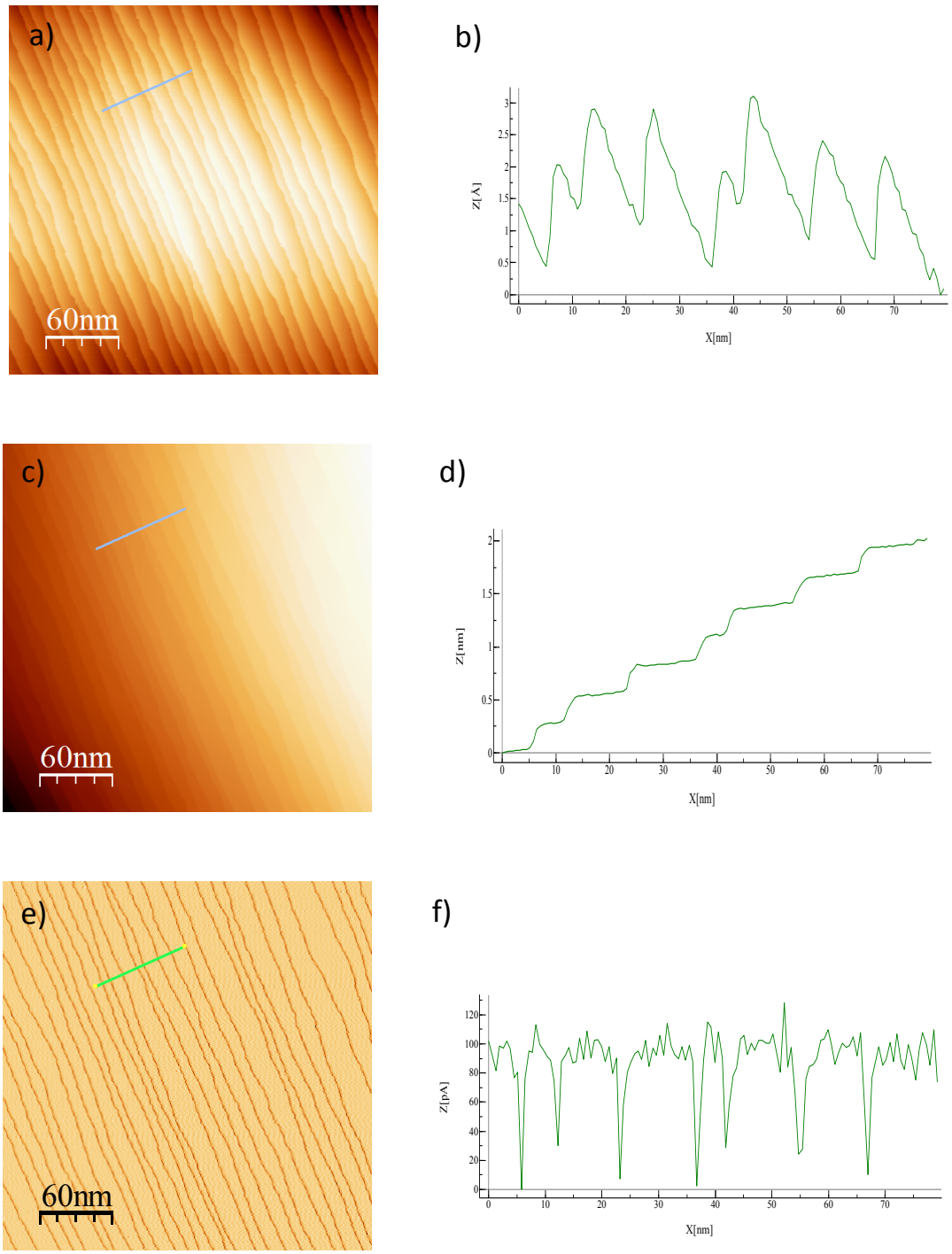

Figure 4.15: a) Original STM topography image (300x300nm^2), b) profile of the figure (a), c) STM image after application of the local plane on one of the terraces, d) profile of the figure (c), e) derivative (inverted) of the STM topography image, f) profile of figure (e)

image. This transformation allows to calculate the terrace width as a distance between the adjacent minima which is a more convenient task for the algorithmic process than tracing of the steps in the original image.

The raw STM topography images do not look like the image shown in the figure 4.15 (c) but they are rotated so that the average tangent plane (the optical plane in the figure 4.1) is horizontal (see figure 4.15 a). To avoid transformation of each image (which takes a lot of time) we apllied derivative filter to the original images directly. The distance between the dips of the derivate image in this case gives the period of the stepped surface measured in the optical plane (distance d in the figure 4.1 a). This parameter is clearly related to the average terrace width as:

$$\frac{L}{d} = \cos\alpha$$

and therefore d is almost equal to L for small miscut angles α. In the next discussion the average distance d will be used as the approximation of the average terrace width *L* but for the conversion of this value to the respective miscut angle $\sin\alpha$ is used in the equations (1) and (7) instead of $\tan\alpha$.

Figure 4.16 shows hystograms of the terrace width distributions corresponding to the STM images shown in the figures 4.11 (a), (c) and 4.12 (a), (d) ({111}-type steps). To

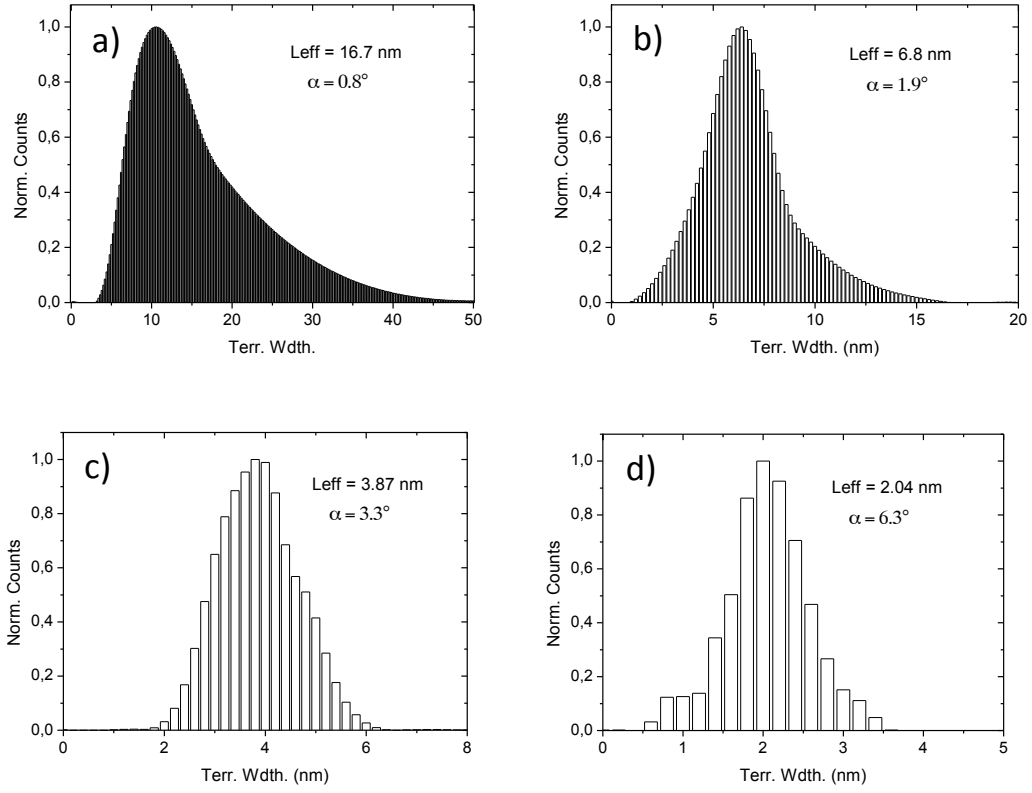

Figure 4.16: a) Terrace width distributions which corresponds to the STM image from the fig. 4.11. {111}-type steps, α=0.8º. b) α=1.9º. c) α=3.3º. d) α=6.3º

improve the statistics, each histogram was built out of three different STM images taken side-by-side in the same zone. Therefore, the images 4.11 (a), (c) and 4.12 (a), (d) can be considered as representative examples of the respective datasets. In general the shape of the distributions obeys the tendency predicted by the theory of the chapter 2.1. The characteristic behaviour of the distributions in the regions close to the center (a non-simmetric broadening in the range of of the wider terraces) changes gradually as a function of the miscut angle. For high miscut angles strong elastic step-step interaction dominates and results in narrower and more symmetric shape of the peaks.

However, the distributions corresponding to the STM images 4.13 (a), (c) and 4.14 (a), (d) ({100}-type steps) demonstrate more complex behavior. The TWD shown in the figure 4.17 (a) characterizes the area closest to the center of the crystal ($\alpha=1.6^0$). The distribution has a shape similar to the one observed in the respective zone on the side of the {111}-type steps (figure 4.16 a). Its pronounced asymmetric peak is shifted towards smaller values of the terrace widths, as commonly observed in the regions with the entropic step-step interactions.

Figure 4.17 (b) shows different type of distribution of the terrace width. The main peak represents the width of the majority of the terraces in this area but also there is a minor peak with a height approximately 1/3 of the height of the first peak. This

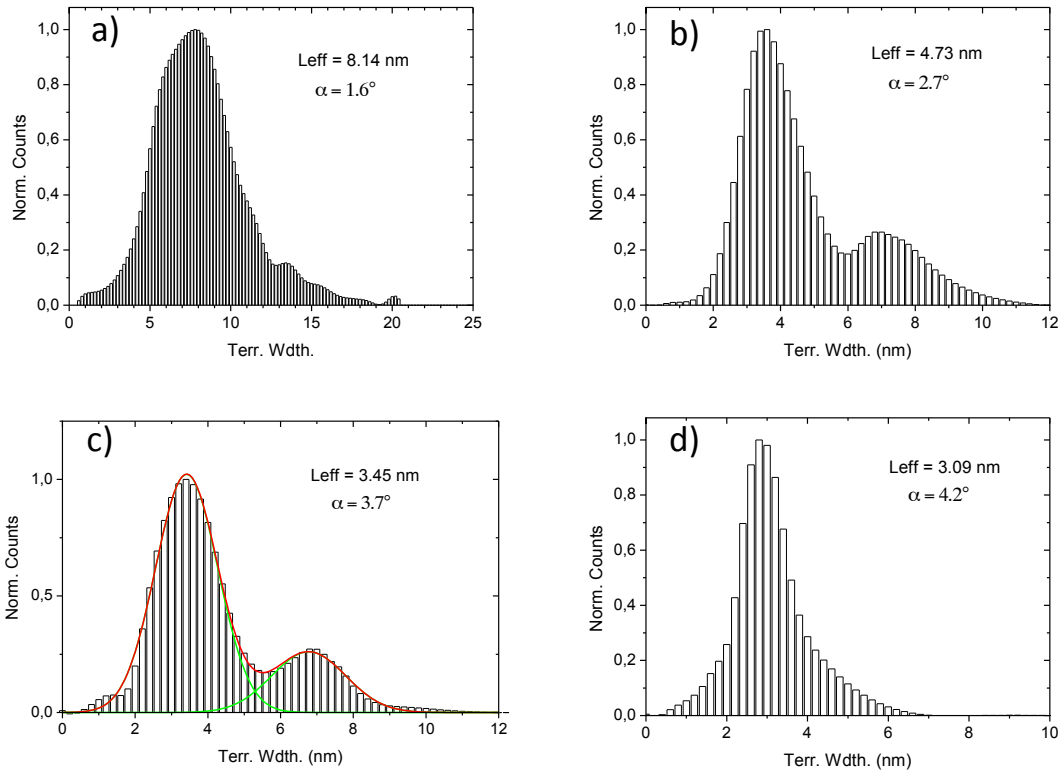

Figure 4.17: a) Terrace width distributions which corresponds to the STM image from the fig. 4.13. {100}-type steps, α=1.6º. b) α=2.7º. c) α=3.7º. d) α=4.2º

distribution corresponds to the STM image 4.13 (c) where all steps were found to be monoatomic but prone to strong meandering. Two peaks in the TWD demonstrates that in this zone there are two characteristic width of terraces which are energetically more favorable than others. These “magic” terrace widths have been observed previously in the vicinal surfaces of the Au(111) and were attributed to the correlation of the periods of the stepped surface and herring-bone reconstruction [6]. Figure 4.17 (c) shows again a distribution with two peaks. It corresponds to the part of the crystal represented by the STM image 4.14 (a) ($\alpha = 3.7^0$). According to the STM data some minor amount of diatomic steps was observed in this zone. Since two atoms high steps appear as a result of merging of two regular steps the adjacent terrace is usually wider than the regular one. Therefore, the lower peak of the distribution can be attributed to the presence of these bigger terraces next to the diatomic steps.

It was shown in the previous part of this chapter that the coexistence of the atomic steps with different heights complicates convertion of the average terrace width into the respective value of the miscut angle. For equation (1), in this case, we should use the effective average terrace width L_{eff}, defined by means of the equations (8) or (9).

In order to estimate the probabilities of the formation of mono- and diatomic steps the distribution from the figure 4.17 (c) has been fitted to the sum (shown by the red line) of two Gaussian peaks (shown by green lines). Positions of the peaks give an approximation of the average terrace widths and the relative area of the peaks is equal to the respective probabilities. Results of fitting and the effective terrace width calculated by means of equation (8) are shown in figure 4.17 (c), together with the experimental terrace width distribution. The probability of the formation of the diatomic steps in this case was found to be 0.233. It should be stressed that corresponding LEED pattern does not show additional split spots (see figure 4.9), therefore the wider terraces adjacent to the diatomic steps do not form any periodic structure.

Finally, the distribution corresponding to the miscut angle $\alpha = 4.2^0$ (figure 4.17 d) shows a narrower and predominant single peak. The region is characterized by a defined size of the terrace width and the presence of ocasional double steps is not big enough to broaden this single peak. The shape of this distribution is symmetric and could be defined as Gaussian like. This is common feature of regions with high density of the steps where the distributions are driven by the elastic step-step interactions.

Next, we will summarize the data obtained by means of the statistical treatment of all the STM images. We have built the plot shown in figure 4.18 with all the histograms obtained across the curved surface. Each horizontal line of the plot represents one histogram where the values are coded with colours. The Y- coordinate of the histogram shows the effective average terrace width, which coincides with the mean terrace width when the steps are monoatomic.

The yellow straight line is plotted at 45^0 and therefore it crosses each histogram in the point whose X-coordinate is equal to the effective average terrace width of the histogram. For the histograms which represent symmetric distributions the crossing point should coincide with the position of the maximum of the histogram (the darkest

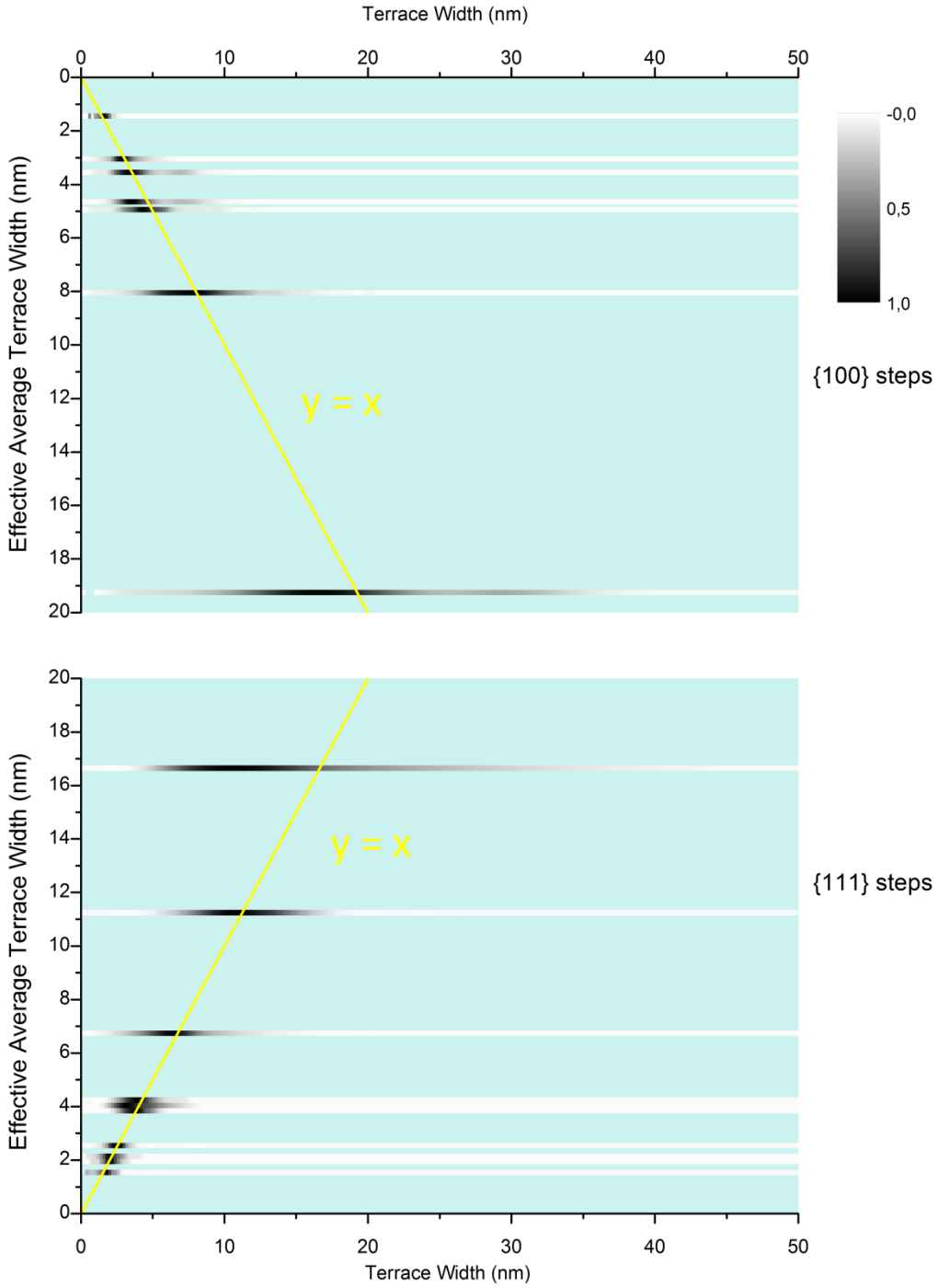

Figure 4.18: Image plot of the curved Pd(111) surface built with all the probability histograms at different mean terrace values <L>. Histograms are individually normalized to the maximum probability. The yellow line is plotted at 45^0 i.e. it is a plot of the equation y=x.

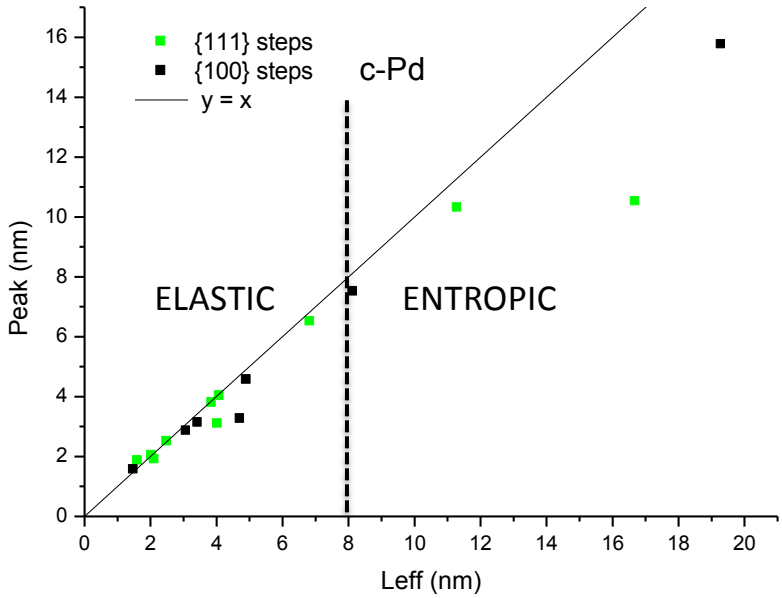

Figure 4:19: Position of the main peak with respect to the effective average terrace width of the terrace width distributions for the {111}- and {100}-type steps sides. The interaction between steps experiments a transition from elastic to entropic at 8 nm effective terrace width.

point in the line). The deviation of the peak from the crossing point indicates that the distribution has a non-symmetric shape. In this plot the deviation is observed for distributions with average terrace width bigger than 8nm on both sides of the crystal ({100} and {111}-type of steps). This tendency is better seen in figure 4.19 where the position of the peaks is plotted as a function of the effective average terrace width of the respective histograms. Taking into account the model of the step-step interaction presented in part 1 we have defined a critical value of the average terrace width ⟨L⟩=8nm, which divides a range of the smaller terraces where strong elastic interactions dominate, from the range of the wider terraces where entropic interactions prevail.

In conclusion, use of the curved crystal for the investigation of the microstructure of the vicinal surface of the Pd(111) has permitted us to probe the whole range of the miscut angles within +/-11^0 range. LEED patterns collected along the curved surface demonstrate gradual splitting of the spots which was attributed to the progressive variation of the average terrace widths with the miscut angle. Symmetry of the splitting with respect to the center of the crystal shows that the diffraction-sensitive microstructure of the vicinal surface is the same on the sides of {111}-type steps and {100}-type steps of the crystal. STM data revealed the presence of the di- and triatomic steps which do not form periodic superstructure and therefore do not contribute to the additional spots in the LEED pattern. Statistical analysis of the TWDs obtained from the STM images has demonstrated the existence of the “magic” terrace widths at the miscut angle of 2.7^0 on the side of the {100}-type steps and proved the transition from the elastic to entropic type of step-step interaction in the range of the terrace width of 8 nm.

4.2 Clean curved Ni(111)

The curved Ni(111) crystal was also polished in our laboratory. It has the same radius of curvature as curved Pd(111) (R=23.2 mm). Due to the dimensions of this crystal (11x11 mm^2) it has a total $\alpha=\pm14^0$ miscut angle which allows us to examine stepped surfaces at both sides of the crystal. This range of miscut angles includes vicinal surfaces from the (223) plane at $\alpha=+11.4^0$ (in the $[\bar{1}\bar{1}2]$ direction) with L=10.1 Å terrace width (4+2/3 atomic rows) and {100} type of steps, to the (553) plane at $\alpha=+12.3^0$ with L=9.36 Å terrace width (4+1/3 atomic rows) and steps of {111} type. As well as with the curved Pd(111), the preparation of the curved Ni(111) has been carried out following repeated sputtering and annealing cycles in the UHV chamber. Sputtering has been done initially with 2 KeV energy of Ar ions applied at 60 degrees with respect to the surface normal in the plane of incidence parallel to the surface steps. Then in the final cycles the energy has been reduced to 1 KeV, the pressure always was of $1\text{-}2x10^{-6}$ mbar. During the sputtering sample was moved for +/-2 mm horizontally and vertically keeping the direction of the surface normal intact so that the total fluence was distributed equally between five different positions. Each point was exposed for 3 minutes and the beam current measured in the grounding circuit was about 9-10 μA (2 keV; 4 μA for 1 keV). Afterwards, the sample was annealed using the e-beam heating with a voltage of 1 KV and emission current of 35-40 mA which results in the temperature of the sample of 600 ºC. The final pressure has been kept below 5.10^{-9} mbar. The sputtering-annealing cycles were repeated until the LEED showed clear splitting of the spots and low background which is an indication of the clean surface and regular step array.

The characterization of the vicinal surface has been done by means of the LEED with the beam energy of 92.2 eV. The sample has been moved laterally across the entire curved surface and the images have been acquired with Δz=0.5 mm step. Figures 4.20 (a-h) show some representative images. The hexagonal pattern characteristic of (111) terraces is clearly seen in all figures. Furthermore, those collected in the lateral parts of the crystal exhibit a splitting of the diffracted spots in the direction perpendicular to the steps. However, in contrast to the curved Pd(111), splitting of the spots in curved Ni(111) occurs differently for both sides of the crystal. When moving from the center along the $[11\bar{2}]$ direction, which is characterized by {111} type of steps (figures (e)-(h)), there is a smooth variation of the splitting of the spots. The clear separation between the spots is an indication of a regular step structure in the real space at this side of the crystal. On the contrary, the side of the crystal characterized by steps of the {100} type (figures (a)-(d)) shows a change in the diffraction conditions when moving with respect to the center half of the distance along the $[\bar{1}\bar{1}2]$ direction. Near the center, the splitting is similar to the one observed in the opposite side (figures (c), (d)) but in the lateral region (figures (a), (b)) there is a pronounced single spot accompanied by the separated but barely visible split spots.

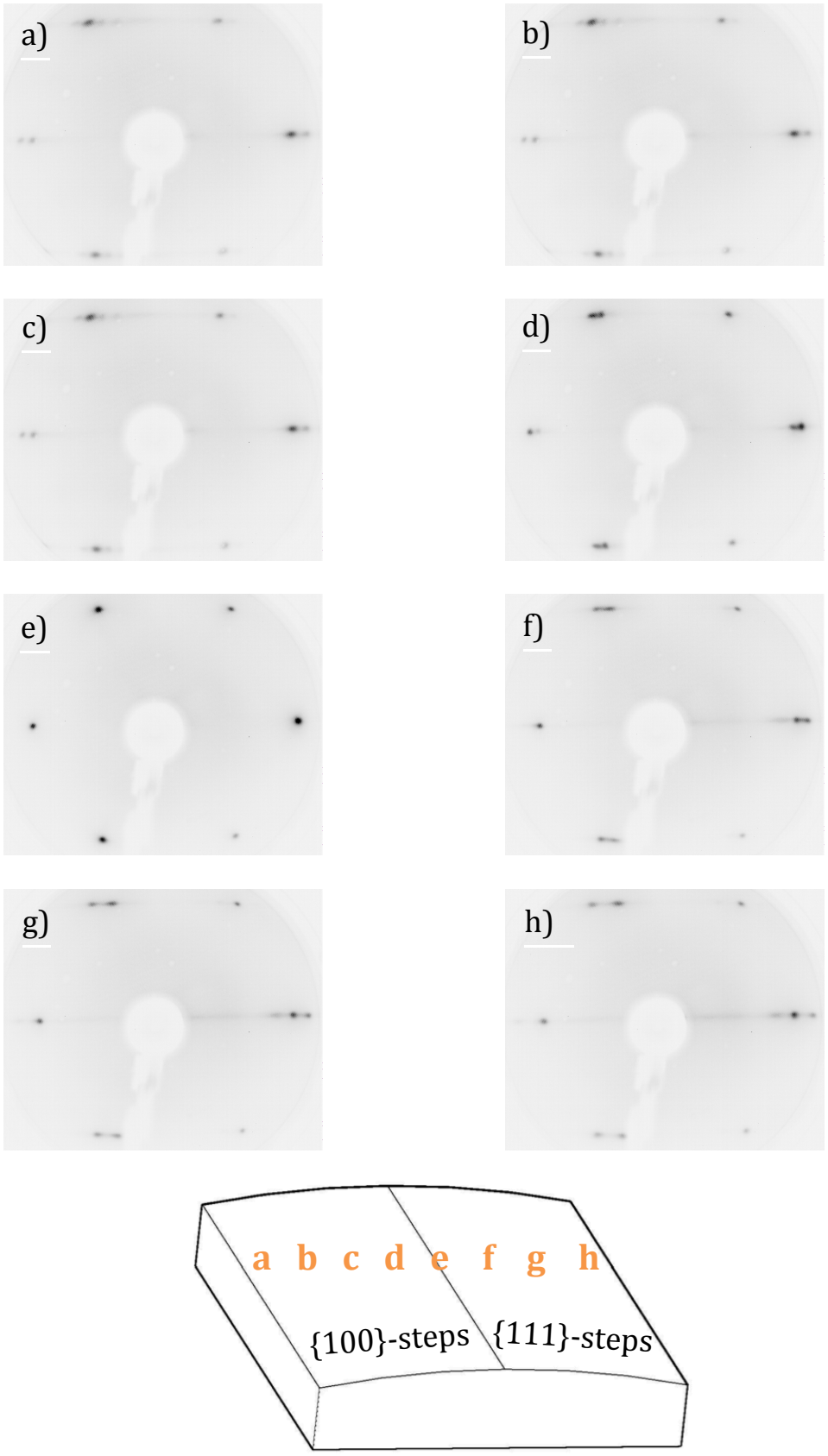

Figure 4.20: (a)-(h) Some representative LEED patterns of the curved Ni (111) surface (E=92.2 eV). The sequence of images from a to h is related to the movement from the {100}-type steps side to {111}-type steps side

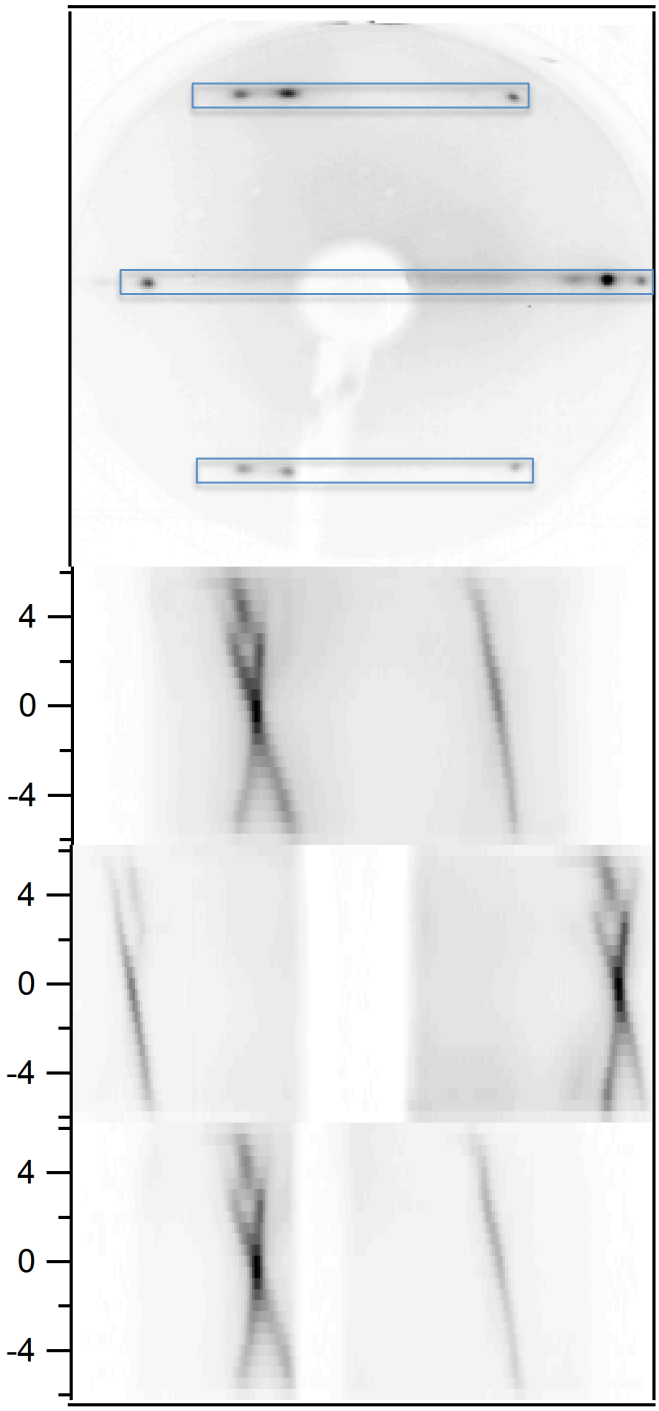

Figure 4.21: The top panel shows the LEED pattern taken at 3.5 mm from the center along the [11$\bar{2}$] direction ({111} type steps). Lower panel shows spatial variation of the splitting traced using the upper, intermediate and lower pair of spots of the whole pattern. Vertical axis indicates the position of the measurement in mm where 0 is the center of the crystal. Non vertical orientation of the crossed lines in the lower panels shows gradual change of the period of the hexagonal pattern due to the variation of the sample-screen distance during the scan.

This behavior is better visualized by means of the plots showing evolution of one pair of spots as a function of the position of the measurements. These plots shown in the lower panel of the figure 4.21 were built in the same way as for the curved Pd(111) crystal (see part 4.1). A stack of images was assembled out of the set of the LEED

patterns collected with 0.5 mm step so that a z-coordinate (in mm) indicates the position of the measurement with respect to the center of the crystal (z=0). Then a crosscut of this stack has been done along the three lines indicated in the upper panel of the figure 4.21.

The gradual variation of the spot splitting observed in the negative part of z coordinates of all three crosscuts confirms that part of {111}-type steps features a regular array of terraces whose average terrace width decreases with increasing miscut angle along the $[11\bar{2}]$ direction. Meanwhile, the smooth variation of the splitting is broken around z=3 mm (distance from the center in the $[\bar{1}\bar{1}2]$ direction).

In order to compare the LEED data to the results of STM characterization we have to perform a calibration using some known value of the terrace width. Taking into account the splitting of the spots for the side with {111} type of steps we can calculate the minimum terrace width (L_{min}) at $\alpha=14^0$ miscut angle which corresponds to the maximum splitting of the spots using equation (1):

$$\sin 14° = \frac{h}{d_{min}}$$

$$0.242 = \frac{a_0/\sqrt{3}}{d_{min}}$$

and then L_{min}=8.4 Å represents the minimum terrace width of this curved Ni(111) sample. The terrace width (d) is related to the splitting of the spots (Δ) such as $\Delta=2\pi/d$ [see part (2.2LEED)]. Therefore, we can calculate the terrace width where the periodic structure of the step lattice changes at the side of {100}-type steps. This occurs at the point where the splitting of the spots is half of the maximum splitting Δ_{max}, then:

$$\frac{\Delta_{max}}{\Delta_{cr}} = \frac{d_{cr}}{d_{min}}$$

$$d_{cr} = \frac{\Delta_{max} d_{min}}{\frac{1}{2}\Delta_{max}} = 2d_{min}$$

and d_{cr}=16.8 Å is a critical value of the average terrace width (approximately 1.7 nm). The disappearance of the linear splitting cannot be attributed to the drastic change of the width of distribution (lack of periodicity) because it would result in the broadening of the spot and this does not occur. In fact, the constructed LEED images show well defined spots and clear contrast between the intensity of the spots and the background. Thus, this change in the diffraction conditions of the stepped structure should be studied by STM because this technique provides more detailed information about the surface structure.

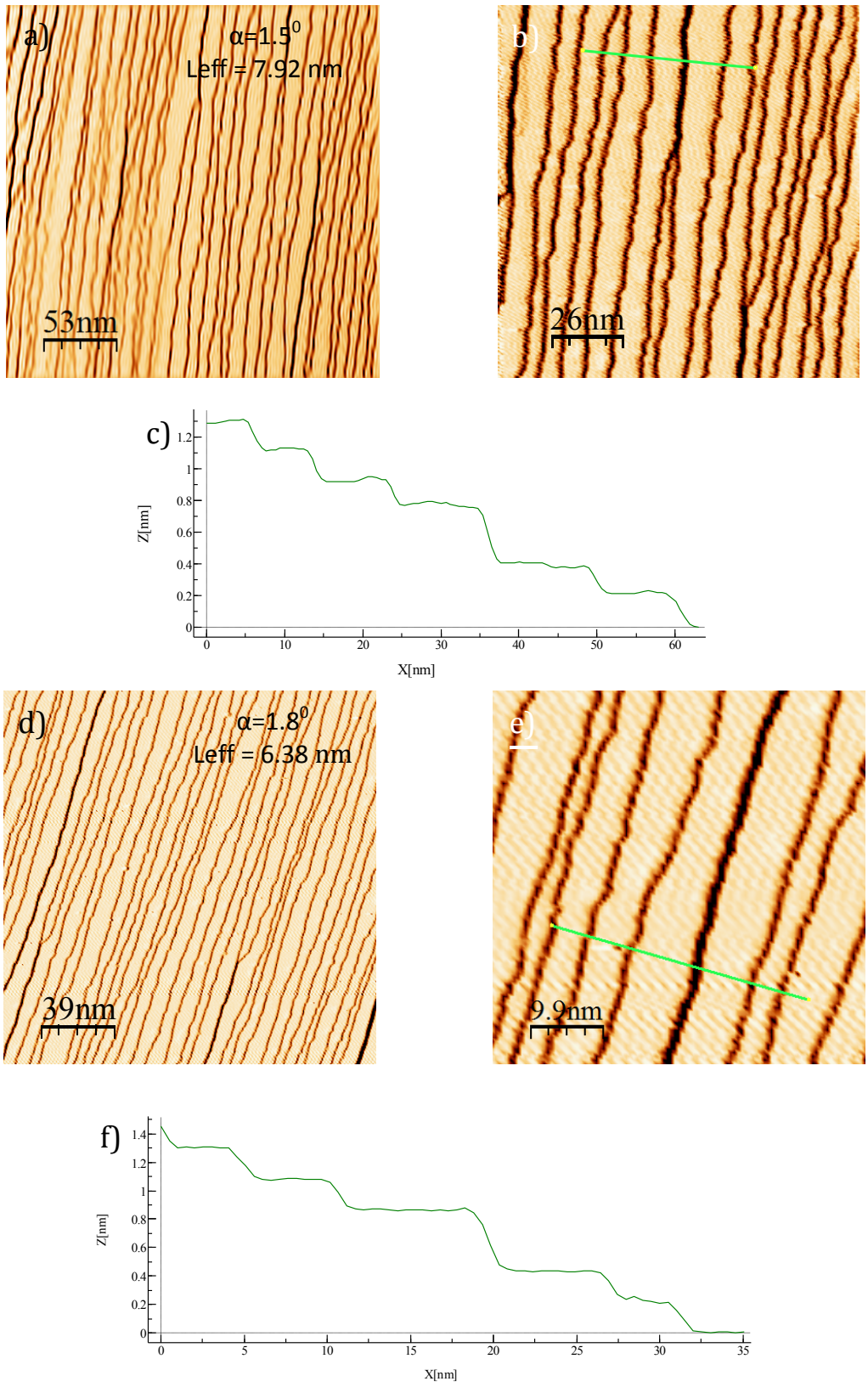

Figure 4.22: a) Derivative of the STM image (265x265nm^2) taken at α=1.5° for the curved Ni(111) at the side of {111}-type steps, b) zoom image of Figure (a), c) profile of the figure (b), d) derivative of the STM image (195x195nm^2) taken at α=1.8º, e) zoom of Figure (d), f) profile of the figure (e)

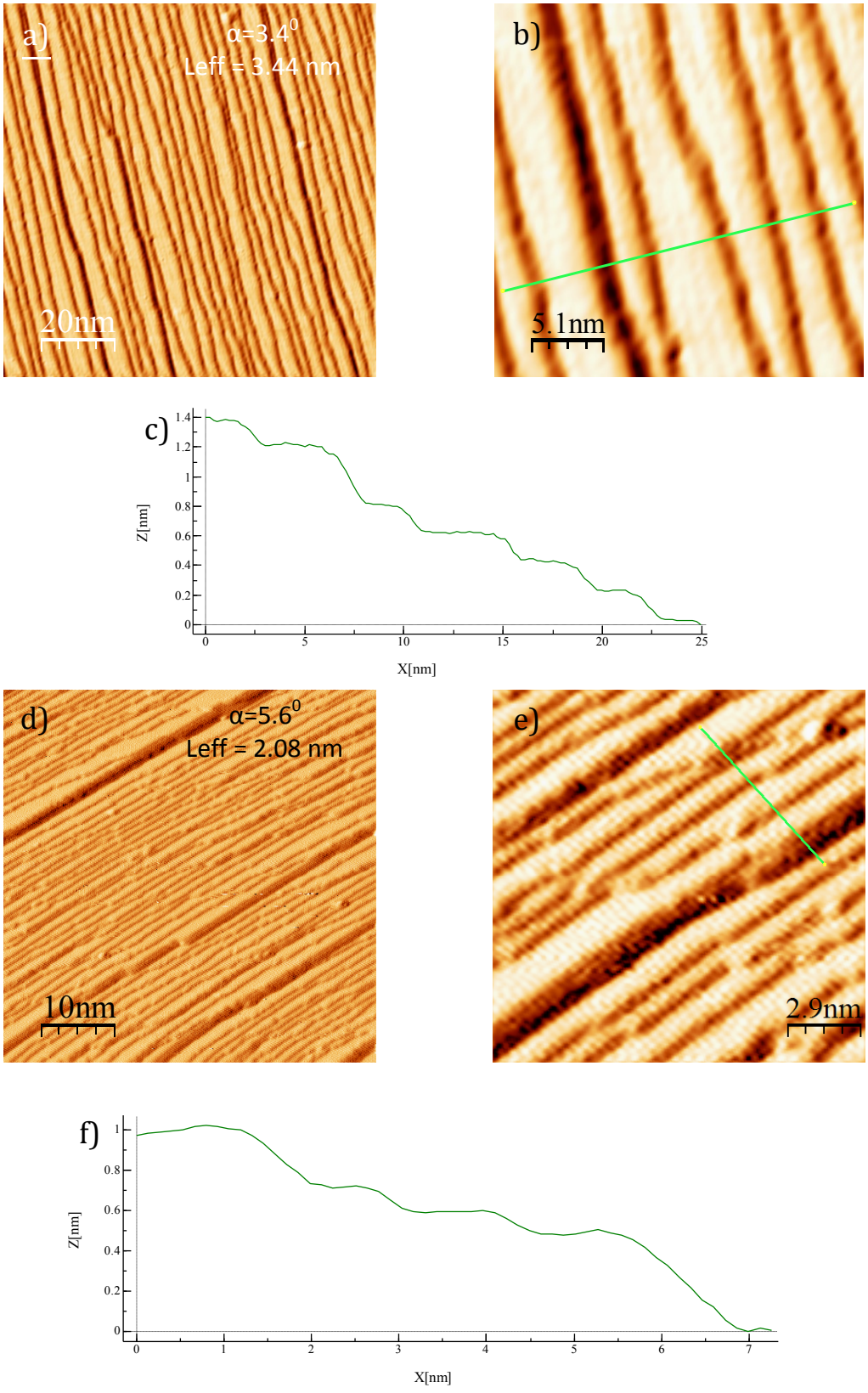

Figure 4.23: a) Derivative of the STM image (100x100nm^2) taken at α=3.4º for the curved Ni(111) at the side of {111}-type steps, b) zoom of the figure (a), c) profile of the figure (b), d) derivative of the STM image (50x50nm^2) taken at α=5.6º, e) zoom of the figure (d), f) profile of the figure (e)

First, we are going to focus on the side with {111}-type steps. According to the LEED patterns, splitting of the spots increases gradually with increasing miscut angle and no other features have been observed. Figures 4.22 and 4.23 show some representative STM images collected on this part of the crystal. Figure 4.22 demonstrates that in the range of small miscut angles, the vicinal surface is composed mainly by monoatomic steps and contains only minor amount of diatomic steps. Increasing of the miscut angle does not lead to the strong growth of the number of the diatomic steps but at the $\alpha = 5.6^0$ three atoms high steps were observed (see figure 4.23 d-f).

Histograms of the terrace width distribution were constructed for each zone from the statistical analysis of three side-by-side STM images, as described in chapter 4.1.

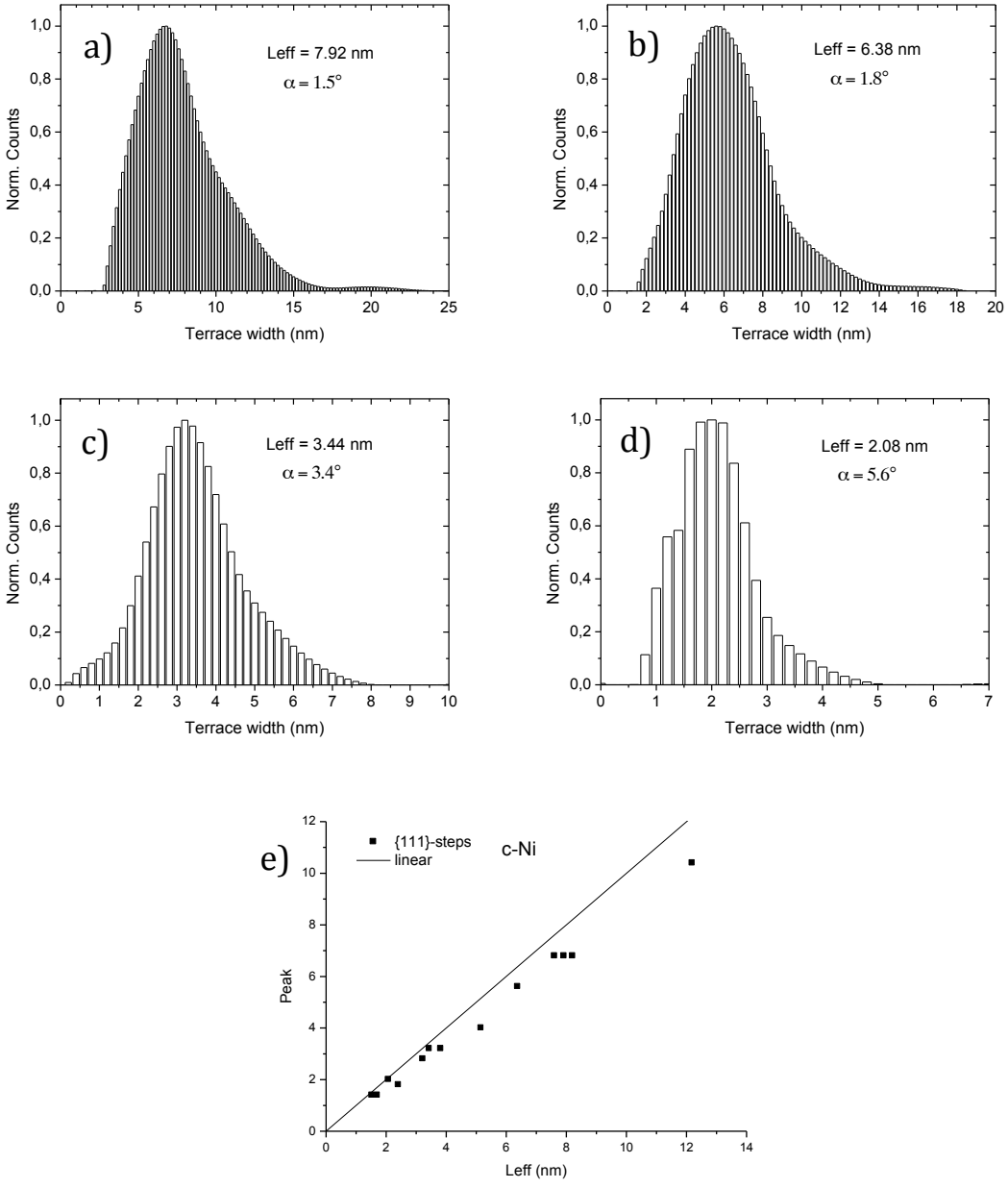

Figure 4.24: (a-d) Terrace width distributions of the regions corresponding to a) α=1.5º, b) α=1.8º, c) α=3.4º, d) α=5.6º. e) Position of the TWD peak as a function of the effective average terrace width for {111}-type steps.

Figure 4.24 shows four representative examples of the histograms which illustrate the general trend. In the range of bigger terraces the distribution is skewed and the peak is shifted towards the smaller values. When the average terrace width decreases the shape of the distribution gets more symmetric and the distribution itself becomes narrower (see figure 4.24 c). However in the range of small terraces distributions do not have Gaussian form (see figure 4.24 d) which can be explained by the presence of diatomic steps. The terraces next to these steps are wider (usually twice as wide as a regular terrace) therefore the respective distributions are the result of the convolution of two (or more) peaks which leads to the distortion of the original distribution shape.

Figure 4.24 (e) shows the positions of the TWD peaks as a function of the respective average terrace width L_{eff} (although no pronounced double-peak structure of the TWD was observed this designation is used for consistency of the analysis of both sides of the crystal). Again as in the case of the curved Pd(111), the maxima of the distributions coincide with the respective mean values in the range of narrow terraces and gradually departs of this direct proportionality when the terraces get wider, demonstrating progressive decreasing of the elastic step-step interaction.

Next we will focus on the side of the crystal with {100} type of the steps. As this side features two zones with different types of the LEED patterns, we will present the STM analysis for each zone separately.

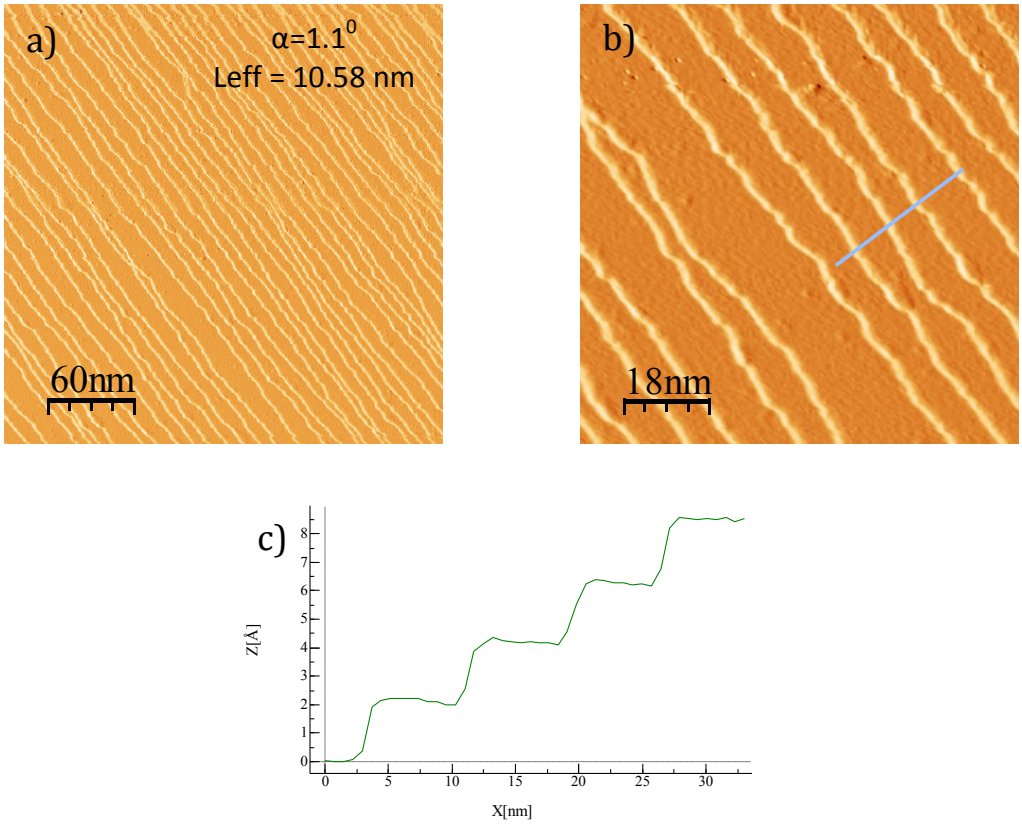

Figure 4.25: a) Derivative STM image (300x300nm^2) taken at α=1.1° for the curved Ni(111) and for 100}-type steps, b) zoom of the figure (a), c) profile of the figure (b)

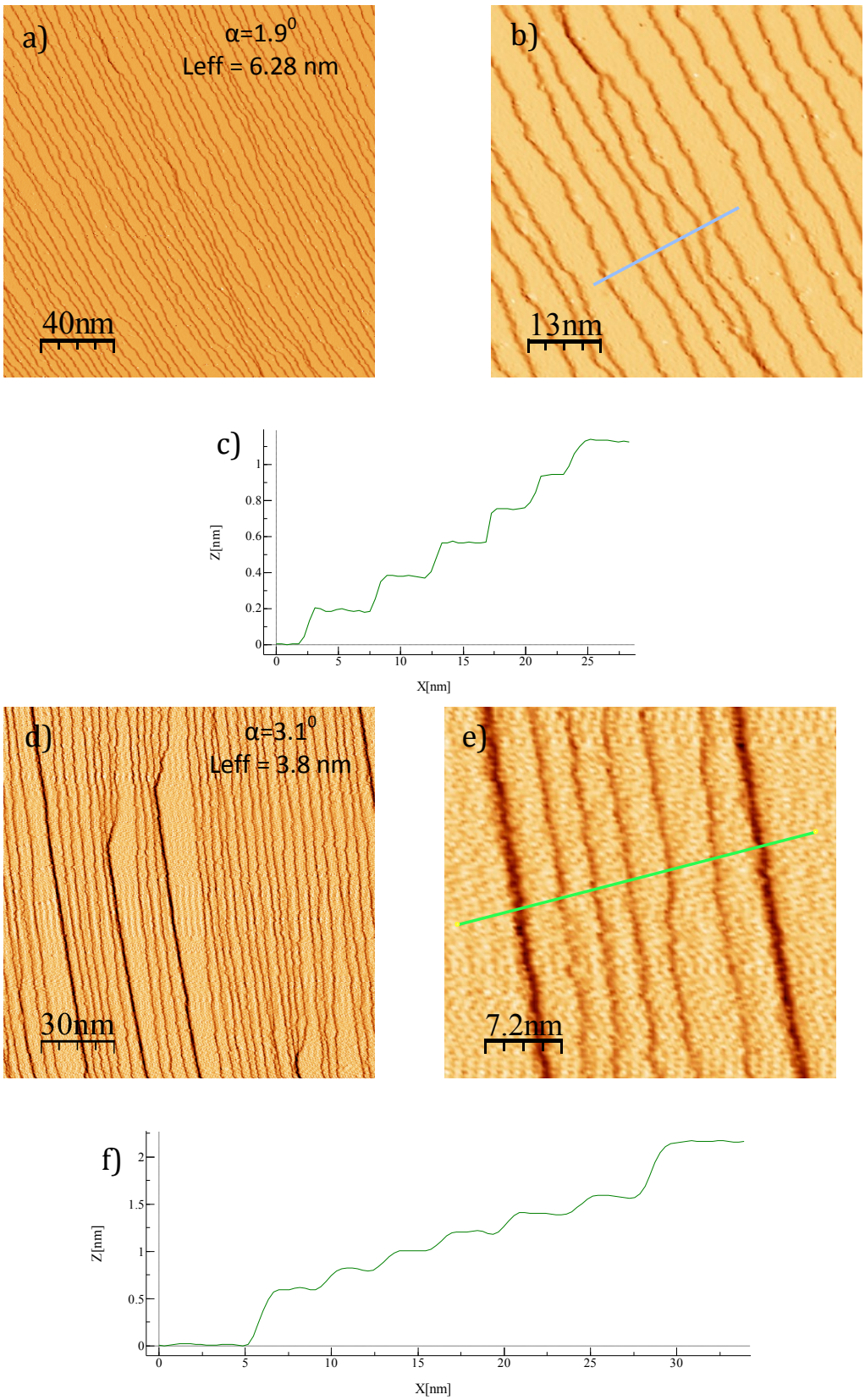

Figure 4.26: a) Derivative of the STM image (200x200nm^2) taken at α=1.9º for the curved Ni (111) and for {100}-type steps, b) zoom of the figure (a), c) profile of the figure (b), d) derivative of the STM image (150x150nm^2) taken at α=3.1º, e) zoom of the figure (d), f) profile of the figure (e)

Figures 4.25 and 4.26 show the STM images and the profiles collected at different miscut angles in the part of the crystal characterized by smooth splitting of the LEED spots. In this region the majority of the steps are monoatomic, however, in figure 4.26 (d) few di- and triatomic steps were observed. The terrace width distributions characteristic of these points are shown in figure 4.27 (a-c). As occurs in the side with {111}-type steps, central regions with wider terraces primarily characterized by monoatomic steps exhibit a predominant peak in the distributions (figure 4.27 a,b) where a small shift of the main peak with respect to the effective average terrace width is observed due to weak entropic step-step interactions.

The distribution shown in the figure 4.27 (c) has a pronounced peak due to monoatomic steps but also two minor peaks appear which are related to the presence of the di- and triatomic steps. Although the number of these steps is still insufficient to change the splitting of the LEED pattern (the average terrace width L_{eff}=3.8 nm is still bigger than the critical value L_{cr}=1.7 nm estimated from the LEED data) the corresponding peaks in the histogram are rather pronounced. Therefore we have calculated relative amounts of these steps and used equation (9) to calculate the effective average terrace width L_{eff}. Probabilities for various heights of the steps were calculated in the same way as we did for curved Pd(111) (see chapter 4.1). The distribution was fitted to the sum of three Gaussian peaks (shown in the figure 4.27 (c)

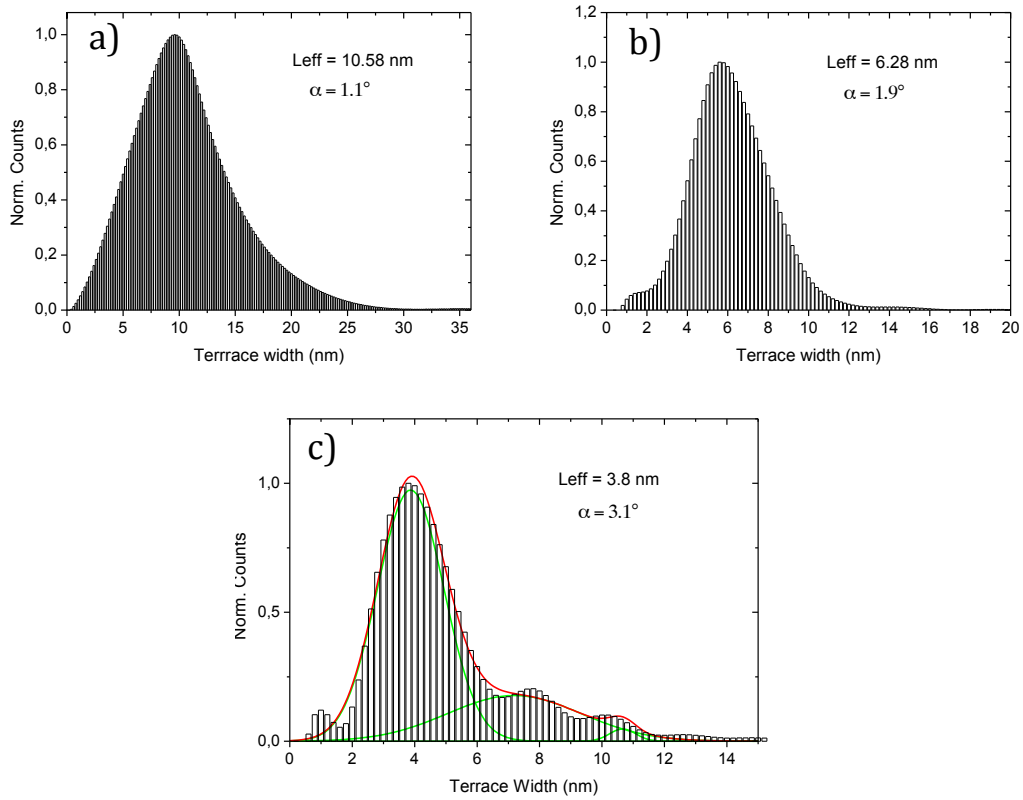

Figure 4.27: Terrace width distributions of the regions corresponding to the miscut angles of a) α=1.1º, b) α=1.9º, c) α=3.1º (fitting with Gaussian peaks (green line) and their sum (red line).

by the green lines) and their relative areas were taken as the estimates of probabilities. Relevant results of fitting are shown in the inset of the figure.

Now, we will analyze a local structure of the surface where the LEED pattern shows the predominant single spot with barely visible splitting of the spots instead of two split spots (part of the {100}-type steps with effective average terrace width smaller than 1.7 nm).

The STM images (figures 4.28 and 4.29) corresponding to this region and the respective profiles obtained from the zoom of the images (figures 4.28 (c) and 4.29 (c)) demonstrate abundancy of the diatomic steps, which is consistent with observed change of the LEED diffraction pattern, where the monoatomic step periodicity is broken. However, this observation must be supported with the quantitative information where the presence of double steps should be predominant. The distributions of the terrace width for these regions are shown in figure 4.30. Both distributions exhibit predominant peaks that correspond to the majority of the diatomic steps (their relative amount is 71.5 and 80% in the case of L_{eff} of 1.59 nm and

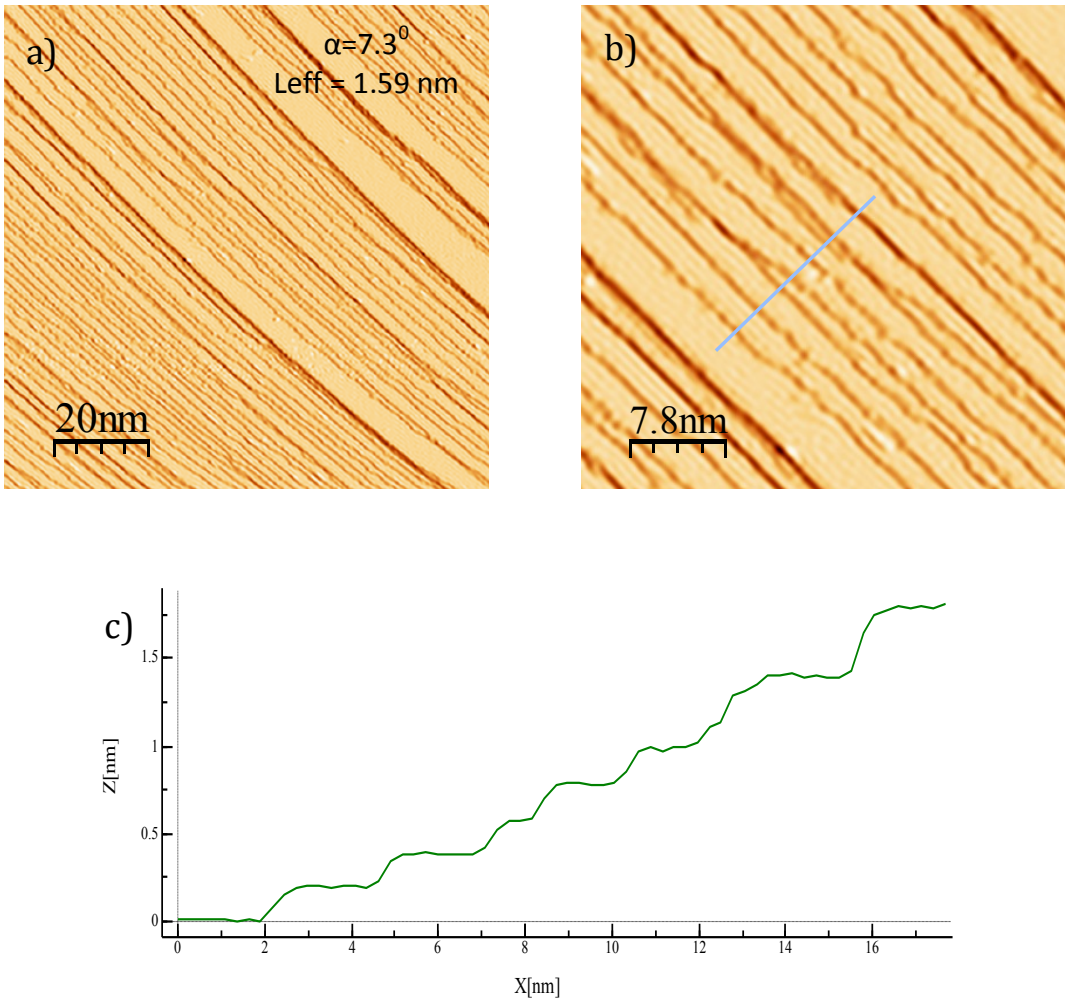

Figure 4.28: Derivative of the STM image (100x100nm2) taken at α=7.3° for the curved Ni(111) at the side of {100}-type steps ,b) Zoom of the figure (a), c) profile of the figure (b)

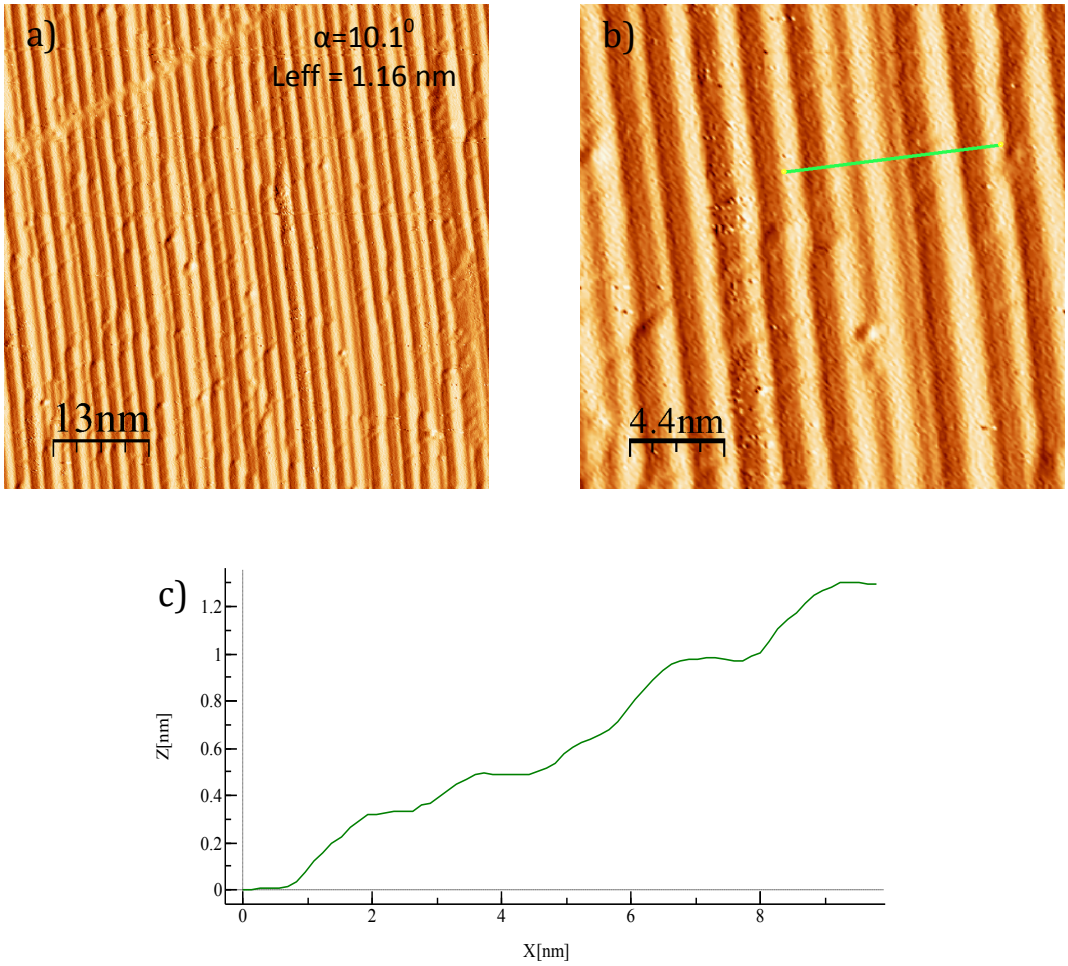

Figure 4.29: Derivative of the STM image (91x91nm^2) taken at α=10.1º for the curved Ni(111) at the side of {100}-type steps ,b) Zoom of the figure (a), c) profile of the figure (b)

1.16 nm respectively). Figure 4.30 (a) shows also a minor peak related to the presence of the triatomic steps but they make up only 15.9% of the total amount of steps. Finally, figure 4.31 illustrates a summary of the data obtained by means of the statistical treatment of all the STM images. As it has been previously done with the curved Pd(111), the plot has been built with all the histograms obtained across the curved Ni(111) surface. The upper part of the plot collects all the individual histograms

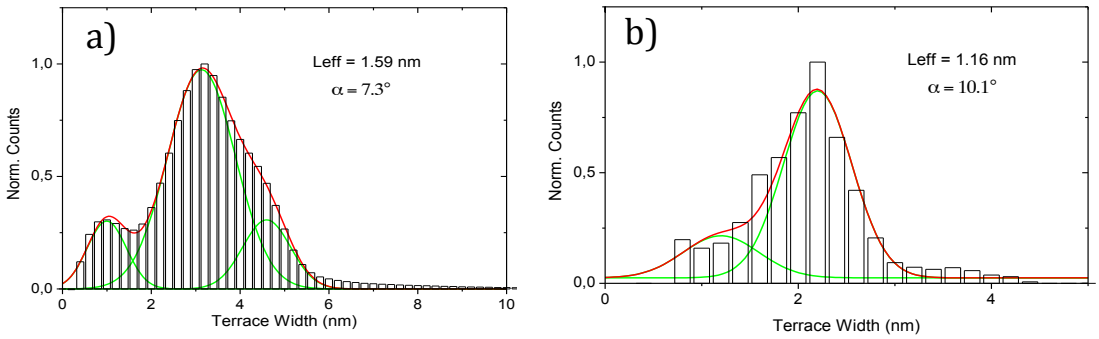

Figure 4.30: Terrace width distributions of the regions corresponding to the miscut angles a) α=7.3º (left) and b) α=10.1º (Right) at the side of the {100}-type steps

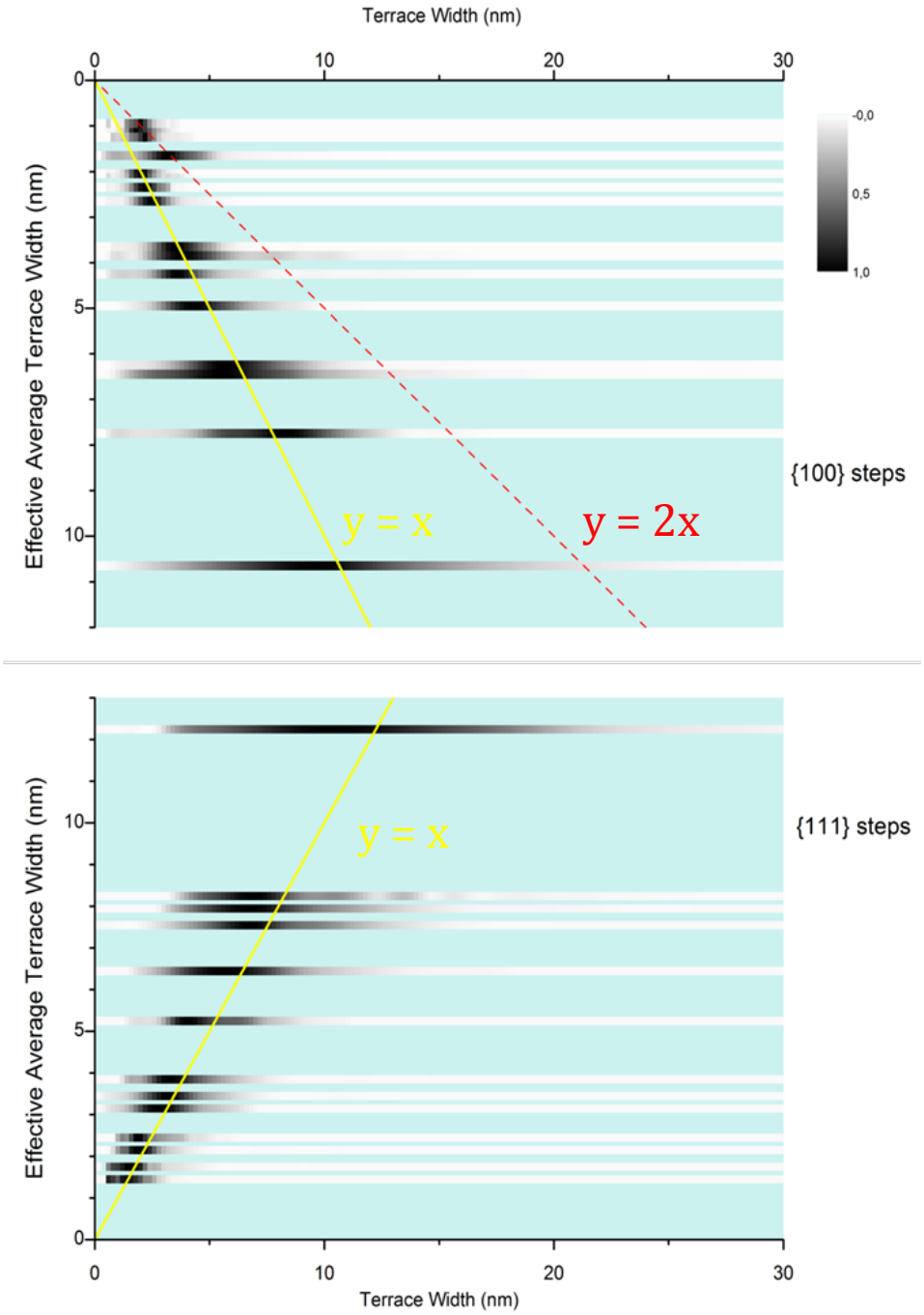

Figure 4.31: Image plot of the curved Ni(111) surface built with all the probability histograms at different mean terrace values <L>. Histograms are individually normalized to the maximum probability. The yellow line is plotted at 45^0 i.e. it is a plot of the equation y=x and the red line y=2x

obtained for the side of the {100}-type and the lower part for the {111}-type steps. Y-coordinate of the histogram shows the effective average terrace width. The yellow line is plotted at 45^0 (y=x plot) and therefore it crosses each histogram in the point whose X-coordinate is equal to the effective average terrace width of the histogram. For the histograms that represent symmetric distributions the crossing point should coincide

with the position of the maximum of the histogram (the darkest point in the line). The deviation of the peak from the crossing point indicates that the distribution has a non-symmetric shape. In this plot the deviation is observed for distributions with average terrace width bigger than 6nm on both sides of the crystal ({100} and {111}-type of steps). This tendency is seen better in figure 4.32 where the position of the peaks are plotted as a function of the effective average terrace width of the respective histograms. The critical value of the average terrace width ⟨Lcr⟩ which divides a range of the smaller terraces where dominate strong elastic interactions from the range of the wider terraces where prevail entropic interactions was found to be of 6 nm which is smaller than ⟨Lcr⟩= 8 nm, observed in the curved Pd(111) (see chapter 4.1).

A red line (a plot of equation y=2x) crosses each histogram in the point whose X-coordinate is double of the effective average terrace width of the histogram. It is clearly seen in the figure 4.31 that the histograms with effective average terrace width smaller than 2 nm has peaks at the position twice as L_{eff} which means that respective zones contain mainly diatomic steps. This conclusion correlates with the change of the LEED diffraction pattern observed on the same side of the crystal in the range of the average terrace width smaller than 1.7 nm.

In conclusion, use of the curved crystal for the investigation of the microstructure of the vicinal surface of the Ni(111) has permitted us to probe the whole range of the miscut angles within +/-14^0 range. LEED patterns collected along the curved surface demonstrate gradual splitting of the spots on the side of the {111}-type steps which was attributed to the progressive variation of the average terrace widths with the miscut angle. Lack of symmetry of the splitting with respect to the center of the crystal shows that the diffraction-sensitive microstructure of the vicinal surface is not the

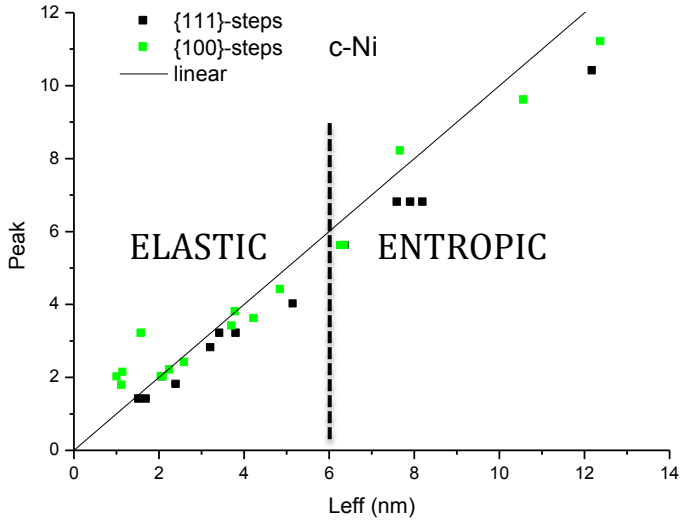

Figure 4.32: Position of the TWD peak as a function of the respective effective average terrace width for the side of {100}-type steps. The interaction between steps experiments a transition from elastic to entropic at 6 nm effective terrace width.

same for {111}-type steps and {100}-type steps. STM data revealed the presence of the di- and triatomic steps which do not form periodic superstructures, and therefore do not contribute to the additional spots in the LEED pattern on the side of the {111}-type steps. In contrast the diatomic steps predominate on the side of the {100}-type steps in the range of the effective average terrace width smaller than 1.7 nm. It leads to the increasing of the terrace width and therefore decreasing of the respective spot separation $\Delta=2\pi/d$ [see part (2.2LEED)]. As a consequence, the change of the mutual arrangement of the rods in the reciprocal space from the situation exemplified with a rod (10) to the situation of the rod $(\bar{1}0)$ shown in the figure 2.8 prevents the spot splitting in the respective LEED patterns.

This latter finding about stability of the {100}-type diatomic steps is worth an additional consideration to elucidate the possible reasons of this effect. According to the general theory presented in the part 2.1 it can be originated from the local minimum of the surface energy of the respective vicinal plane, strong step-step interaction or the influence of the contamination. Equilibrium crystal shape of pure Ni [25] does not contain any stable facets between (111) and (100) planes in the $[\bar{1}\bar{1}2]$ direction (see also figure 2.2, part 2.1). Furthermore, various authors have reported single atomic steps in the flat vicinal crystals of Ni (977) [60-62] and (511) [63] which rules out the energetic favorability of step doubling of the pure Ni.

On the other hand extensive research was aimed to study step doubling and other morphological transformations of vicinal surfaces due to the adsorption of various substances. For instance, exposure of pure Ni to the carburizing atmosphere was found to change the crystal from polyhedron with sharp edges to the rounded shape and provokes formation of steps. It was ascribed to the lowering of the anisotropy of the surface energy due to the adsorption of carbon [25]. Reversible step doubling was observed in Pt(997) [64], Rh(332) [65] and Ni(977) [60] exposed to submonolayer doses of oxygen. In this latter case the width of (111) terraces was of 1.65 nm, which is consistent with a range of step doubling found in this work. The driving force of the step doubling was thought to be a preferential adsorption of oxygen on the four-fold hollow sites of the {100} microfacet [60]. Amount of oxygen sufficient to complete the transformation of single atomic steps to diatomic steps is very low (less than 2% of adsorbate monolayer coverage), therefore it was concluded that even the oxygen concentration below the detection limit can provoke the step doubling of the vicinal Ni surfaces [66].

5. Growth of cobalt

For Co growth experiments, the preparation of the curved surfaces has been carried out following the protocol of the sputtering-annealing cycles described in sections 4.1 and 4.2 for Pd(111) and Ni(111), respectively. Cobalt has been deposited from the electron-beam heated rod with an evaporation rate of 0.15 ML/min. The pressure during the evaporation was maintained below $2x10^{-9}$ mbar. The heating power was equal to 9 W (1000 V x 9 mA of emission current) and samples were kept at room temperature. The stability of the evaporation rate was monitored using a quartz microbalance moved to the position of the sample prior to each preparation. The calibration of the absolute value of the evaporation rate has been done using the STM. For this purpose, a submonolayer amount of Co was evaporated on curved Pd(111) crystal and the effective coverage was calculated as a ratio of the Co/Pd surface areas within few large terraces.

Since the size of the substrate crystals is relatively big, initially we have verified that the entire surface of the sample is equally covered with cobalt. Effective coverage was calculated by means of the STM measurements (determination of ratio of the Co/Pd surface areas) in the three different positions separated by 3 mm approximately across the surface curvature (see figure 5.1). Results of measurements are summarized in the table 5.1

Position	Area (nm x nm)	Coverage d (ML)	Δd/d(%)
1	120 x 120	0.085	14.9
2	120 x 120	0.072	2.7
3	120 x 120	0.065	12.2

Table 5.1 Test of the uniformity of the Co evaporation

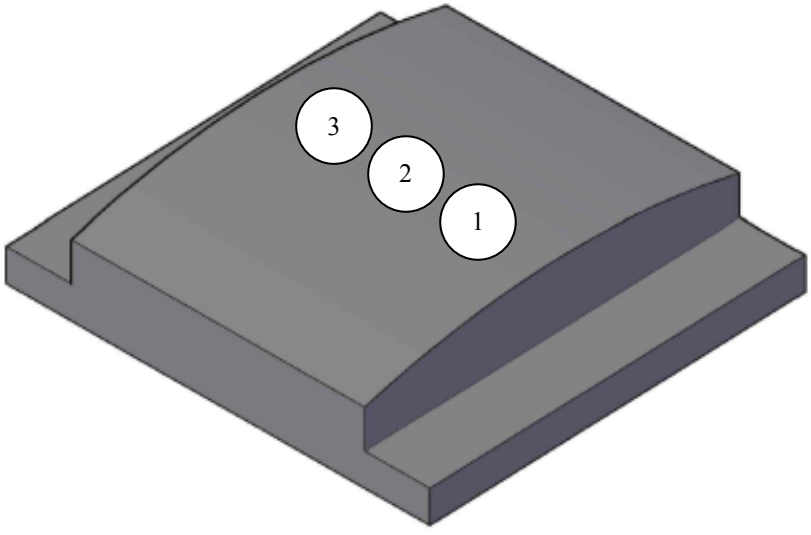

Figure 5.1: Positions of the measurements of the cobalt coverage on curved Pd(111) crystal

As it can be seen from the table the coverage in the three zones is similar. The mean value is 0.074ML and the deviation is lower than 15% with respect to the average. Since evaporation of cobalt is isotropic in the plane of the substrate this result allows us to confirm that Co is uniformly deposited on the entire surface of the crystals and therefore we are able to study the cobalt growth as a function of the curvature of the crystal.

5.1 Growth of Co on curved Pd(111)

We have studied seven different Co coverages on curved Pd(111) surface grown with the same evaporation rate of 0.15 ML/min. For the first five preparations the mean coverage has been cross-checked by means of the STM measurements performed in three different large terraces (see table 5.2) and for the rest we have extrapolated the time used for the evaporation of cobalt to estimate the coverage.

In figure 5.2 the topography data of the Co overlayers correspond to the central part of the crystal (the miscut angle $\alpha=0^0$) as a function of the effective Co coverage. Since the surface in this region is composed of terraces wider than 100 nm it is equivalent to the Co growth on flat Pd(111) crystal. Then the influence of the terrace width is studied for each value of the effective Co coverage (the data are presented as a function of the miscut angle).

For the lowest studied effective coverage of 0.075ML, Co grows on the wide terraces as single-layer islands and in some islands the formation of the second layer is observed (see figure 5.2). The ratio of the area covered by 1ML-high Co layer to the area covered by 2ML-high Co layer is 9/1 (90% of the total area covered by Co has a height of 1ML). The formation of the third monolayer has not been observed in this sample. Figure 5.2 (a) shows the STM images of two terraces separated by one atomic step. Figure 5.2 (b) is a zoom within one of the terraces, where the shape of the islands is clearly visible. The first and second layer of the islands can be seen in the profile of the figure 5.2 (c). The histogram of figure 5.2 (d) represents the area of the islands at the lower terrace of the figure 5.2 (a). The peak of the histogram shows that the most probable value of the island area is 18 nm^2.

Preparation	Coverage (ML)	Relative error (%)
1	0.075	14
2	0.25	17
3	0.38	16
4	0.72	1
5	1.0	1
6	1.8	-
7	3.0	-

Table 5.2 Summary of the effective Co coverages for the Co/c-Pd(111) samples

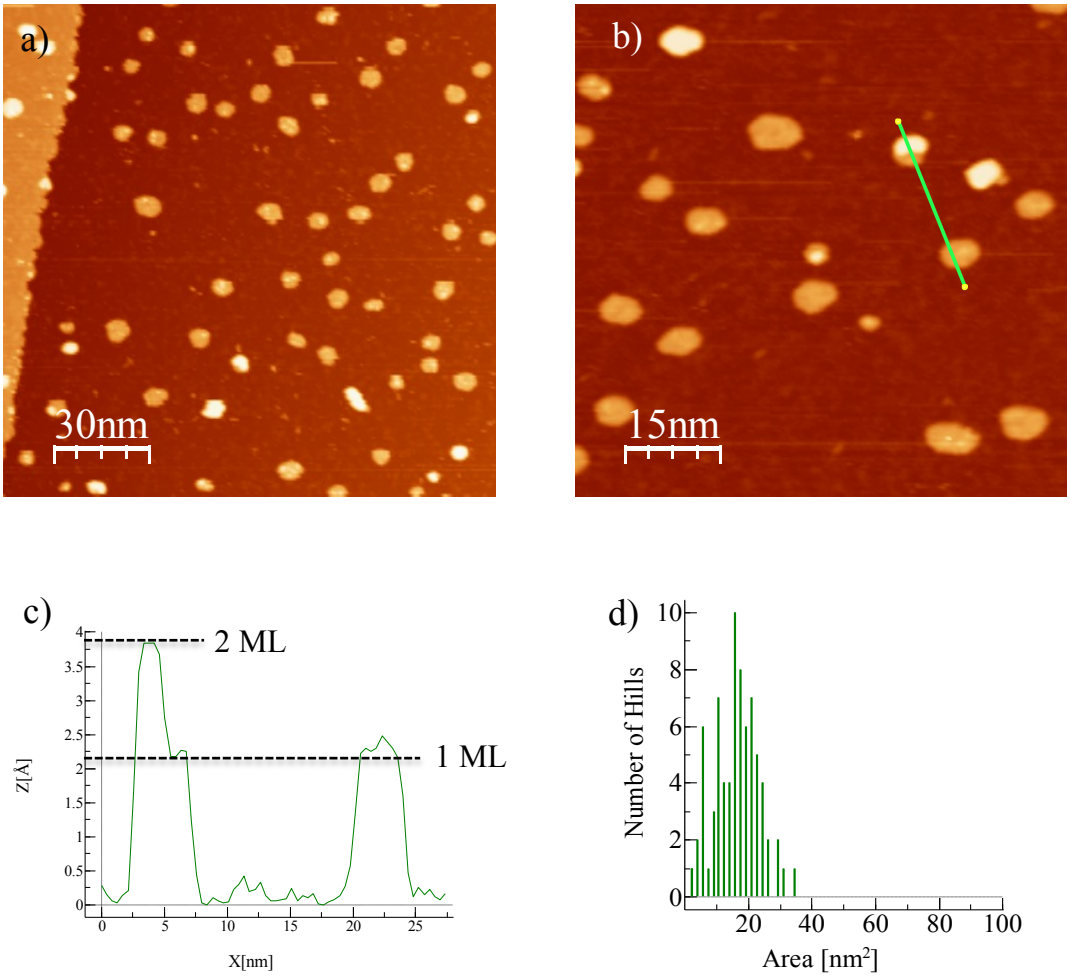

Figure 5.2: a) STM topography image acquired for the Co/c-Pd(111) sample at the miscut angle $\alpha = 0^0$. The effective Co coverage is 0.075ML, b) zoom of the image (a), c) profile for the figure (b), d) histogram of the area of Co islands measured in the lower terrace shown in panel (a)

Increasing the effective Co coverage leads to the rapid growth of the average island area and the progressive completion of the second layer. Only data for 0.25ML sample deviate from the general linear relationship between the proportion of the second layer in the total area covered by Co and the effective Co coverage (see figure 5.9). Transition from 1ML high islands to 2 ML high islands is completed for the sample with 1ML of the effective Co coverage which has almost no 1ML high islands. At the same time development of the third monolayer was observed in the samples with effective coverage of 0.72ML and higher. Further increasing of the coverage leads to the coalescence of the islands. For 1.8ML sample some separated islands are still present in the large terraces and in the 3ML sample completely percolated Co film was observed. Figures 5.3-5.7 shows the evolution of the shape of the islands and figures 5.9 (a)-(d) summarize the quantitative information obtained by means of statistical analysis of the STM images.

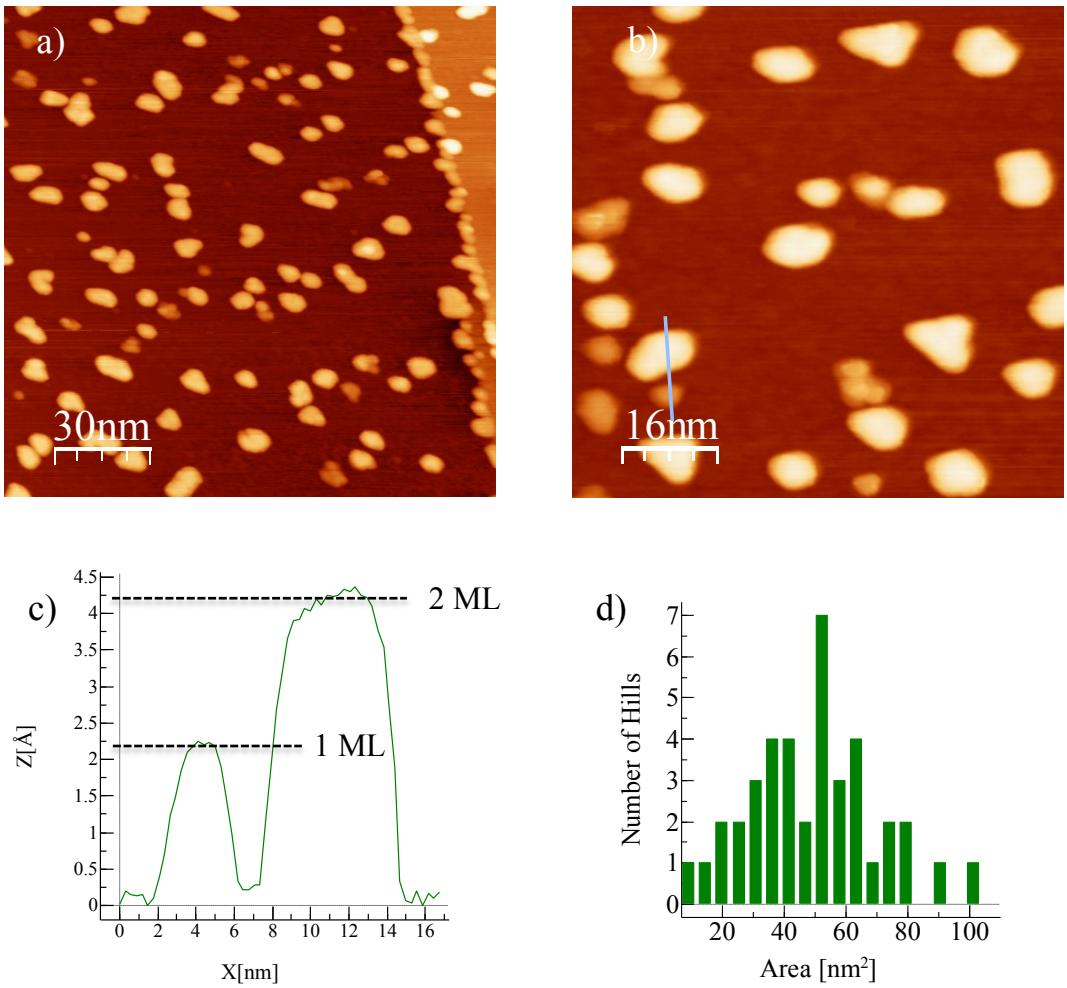

Figure 5.3: a) STM topography image acquired for the Co/c-Pd(111) sample at the miscut angle $\alpha = 0^0$. The effective Co coverage is 0.25ML, b) zoom of the image (a), c) profile for the figure (b), d) histogram of the area of Co islands measured in the lower terrace shown in panel (a)

The present data complement results of previous investigations of the Co/Pd(111) system. In recent work [23, 67] the growth mode has been studied at various temperatures by means of the STM and the authors concluded that in the submonolayer regime at room temperature Co forms only 2ML-high islands on the flat Pd(111) surface. At 210 K an incomplete second layer was observed, and at 500-550 K the islands were found to have single layer only. However the lowest studied effective coverage was of 0.4ML, therefore these results probably do not contradict our findings but show the difference in the calibration. According to figure 5.9 (a) 1ML high islands disappear in the sample with effective coverage of 1ML so the underestimation of the coverage by 0.5ML in Refs. [23, 67] may explain the discrepancy. On the other hand the evaporation rate in these works (0.4 ML/min) is more than twice as high as our evaporation rate (0.15 ML/min) therefore the difference in the results can be originated from the kinetics of the growth process. Relatively large lattice mismatch of 9% between the fcc phases of Co and Pd raises a question of the feasibility of the pseudomorphic growth in this system. Older results of the low energy ion scattering (LEIS), low energy electron diffraction (LEED), X-ray

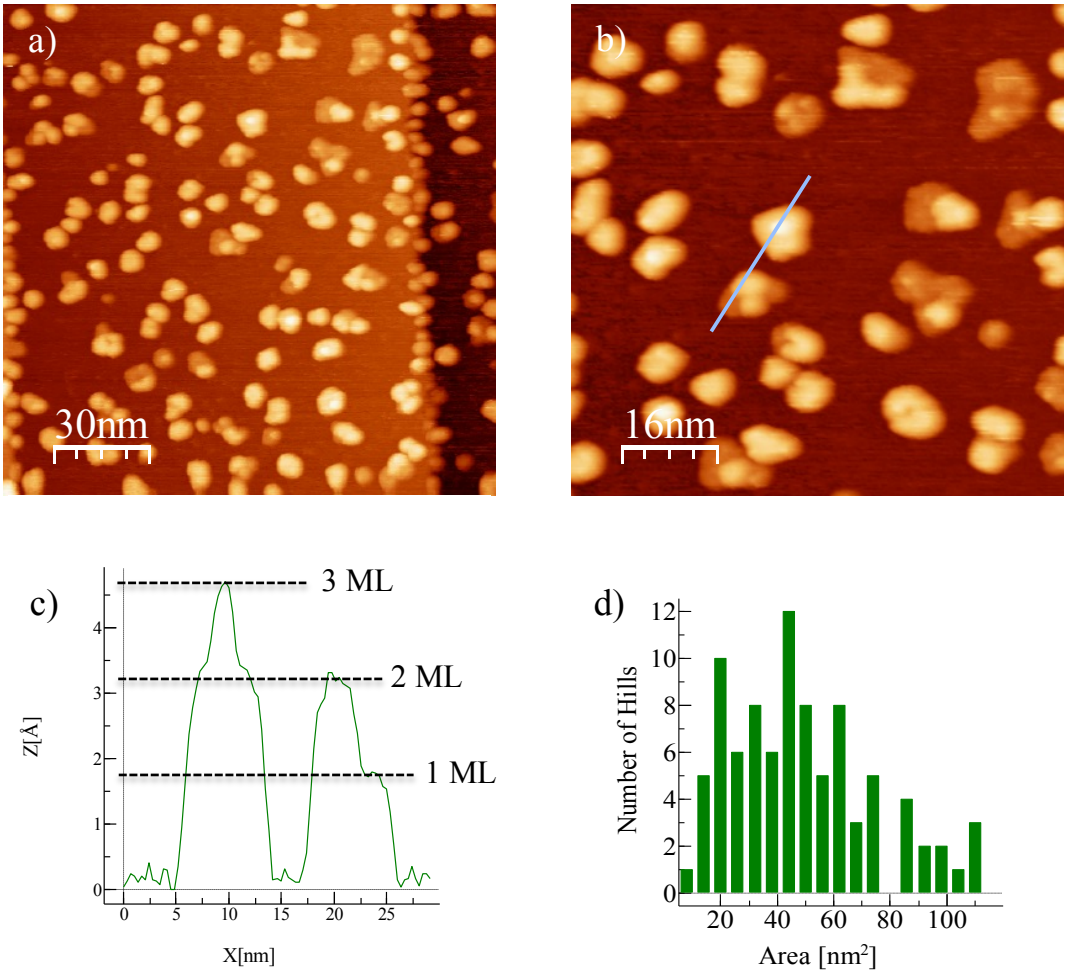

Figure 5.4: a) STM topography image acquired for the Co/c-Pd(111) sample at the miscut angle $\alpha = 0^0$. The effective Co coverage is 0.38ML, b) zoom of the image (a), c) profile for the figure (b), d) histogram of the area of Co islands measured in the lower terrace shown in panel (a)

photoelectron spectroscopy (XPS) and X-ray photoelectron diffraction (XPD) show that the cobalt islands have a tetragonally distorted fcc structure and that the Co film grows pseudomorphically for the first 1–2 atomic layers [68, 69]. However more recent STM data [23, 67, 70] demonstrate formation of the hexagonal dislocation networks within the islands which was interpreted as a non-pseudomorphic growth and relaxation of the stress via formation of the fcc and hcp domains. This conclusion is supported by the LEED patterns characteristic of the moiré reconstruction which were reported in the papers [23, 67, 71, 72]. Nevertheless Kim et al. found evidence that Co grows pseudomorphically on palladium (111) in a layer-by-layer mode and the surface morphology at submonolayer coverage is characterized by small monolayer high islands [73, 74].

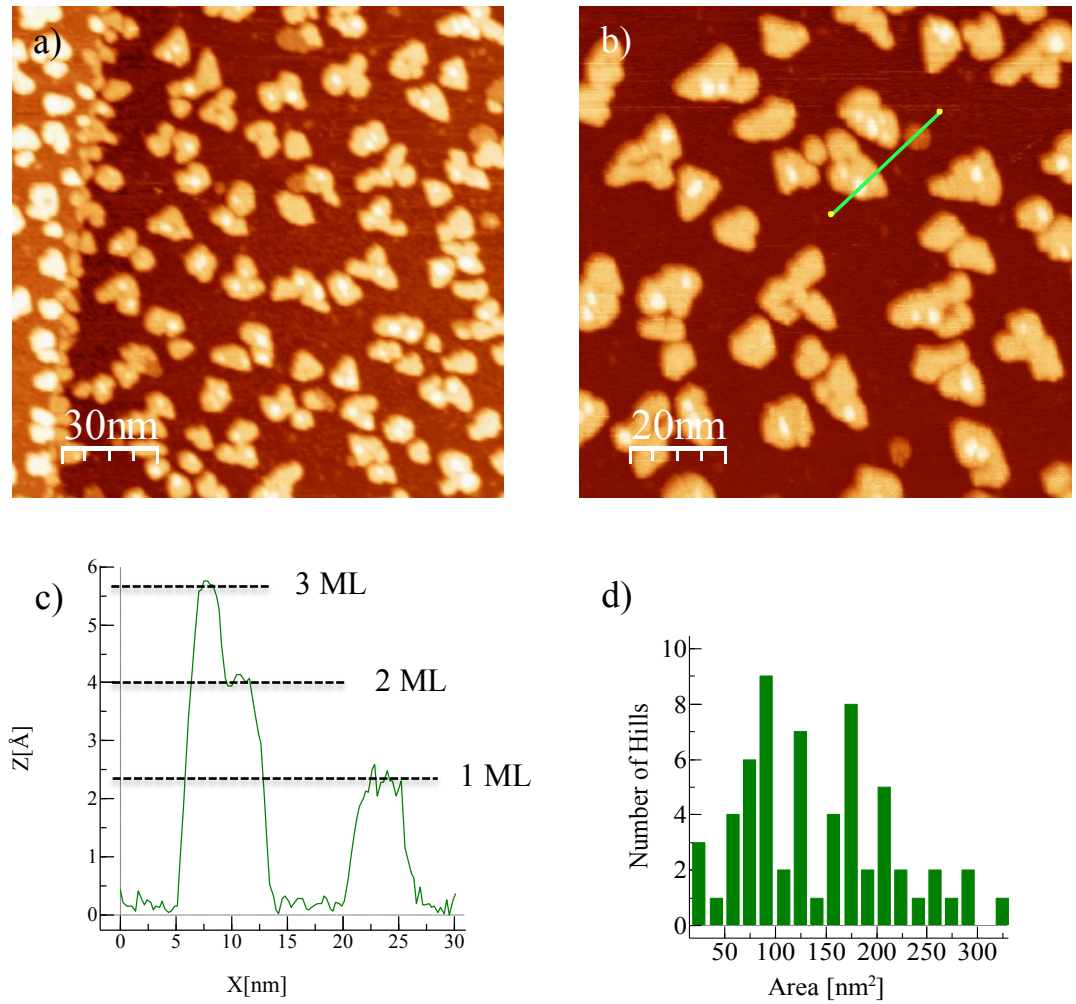

Figure 5.5: a) STM topography image acquired for the Co/c-Pd(111) sample at the miscut angle $\alpha=0^0$. The effective Co coverage is 0.72ML, b) zoom of the image (a), c) profile for the figure (b), d) histogram of the area of Co islands measured in the lower terrace shown in panel (a)

Our LEED measurements have not revealed any additional spots except the common pattern characteristic of (111) atomic terraces. However, STM images shown in figure 5.6 shows a pattern of protrusions in the topmost layer of the islands very similar to the one observed in the papers [23, 67, 70] and identified as a red of dislocation lines separating the fcc and hcp domains. Since the area of the islands decreases rapidly with decreasing of the effective Co coverage and the islands become single-layered it is reasonable to suppose that the islands break into structural domains only when they reach some critical average size (which according to our STM data is characteristic of the effective coverages of 0.72-1.0ML). Meanwhile for lower effective coverages Co islands grow pseudomorphically.

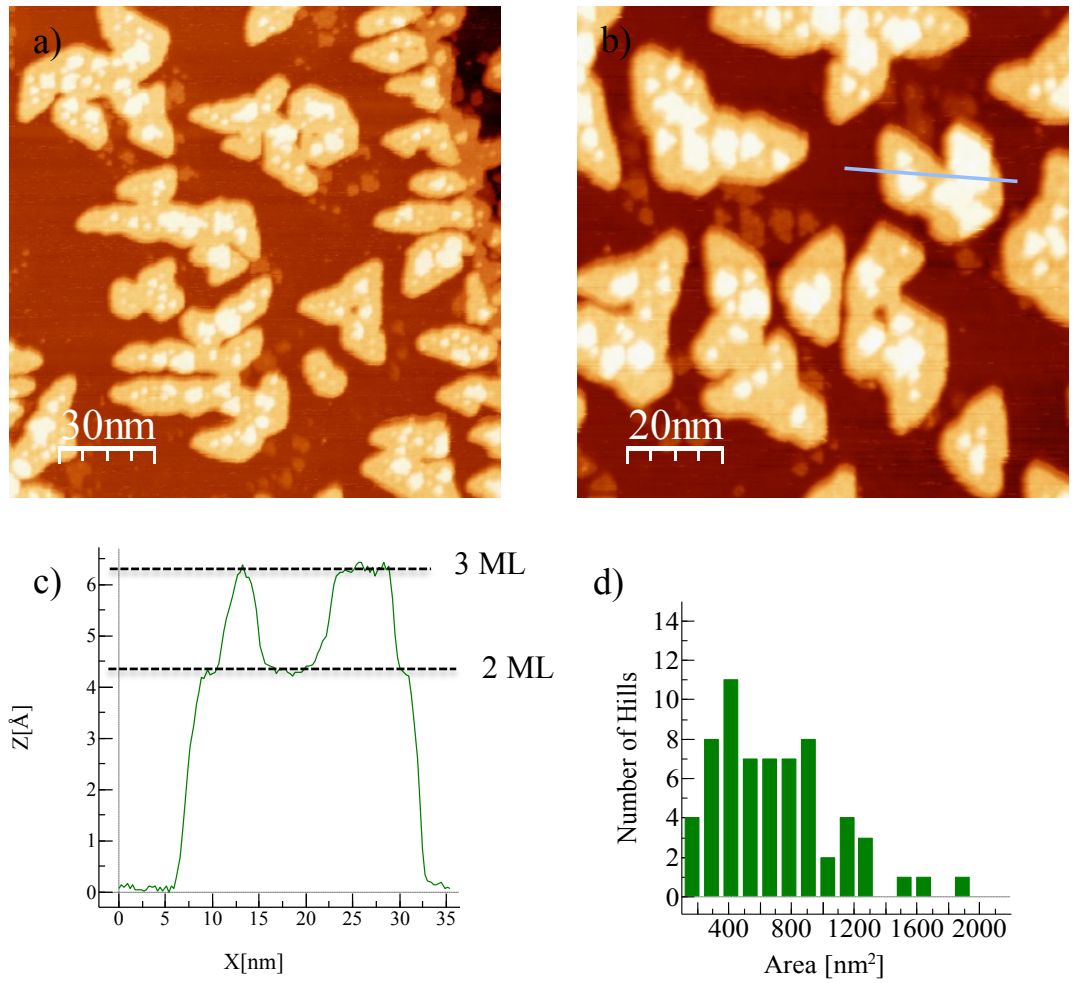

Figure 5.6: a) STM topography image acquired for the Co/c-Pd(111) sample at the miscut angle $\alpha=0^0$. The effective Co coverage is 1.0ML, b) zoom of the image (a), c) profile for the figure (b), d) histogram of the area of Co islands measured in the lower terrace shown in panel (a)

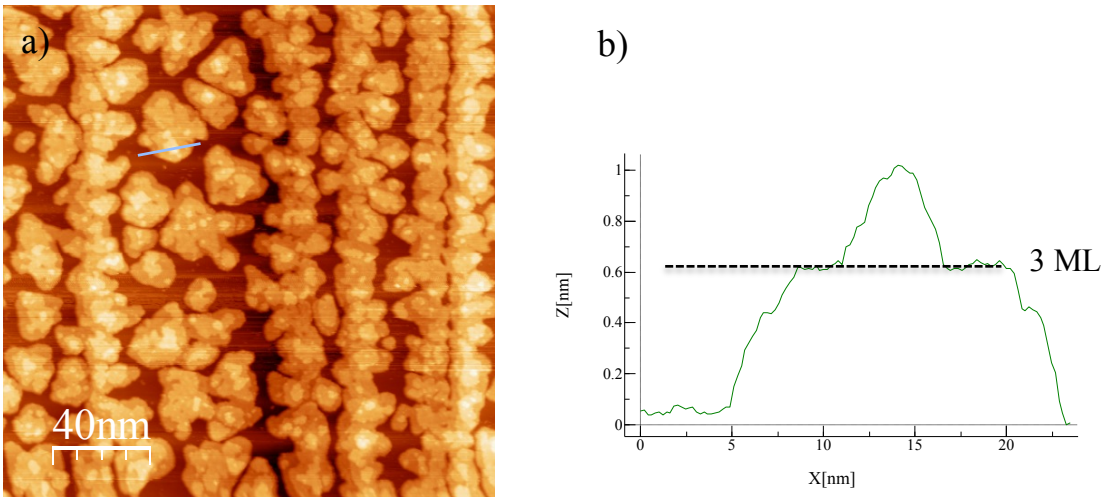

Figure 5.7: a) STM image for a cobalt effective coverage of 1.8ML, b) profile of panel (a)

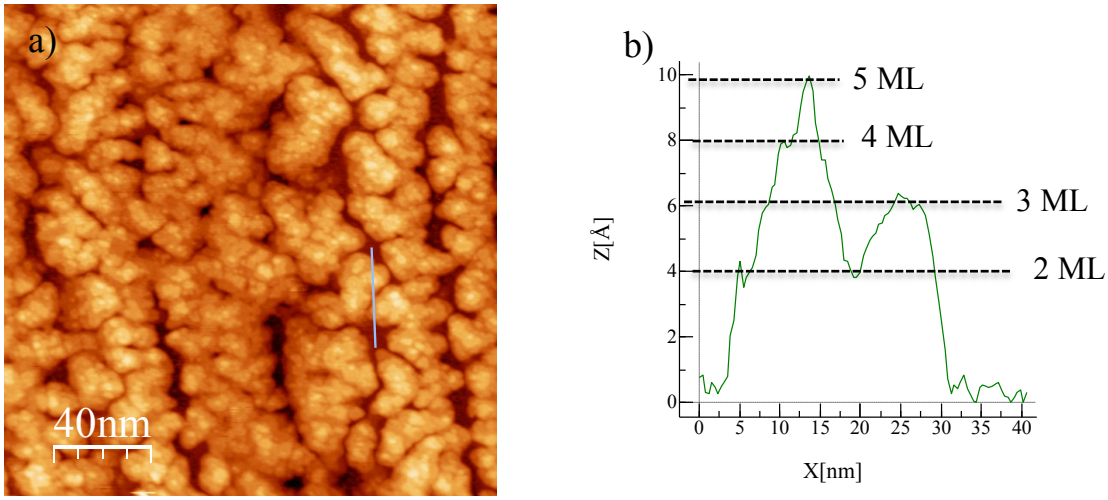

Figure 5.8: a) STM image for a cobalt effective coverage of 3ML, b) profile of panel (a)

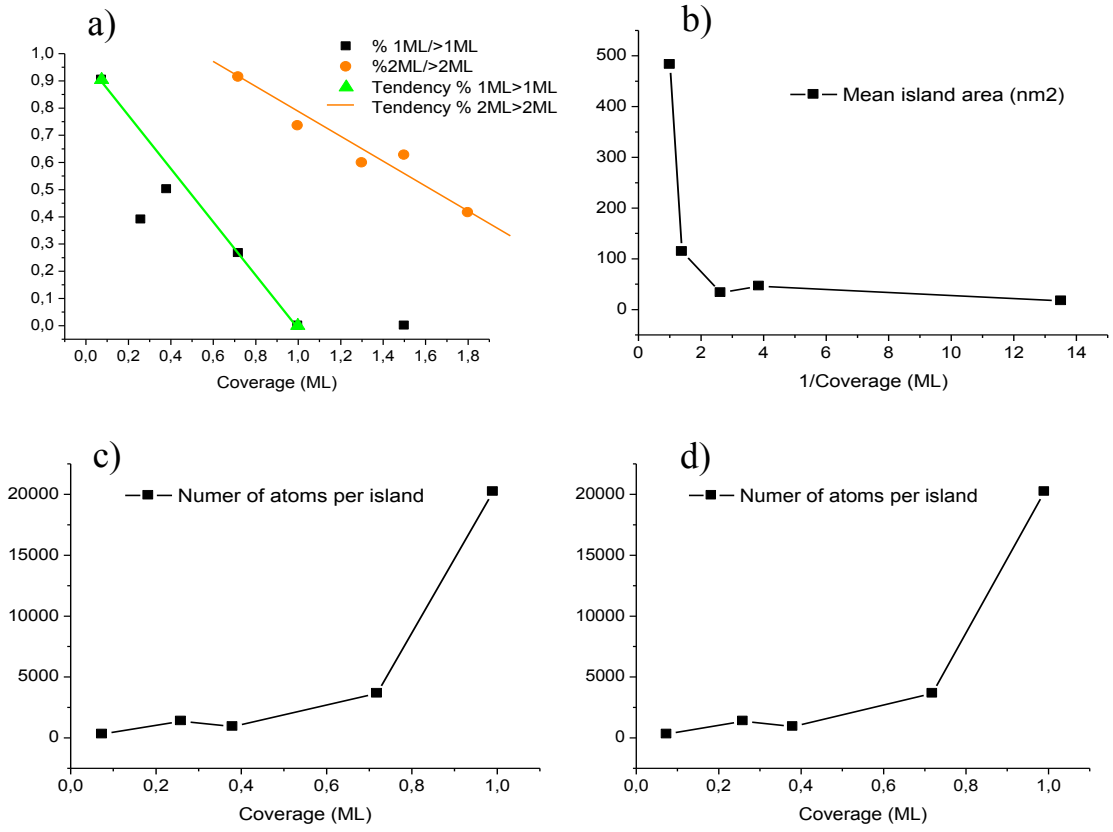

Figure 5.9: a) Proportion of 1ML-high (black) or 2ML-high (green) area to the whole area covered by Co, b) mean island size as a function of inverse coverage, c) mean island as a function of coverage, d) average number of Co atoms per islands, calculated by means of data from panel (a) and (c) and the atomic surface density from the table 4.1

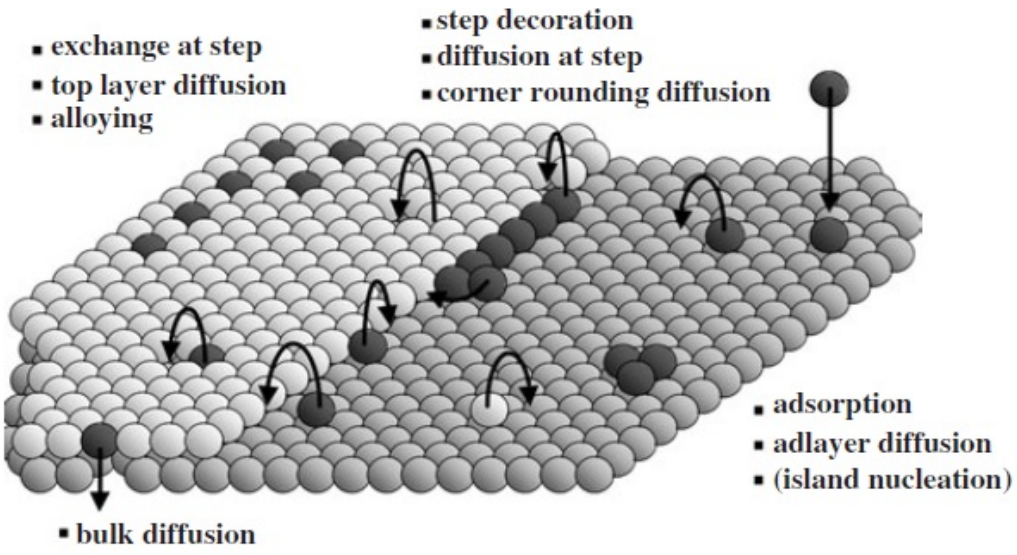

Figure 5.10: Surface processes relevant for growth on vicinal surfaces [7]

Next the virtue of the curved crystal (a gradual variation of the step density with a miscut angle) is used to study the dependency of the Co growth on the presence of the atomic steps. The effect of steps on the epitaxial growth can be illustrated by means of figure 5.10. The atoms arriving on the flat terrace land in the positions with only three nearest neighbors. However atoms reaching the ascending atomic step would attach to the site with higher coordination (five for the straight step or six in the kink position of the step). For many metallic surfaces higher coordination means higher binding energy, which makes atomic steps a sink for the adatoms [7].

Atoms approaching the descending atomic steps face an effective repulsion (so-called Ehrlich–Schwobel (ES) barrier [7]) because hopping from the upper terrace would involve a crossing of the corner with reduced coordination which is energetically unfavorable. Nevertheless, the probability of this process gets higher in the kink positions of the atomic steps. Progressive increasing of the number of the nucleated atomic layers with effective coverage was attributed to the more regular shape of the bigger islands (smaller relative number of kinks in the islands edges) and to the respective growth of the Ehrlich–Schwobel barrier in the study of the Co growth on the flat Pd(111) [23, 67].

Diffusion depends strongly on the temperature, but at 290 K the adsorbate atoms can move tens of lattice periods on the low index terraces easily [7]. Collision of the randomly moving adsorbed atoms leads to the formation of the clusters with reduced mobility which then serve as the centers of nucleation for the next atoms. The probability of these events depends on the flux of the arriving atoms. Higher evaporation rate makes the collisions more probable and therefore facilitates the nucleation of the islands. On the other hand small terrace width decreases the distance to the closest step and thus reduces probability of the formation of the islands.

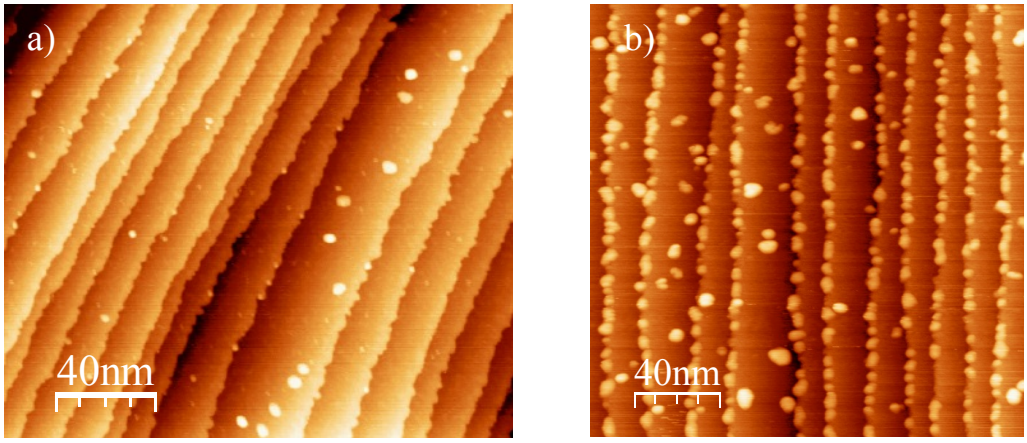

Figure 5.11: Progressive transition to the step decoration mode of growth of Co on curved Pd(111) for the effective coverage of 0.075ML (a) and 0.25ML (b)

A competition of these two processes leads to the change of the growth mode from the nucleation of islands in the big terraces to the step decoration in the smaller terraces. A step decoration mode of growth has been reported in the number of papers for Co, Ag, Cu, Fe and Mo on vicinal Pt(111) [7,76].

Figure 5.11 shows STM images collected in curved Pd(111), where the average terrace width L_{av} is close to 15nm (miscut angle α of 1^0), at the side of {111}-step side. Gradual disappearance of the islands within the terraces and transition to the step decoration growth mode is clearly seen for both 0.075ML (a) and 0.25ML (b) effective Co coverage. Similar to the case of the Co/vicinal Pt(111) system no major difference has been observed between the growth on {111}- and {100}-type steps of curved Pd(111) therefore in the following only the results for the {111}-type steps are reported.

Step decoration growth has been observed in the whole range of effective Co coverages and a critical value of the terrace width was found to be of 10-15 nm. In the range of small miscut angles the principal difference between the samples with different amount of Co is that for the 0.075ML sample, the Co island attached to the step is always 1ML-high (see figure 5.11 a). From 0.25ML to 0.72ML of effective Co coverage, the attached Co consists of 2ML-high separated islands (see figure 5.12 (a), (c) and (e)) and eventually for the sample with 1ML of effective Co coverage, the step decorating layer becomes a continuous 2ML high stripe (see figure 5.13).

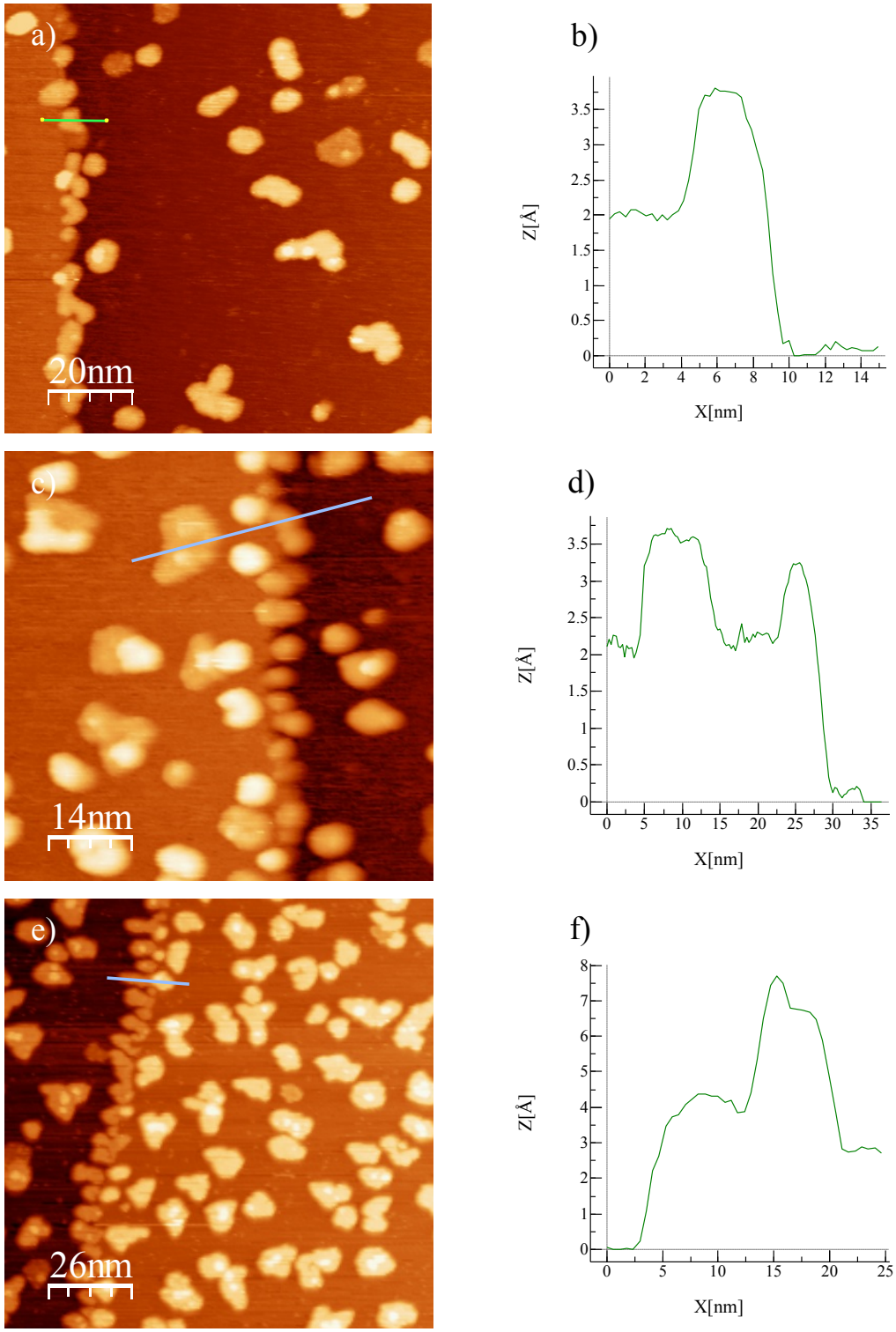

Figure 5.12: Step decoration mode of growth of Co on curved Pd(111) for the effective coverage of 0.25ML (a) and profile of fig a) (b), step decoration for 0.38ML (c) and profile of fig c (d), step decoration for 0.72 ML (e) and profile of e) (f). The three STM images correspond to the center of the crystal.

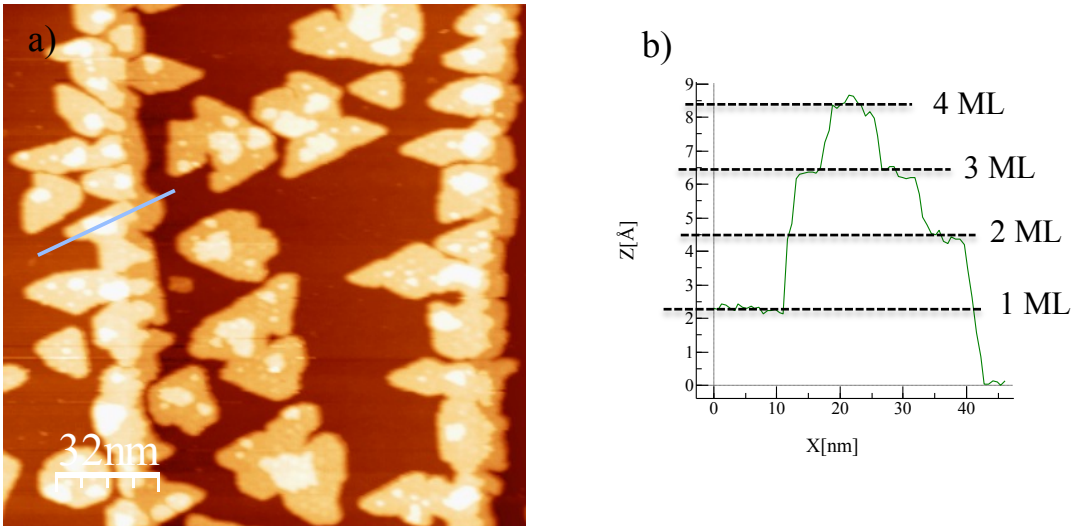

Figure 5.13: Step decoration for 1ML of Co effective coverage in the center of the crystal (a) and profile of fig a) (b)

The morphology of the attached Co layer depends on the diffusion processes. The Co atoms which arrive to the part of the step already decorated by other atoms can move along the edge of the Co stripe or turn the corner atom and hop to the bare step edge. If the mobility of the adatoms is not sufficient to pass the barrier concerned with the reduced coordination in the corner, the rough growth takes place. Otherwise an edge- smoothening is observed.

A phase diagram of the step decoration growth modes for the case of the Co/Pt(997) system was reported in Ref. [75]. It was shown that the edge-smoothening takes place above 250 K, and at 300 K the Co atoms starts to cross the border between the substrate and the step-decorating layer (see figure 5.14 a). Our data demonstrate that the mode of the step decoration growth depends also on the average thickness of the attached layer w. Indeed the islands nucleated at the step and representing initially the rough growth mode, expand laterally, and eventually start to coalesce.

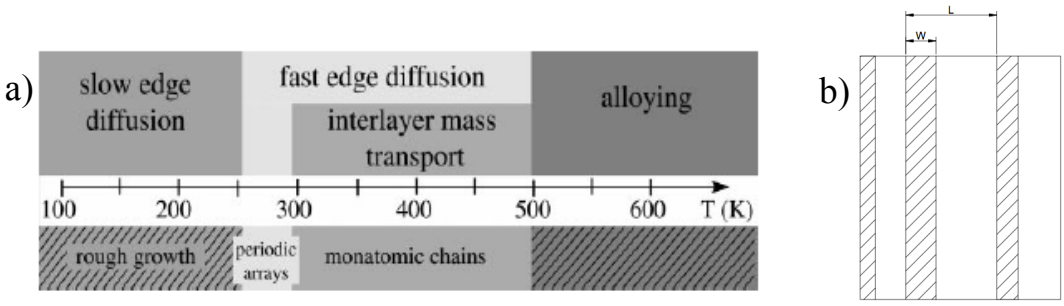

Figure 5.14: a) Different Co growth modes on Pt(997) as a function of the substrate temperature [75], b) a scheme illustrating that an amount of adsorbed material w is proportional to the terrace width L in the step decorating mode of growth

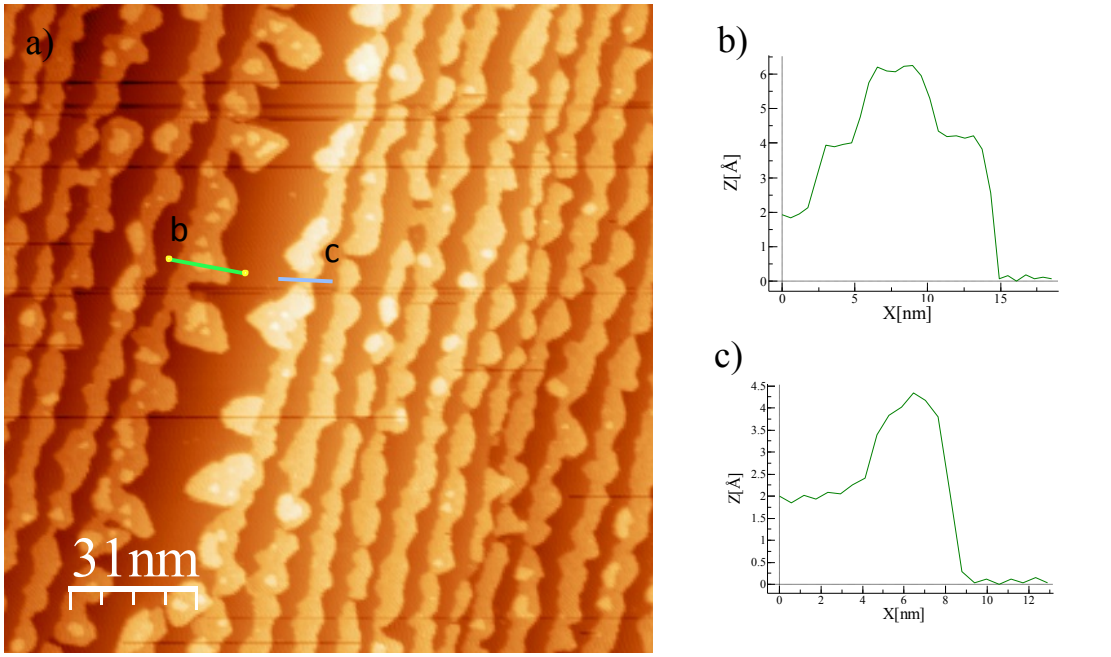

Figure 5.15: a) Step decoration for different terrace widths for 1ML effective Co coverage, b) profile of the decorated layer on the left, c) profile of the decorated layer on the right

Obviously a big enough terrace which can host the islands of the respective size is a prerequisite of this transition. According to the STM images from fig 5.12, rough growth mode takes place in the big terraces close to the center of the crystal from the lowest coverage up to 0.72ML. This mode of growth is characterized by 1 or 2ML high separated islands attached to the steps. For 1ML of effective coverage the edge smoothening takes place and cobalt grows as continuous 2ML high stripe attached to the step (see fig. 5.13).

On the other hand the repulsion of the deposited adatoms by the next descendent step also affects the morphology of the step decoration growth mode. For example figure 5.16 (a) shows that in the sample with 0.72 ML of the effective Co coverage the islands grow along the steps in the zone of the average terrace width of 5 nm (miscut angle α=2.7^0). Although in the same sample the islands were growing perpendicular to the steps in the range of the bigger terraces (see figure 5.12 e).

Except the geometrical restrictions that decreasing terrace width imposes on the size of the attached islands, reduction of the terraces results in the smaller average width of the attached Co layer *w*. Indeed figure 5.14 (b) shows that *w* and the average terrace width L_{av} are related to the effective coverage τ (expressed in ML) as:

$$w = L_{av}\tau \quad (1)$$

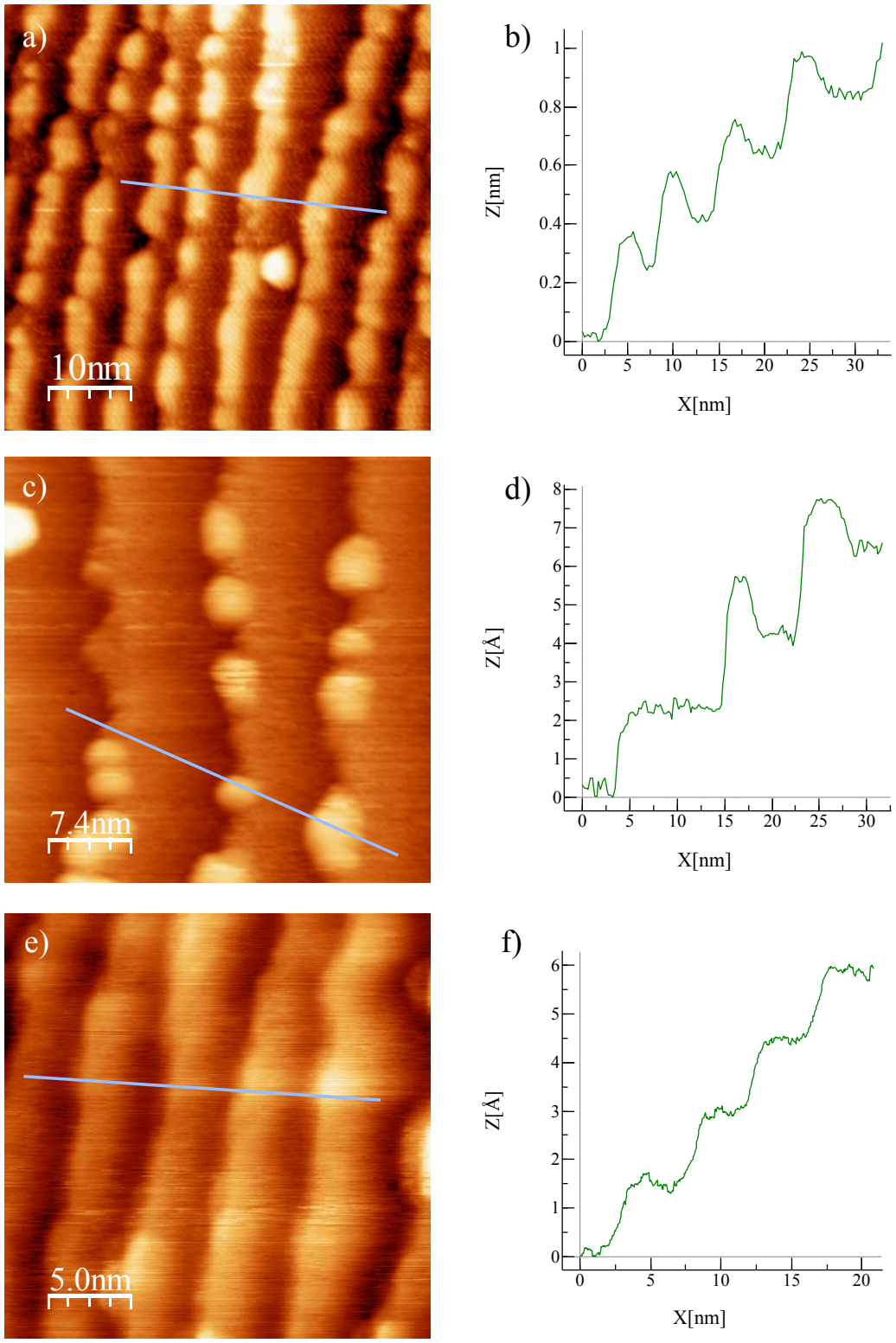

Figure 5.16 decoration of steps in the range of smaller terraces for the sample of 0.72 ML a), b) and 0.25 ML c)-f)

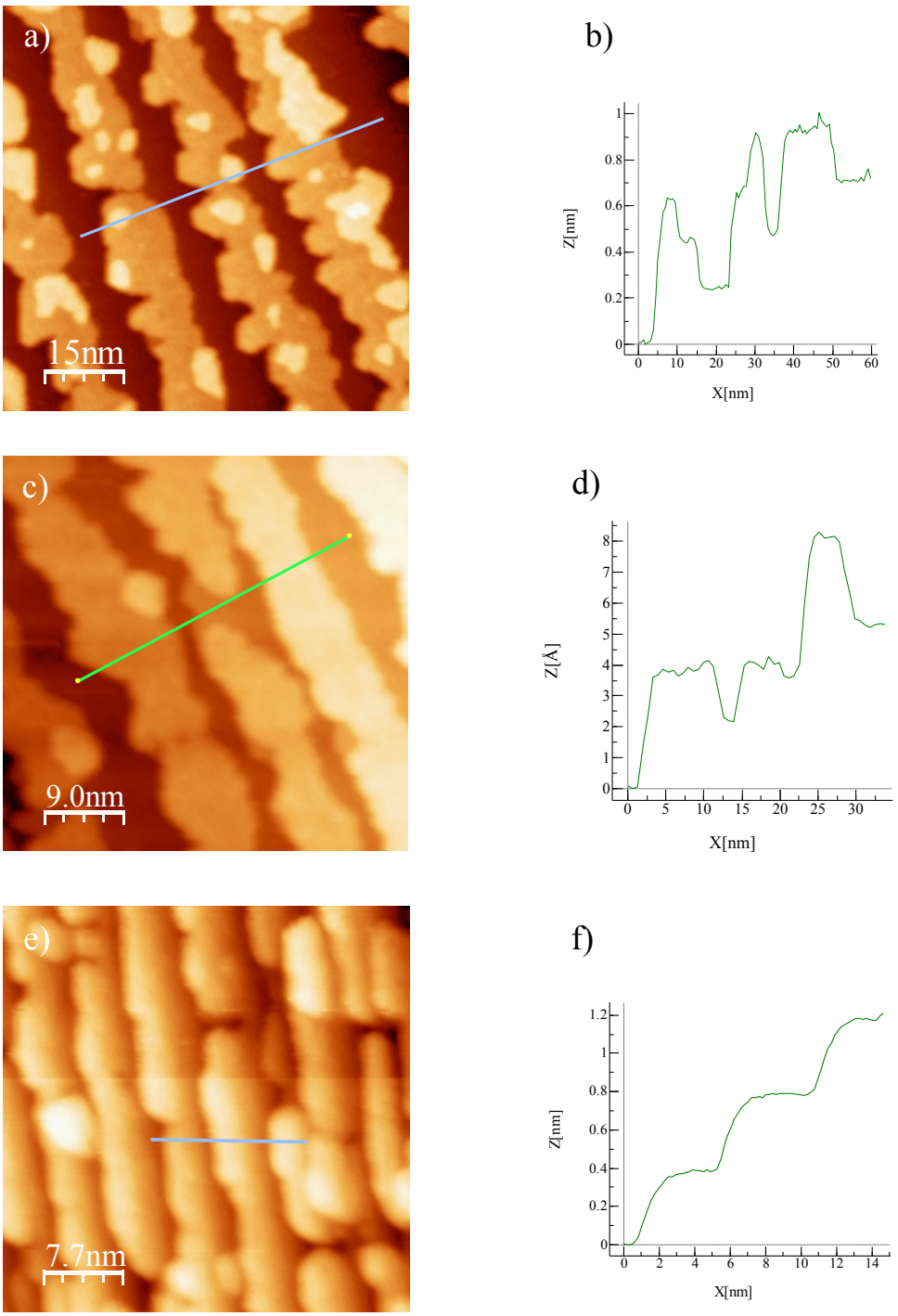

Figure 5.17: Step decoration mode of growth of Co on curved Pd(111) for the effective coverage of 1ML from moderate to small size terrace (a), (c), (e) and profile of the respective figures (b), (d) and (f)

This relationship visualized in figure 5.15 (a), measured in the sample with 1ML effective cobalt coverage. The attached cobalt layer on the biggest terrace of approximately 30 nm width is significantly wider than those layers attached on the rest of the terraces which consist of finer stripes along the step. Figures 5.16 (c) and (e) demonstrate that decreasing of the average width of the attached Co layer leads to the progressive change of the height of the step decorating adsorbate layer from two to the one atomic layer in the case of the 0.25 ML of effective Co coverage sample.

The effect of the reduction of the terrace width on the mode of Co growth for the sample with 1ML of effective Co coverage is shown in figure 5.17. 2ML high continuous stripes extended along the steps are shown in figure 5.17 (a). Figure 5.17 (c) shows the progressive change of the height of the step decorating adsorbate layer from two to one atomic layer, and finally monolayer stripes cover all the terrace surface in figure 5.17 (e). It is important to note that the profile of figure 5.17 f) shows the height of the cobalt attached to the step with a value corresponding to the height between one and two monolayers. However, for the same effective coverage only half of the surface is covered with the 2ML cobalt stripes, as it can be observed in figure 5.17 (a). Additionally, it was demonstrated that homogeneous evaporation of cobalt on the entire sample and thus the cobalt attached to the steps in figure 5.17 (e) must be 1 monolayer high.

5.2 Growth of Cobalt on curved Ni(111)

The growth of Co on curved Ni(111) surface was studied for four different values of the effective Co thickness (see table 5.3). The substrate has been cleaned in UHV in accordance with the protocol specified in the part 4.2. The evaporation rate of cobalt (0.15ML/min) was the same as for the preparation of Co on curved Pd(111). During the evaporation the substrate was kept at room temperature.

The mobility of Co adatoms at room temperature on Ni(111) terraces apparently is higher than on Pd(111). In fact, the critical terrace width of the transition from the islands to the step decoration growth mode in Ni(111) is 30-35 nm, which is almost double of the critical terrace width for Pd(111) (see part 5.1). Figure 5.18 (a) shows a STM image of the intermediate regime with 0.1ML of effective Co thickness. The profile shown on the figure 5.18 (b) demonstrates that both the separate islands and the islands attached to the steps are 1ML high.

Figure 5.19 illustrates the STM topography data collected in the large terraces in the central part of the crystal (the miscut angle $\alpha=0^0$) as a function of the effective Co coverage. Cobalt islands keep growing one monolayer high for 0.03 and 0.1 ML. The size of the islands significantly increases with increasing the effective cobalt thickness. The second layer starts to nucleate in the 0.5ML sample (see fig 5.19 (c)), and in the 0.75ML sample the third layer was observed (see fig 5.19 (d)). Nevertheless the majority of Co surface has only 1ML height in both cases.

Preparation	Coverage (ML)
1	0.03
2	0.1
3	0.5
4	0.75

Table 5.3: Deposited effective cobalt coverage

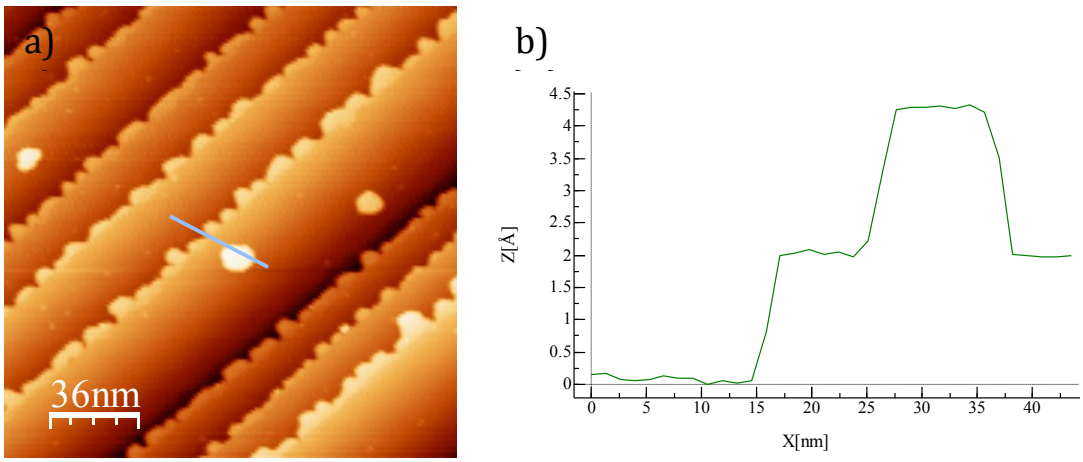

Figure 5.18: a) STM image ($180x180nm^2$) taken in the central part of the crystal ($\alpha=0^0$) for 0.1ML effective cobalt coverage. b) Profile of figure a.

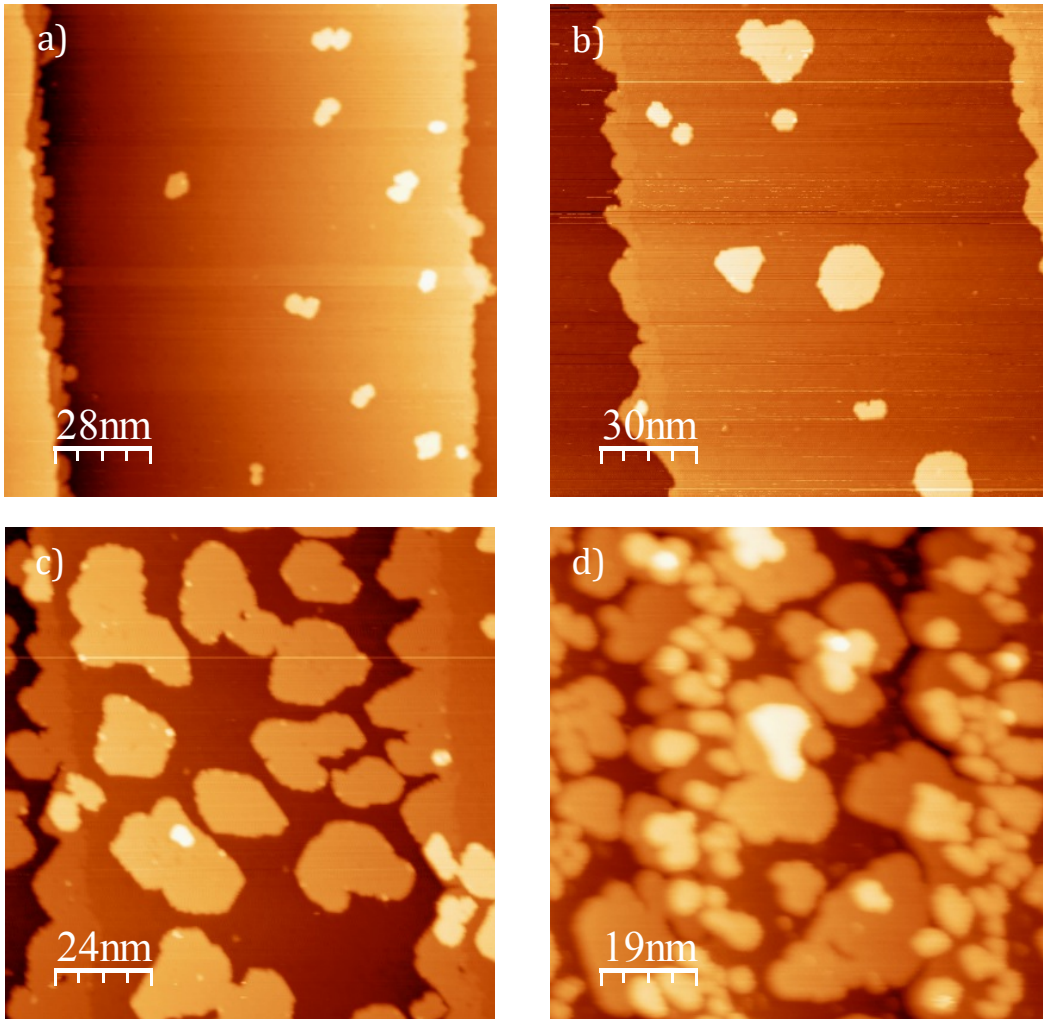

Figure 5.19: STM image in the central part of the crystal with effective cobalt coverage of a) 0.03ML, b) 0.1ML, b) 0.5ML, d) 0.75ML

These data cannot be compared directly with results of other investigations because to our knowledge the study of the growth of cobalt on single crystal nickel substrate has not been reported yet. Nevertheless, the growth of epitaxial bi and multilayers of Co/Ni has been an object of active research because of their importance for applications [21]. For instance, the growth of Co wedges on different low index surfaces of copper single crystal with a 4ML Ni buffer has been studied by means of LEED [77]. The lattice mismatch between Cu and Ni is 2.5% which leads to the in-plane expansion (tensile strain) and out-of-plane contraction of Ni layer due to the pseudomorphic growth. Cobalt was found to grow coherently on this strained Ni buffer up to 30ML in a layer-by-layer mode.

Unstrained nickel layers are obtained by incoherent Ni growth on substrates with larger lattice mismatch. For example, the moiré pattern of LEED observed in the case of 1ML Co/1ML Ni/Pt(111), evolves into a regular atomic six-fold pattern with increasing Co thickness, which was interpreted as a relaxation via formation of dislocations [78]. A thorough investigation by means of the Reflection High Energy Electron Diffraction, X-Ray diffraction and Transmission Electron Microscopy shows

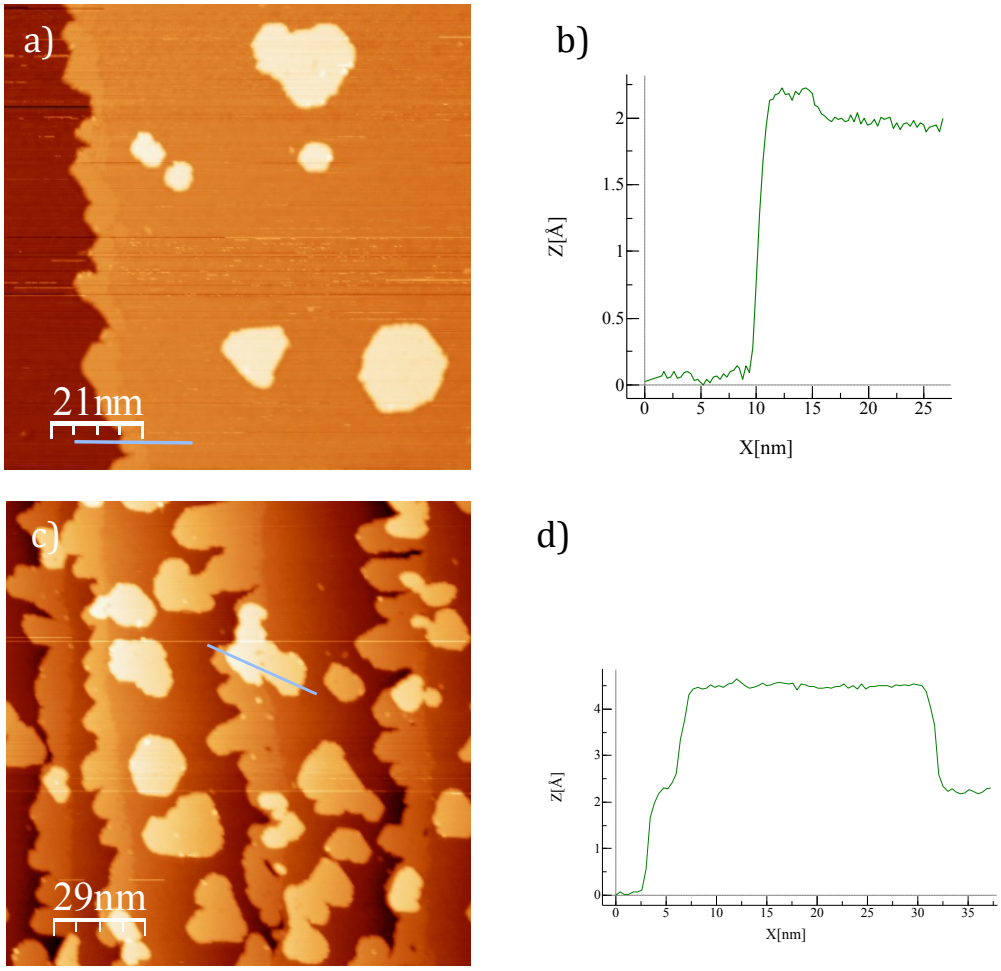

Figure 5.20: a) STM image (105x105nm^2) for 0.1ML cobalt effective coverage, b) profile of Figure a, c) STM image (145x145nm^2) for 0.5ML cobalt effective coverage, d) profile of figure c.

that Ni/Co multilayer grows on the sapphire substrate with V(110)/Au(111) buffer maintaining a relaxed fcc structure that is incommensurate to that of Au [22, 79]. The cobalt/nickel growth mode was found to be layer-by-layer without any intermixing.

Next, we studied the influence of the atomic steps on the cobalt growth. Since the general tendency for the Co/cNi(111) is a continuous 2D layer formation, the effect of steps is not that strong as it was in the case of Co/cPd(111). Step decoration observed in the terraces smaller than 30-35 nm leads to the formation of continuous 1ML high cobalt stripes attached to the ascending steps, similar to the case of Co/vicinal Pt(997) [75] or Ag /vicinal Pt(997) [7] (see figure 5.20). Nucleation of the islands partially covering the attached stripes demonstrates that the barrier between Ni and Co does not prevent the diffusion of Co atoms from the upper terrace towards the steps (see figure 5.20 (c)).

The shape of the cobalt stripes is irregular showing that the diffusion along the cobalt island edge is not sufficient to trigger smoothening and the step-flow growth. Nevertheless, decreasing of the average width of the attached Co stripe, which occurs

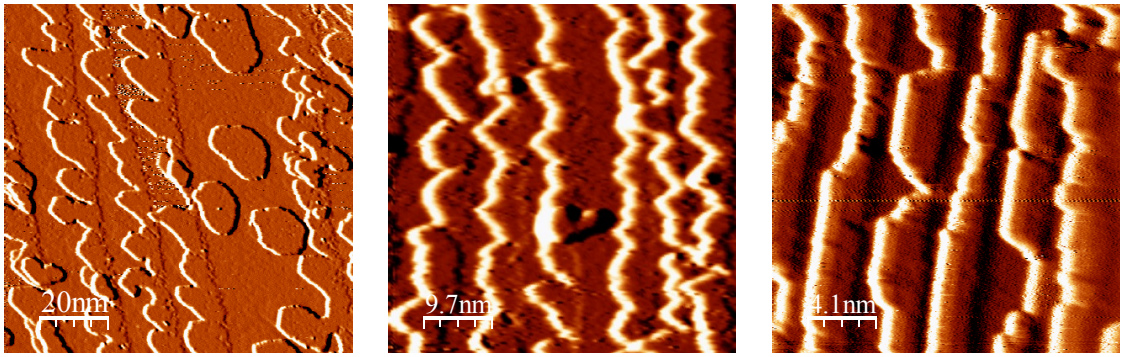

Figure 5.21: Cobalt growth as a function of the density of steps for 0.5ML effective coverage

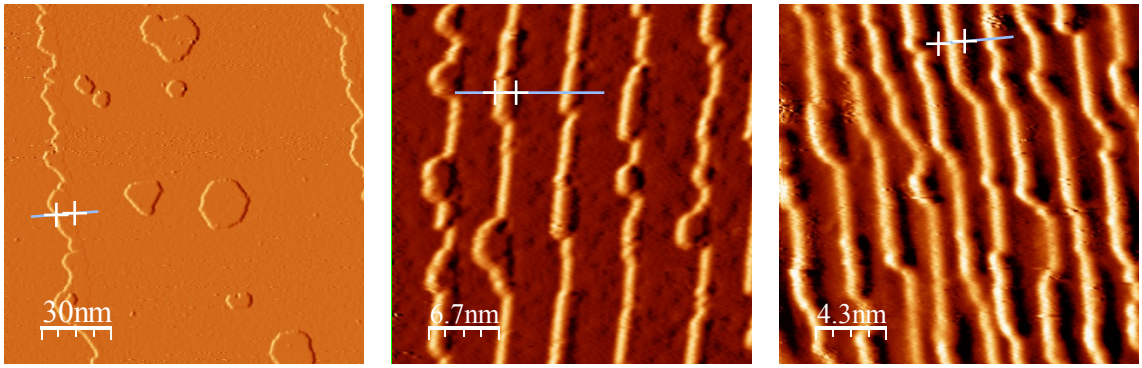

Figure 5.22: Cobalt growth as a function of the density of steps for 0.1ML effective coverage.

according to the equation (1) of part 5.1 with decreasing of the terrace width, leads to the gradual straightening of the Co edge as it can be seen in figure 5.21. It illustrates the evolution of the step decorating layer as a function of the miscut angle for the 0.5ML sample and demonstrates that in 4 nm wide terraces Co stripes consist of straight parts with characteristic length equal to 2-3 times the width of the terrace.

This effect is even more pronounced in the sample with 0.1ML effective cobalt coverage. Figure 5.22 shows that in the wide central terrace Co grows as a rough stripe of 6 nm average width (panel (a)). Meanwhile in the 5 nm wide terrace wide the Co stripes are straighter with long parts of 1-1.5 nm width. And eventually 3 nm wide terraces features the Co stripes which are partially thinner than 1 nm (see panel (c)). This means that they comprise only 2-3 atomic rows and can be already considered as 1D objects.

This last result shows that using of the curved crystal as substrate allows to realize and study the gradual transition from the 2D to 1D growth mode in one sample.

6. Magnetic properties of cobalt

The investigation of the magnetic properties of Co nanostructures grown on the curved Pd and Ni crystals was performed by means of the XAS/XMCD measurements in the Deimos beamline of the synchrotron Soleil, and at Boreas beamline of the synchrotron Alba. In both cases the samples were prepared in-situ in the respective preparation chambers connected to the end-stations. It allowed to handle the samples without breaking the UHV conditions. Therefore we did not use any protective capping layers. Technical characteristics of both chambers are available in section 2.4.

Since the diameter of the X-ray beam (0.08 mm) is much smaller than the size of the substrates, few zones with different effective Co coverage were grown on each crystal at once, as it is schematically shown in figure 6.1. Use of samples in the form of such stepped wedge drastically reduces the time for the preparation of the experiment, because it takes smaller number of transferences between the chambers, alignments of the beam with the sample and cooling cycles. Furthermore, the wedged sample allows better control of the amount of cobalt because the flux is stabilized and then only the shutter is moved without disturbing the evaporation.

The manipulator at the end station allows the movement of the sample in the plane perpendicular to the X-ray beam and rotation as it is shown in the figure 6.2. Therefore the X-ray absorption experiments were performed as a function of the cobalt coverage and the miscut angle of the curved surface in normal incidence (OOP) and grazing incidence (GI) geometry (the range of the incidence angles is +/-60 deg). The magnetic

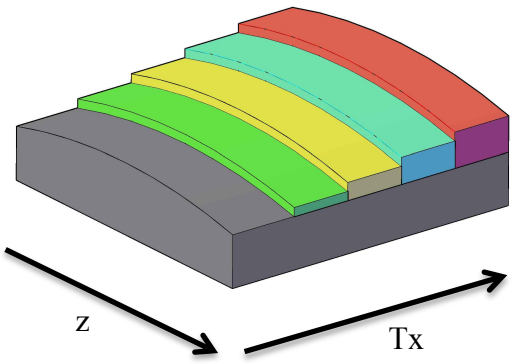

Figure 6.1: Schematic representation of the stepped wedge structure of the samples.

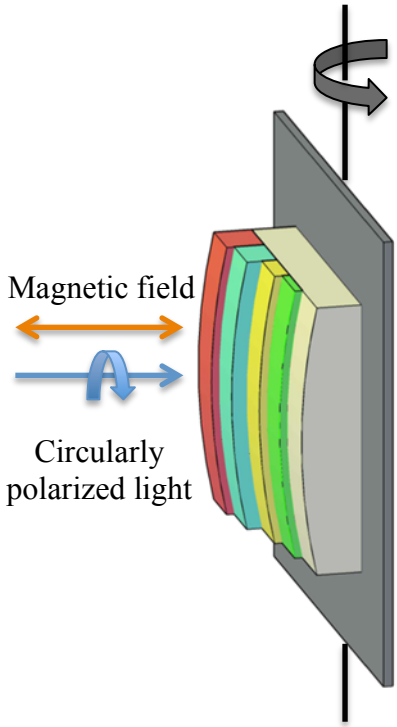

Figure 6.2: Orientation of the magnetic field, X-ray beam and sample in the end station.

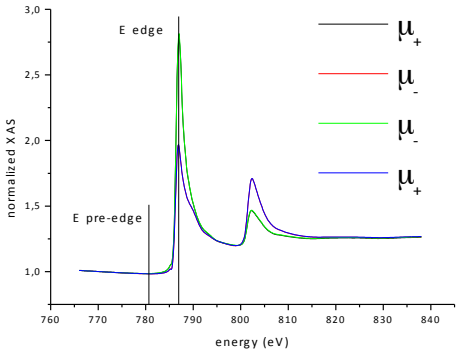

Figure 6.3: XAS absorption spectra measured for Co/Ni in normal incidence

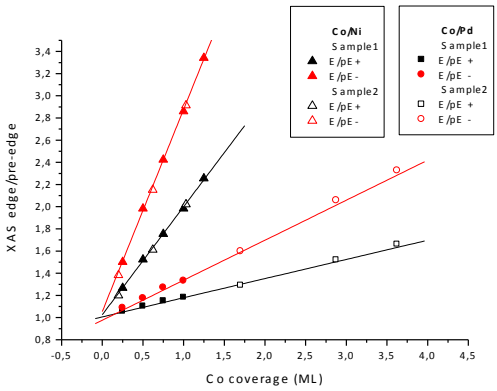

Figure 6.4: Normalized XAS L_3 edge/pre-edge intensities, measured at normal incidence

field with amplitude of up to 6 Tesla was always parallel to the X-ray beam. According to the configuration of the deposited cobalt wedge the position along the z axis corresponds to the miscut angle while the position along the *Tx* axis refers to the cobalt effective thickness.

The substrates were cleaned by means of the sputtering/annealing using the parameters from section 4. Co was evaporated from the rod using e-beam heating at relatively low rate of 0.15ML/min. The stability of the evaporation rate was monitored by the integrated fluxmeter. The accuracy of the relative calibration was crosschecked using the intensity of the L_3 XAS absorption edge normalized to the intensity of the pre-edge (see figures 6.3 and 6.4). These values were found to be linear function of the effective Co coverage in each preparation. The offset between the lines obtained for different preparations was corrected so that all data measured for the same substrate follow the same straight line.

The calibration of the absolute value of the deposition rate has been done by means of STM. An amount of Co approximately equivalent to 1 complete monolayer was evaporated at the same rate monitored using the integrated fluxmeter on the clean Au (111) surface. Since Co grows on this substrate as 2ML high islands [73], the exact amount of Co was then determined as the double of the covered/total area ratio in few STM topography images. The precision of this method is not very high (around 25%) because of the convolution of the tip and the surface topography. However, the precision of the relative amount of Co calibrated by means of XAS spectra is better than 10%.

From XAS spectra, we determine the XMCD spectra, and then calculate the orbital and spin moments of Co by means of the Sum rules (see part XMCD technique). Furthermore, the XMCD signal was recorded as a function of field (XMCD magnetization loops). All these measurements were done at 2.5 K.

6.1 Magnetism of cobalt on curved Pd(111)

Two different Co wedges have been grown on the curved Pd(111) crystal. The total number of the studied Co coverages is seven (see table 6.1). First wedge has four different zones with effective Co coverage from 0.25 to 1ML and second has three zones. Furthermore one segment of the substrate was always left clean to measure the background absorption spectra. Each zone of the constant cobalt thickness is 1.5mm wide and covers all the curvature of the crystal. The shape of the wedge and the positions of the different zones were probed using the XAS intensity measured at two constant energies as a function of the coordinate. Figure 6.5 shows the difference between the XAS measured at the energy of L_3 Co edge and pre-edge in the central part of the crystal (miscut angle $\alpha=0^0$). Since the value of this difference is proportional to the effective thickness of the Co layer the presented curve can be considered as a profile of the wedge. Vertical lines show the points chosen to measure the XAS spectra. The homogeneity of the Co coverage for each zone was checked using the XAS edge minus XAS pre-edge curves measured along the z direction.

Magnetization loops measured in the central part of the crystal (miscut angle $\alpha= 0^0$) in normal incidence (OOP magnetic field) are shown in figure 6.6. Samples with effective Co coverage of 0.5-1.0ML have remanent magnetization equal to the saturation

c_Pd (111)	Cobalt coverage (ML)				
Sample 1	clean	0.25	0.5	0.75	1
Sample 2	clean	1.7	2.9	3.6	

Table 6.1: Cobalt coverages of the two wedges on the curved Pd (111)

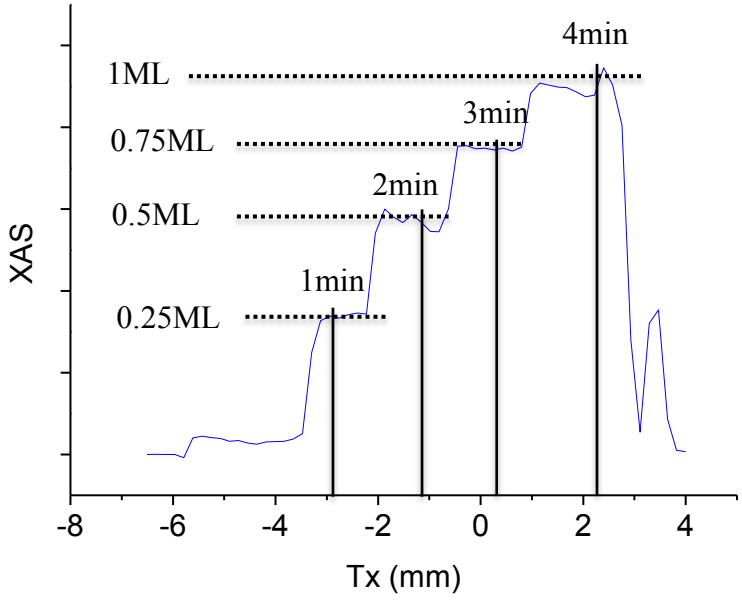

Figure 6.5: Profile of the Co wedge number one, grown on the curved Pd(111)

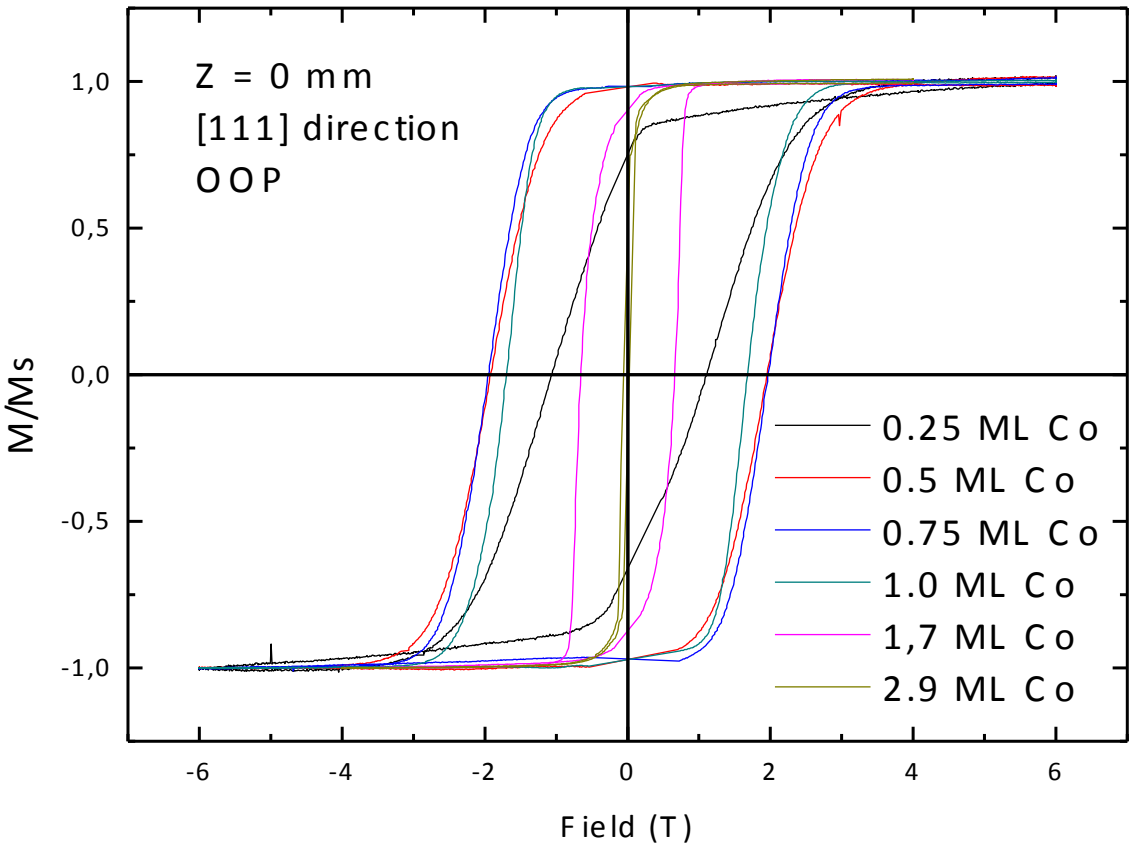

Figure 6.6: OOP magnetization loops measured in the central part of the Pd crystal (miscut angle $\alpha=0^0$) for increasing Co thickness.

magnetization which means that the OOP direction is the easy-magnetization direction. Since Co grows on the large terraces of Pd(111) as separate islands (see part 5.1), the high coercive field of 1.95 T shows that these islands are single-domain magnetic particles. The magnetization loop of the 0.5ML sample measured in grazing incidence (magnetic field at 60 degrees with respect to the OOP direction) has a remanent magnetization equal to half of the saturation magnetization and its shape is characteristic of Stoner-Wohlfarth magnetic particles (see figure 6.7b) [48] therefore we concluded that these Co islands possess uniaxial magnetic anisotropy.

The coercive field H_C allows to calculate the anisotropy energy (K) of the Co islands. Within the Stoner-Wohlfarth model it can be done by means of the relationship:

$$H_C = \frac{2K}{M}$$

where M is a magnetic moment (1.8 μ_B/Co atom). Using the value of H_C of 1.95 T we get the anisotropy of K=0.1 meV/at similar to K=0.15-0.2meV/at reported in [81,82-83] for Co/Au(111).

The blocking temperature (T_b) of the islands can be estimated using the average number of Co atoms per island presented in figure 5.9 (d) of part 5.1. With the estimated anisotropy of Co of K=0.1 meV/at, the anisotropy of islands with 2000 atoms

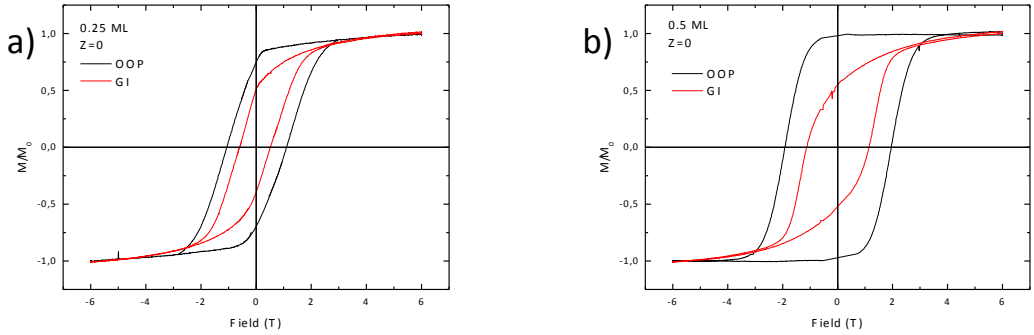

Figure 6.7: Magnetization loops measured in OOP and GI configurations for a) 0.25ML and b) 0.5ML samples in the central part of the Pd curved crystal (miscut angle $\alpha=0^0$)

(average number for 0.5ML sample) is 200 meV, which is equivalent to T_b of 93 K. The magnetization loop of the sample with effective Co coverage of 0.25ML has a coercive field of 1.1 T and its remanent magnetization makes up only 75% of the saturation magnetization. Figure 6.7 (a) shows that both loops measured in OOP and GI geometry approach the saturation asymptotically. These features can be explained by the influence of the thermal agitation in the smaller Co islands at 0.25 ML coverage. Indeed the coercive field of the 0.5ML sample measured at 2.5 K (H_C=1.95 T) can be taken as a good estimate of its zero-temperature value of H_C because the blocking temperature of this sample is much higher than the temperature of the measurements. Within the Stoner-Wohlfarth model the coercive field does not depend on the size of the particle, therefore this value can be used also as an estimate of the zero-temperature H_C of the 0.25ML sample. Using the value of the coercive field at 2.5 K its blocking temperature can be calculated using the Sharrock law (see part 2.3) as

$$T_b = T\left(\frac{H_0}{H_0 - H_c}\right)^{3/2}$$

which yields T_b of 8.7 K. Taking into account that a sample with 0.25ML of effective Co coverage consists of islands having in average 1300 Co atoms per island (see figure 5.9 (d)) the anisotropy can be calculated using the equation (see part 2.3):

$$K = \frac{25 k_b T_b}{N_{atoms}}$$

which yields a value of 0.015 meV/at. It is much lower than 0.1 meV obtained previously for the 0.5ML sample. Therefore, the magnetic properties of Co are different in the case of smaller islands of 0.25ML sample then in the bigger islands of 0.5-1.0ML samples. This observation correlates with a transition from the growth of Co as 1ML high islands observed for the low coverages to the growth as 2ML high islands in the samples of 0.72 and 1.0ML of effective coverage (see part 5.1).

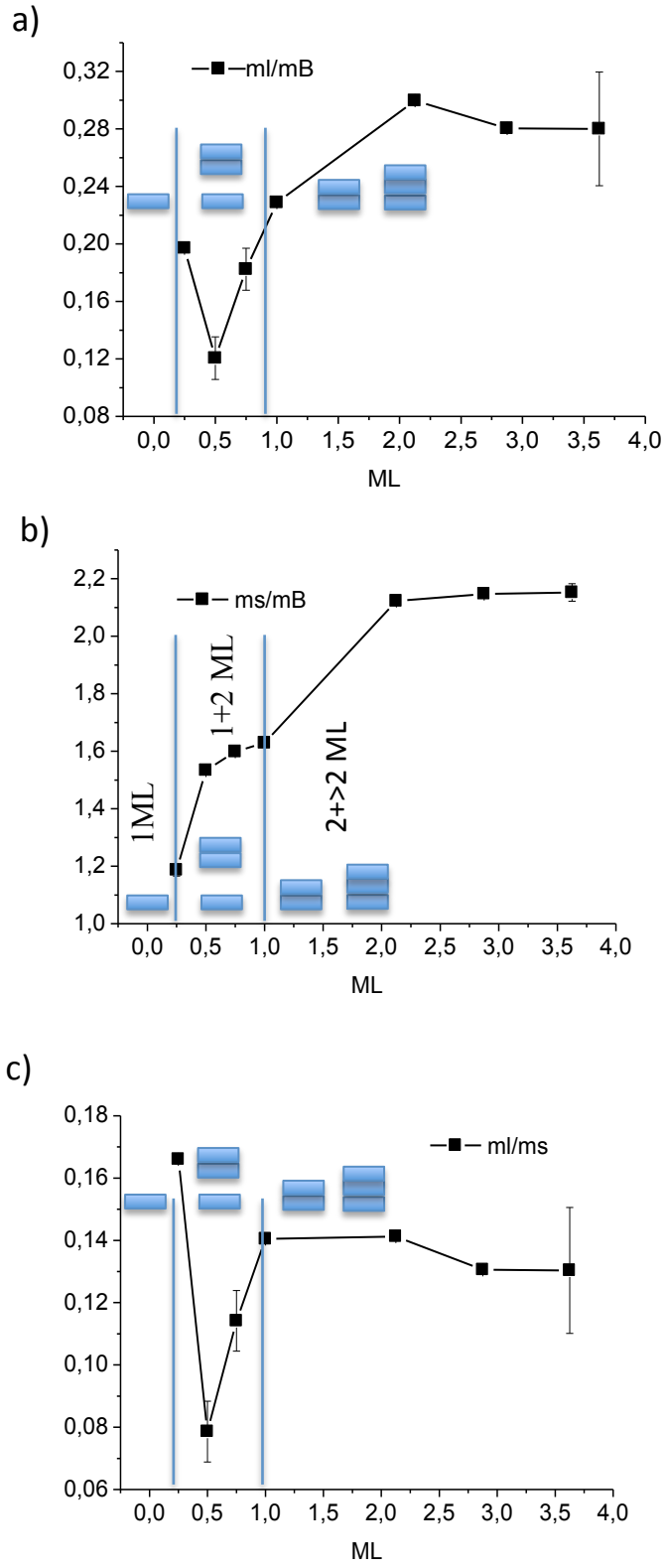

Figure 6.8: Orbital moment m_L a), effective spin moment m_{Seff} b) and the ratio c) as a function of the effective Co coverage, measured in the center of the Pd(111) sample (miscut angle $\alpha=0^0$)

Magnetization loops measured for the samples with effective Co coverage of 1.7ML and 2.9ML have coercive field of 0.67 T and 0.09 T respectively. Remanent magnetization is also lower than M_s, however, both of these samples are saturated inthe field only a little bit higher than the respective coercive field (H_S is 1 T and 0.2 T). This behavior can be attributed to the multi-domain state of the samples. Coercive field of 0.09 T is typical for the continuous Co films [84, 85], therefore the effective coverage of 2.9ML is higher than the percolation threshold. This value agrees well with the percolation threshold of 2.3ML reported in [23] and our STM data (see part 5.1).

The magnetic properties of Co atoms were calculated using the experimental XMCD

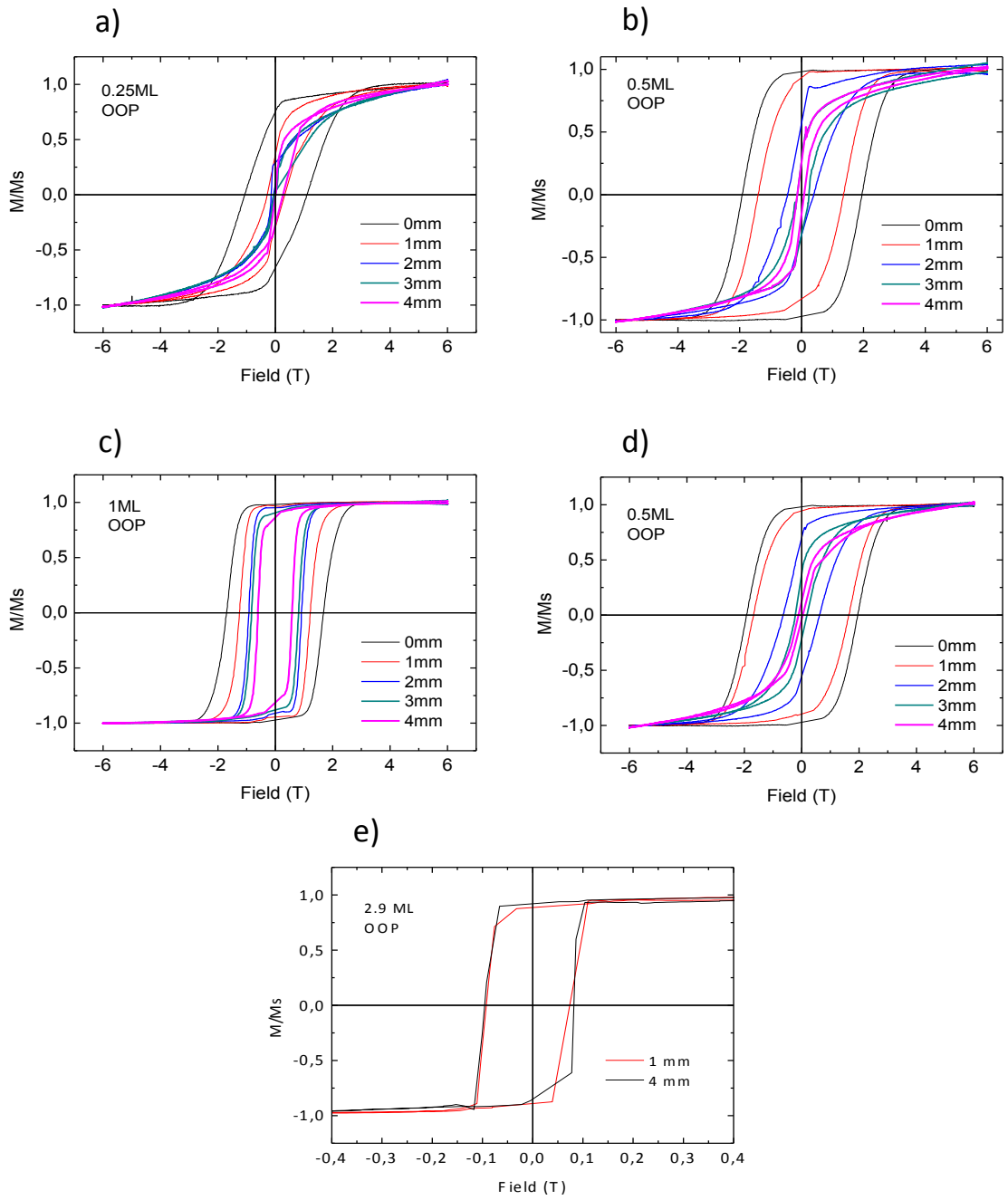

Figure 6.9: XMCD magnetization loops measured at the L_3 Co edge as a function of the miscut angle on the side of {111} type steps a), b, c) and e) and on the side of {100} type steps d)

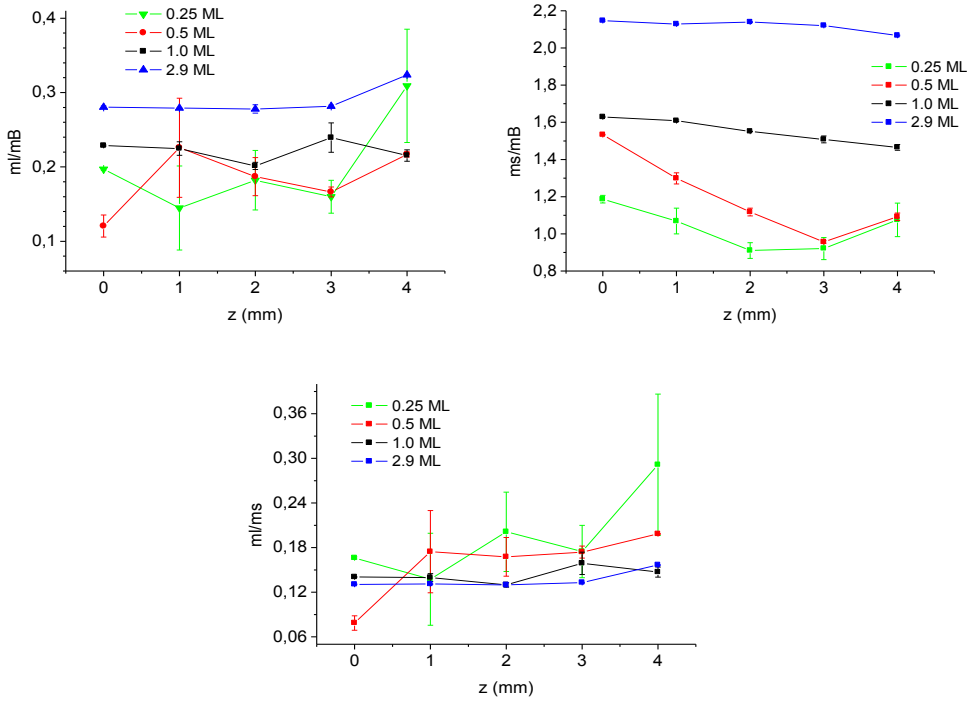

Figure 6.10: Orbital moment m_L a), effective spin moment m_{Seff} b) and their ratio c) measured at different miscut angles of curved Pd(111). 1mm of z corresponds to the change of α of 2.4^0

spectra by means of the Sum Rules (see part 2.4). Orbital moment m_L, effective spin moment m_S and their ratio are plotted as a function of the effective Co coverage in figures 6.8 (a), (b) and (c), respectively. These data were collected in the central part of the curved Pd(111) crystal (miscut angle $\alpha=0^0$).

All three parameters have distinctive features in the lowest measured value of Co coverage which can be attributed to the transition from 2ML to 1ML high islands growth. An orbital moment of $0.31\mu_B$ has been reported for strained 1ML-high islands of Co grown on Pt(111) [86]. The change of the tendency at 1ML effective Co coverage correlates with a nucleation of the third atomic layer in the Co islands, observed in 5.1 (see figure 5.9 a). The characteristic values of hcp ($m_L=0.15\,\mu_B$, $m_S=1.55\,\mu_B$, $m_L/m_S=0.099$) agree with experimental data for the 0.75ML sample. Elevated values of m_L observed for 2.9ML sample meets the predictions made for ultrathin fcc Co films [87]. Intermediate values observed in the rest of the samples can be attributed to the coexistence of different phases (one and two monolayer high islands, fcc and hcp domains) which is corroborated by our STM data (see part 5.1).

Figure 6.9 shows magnetization loops measured for few different Co coverages at different miscut angles. The sample having 0.5ML of effective Co coverage has been studied on both sides of {111}- and {100}-type steps. Both sets of the loops are very similar (see figure 6.9 (b) and (d)), which supports the conclusion drawn in chapter 5.1 that both sides of the crystal are essentially symmetric. The rest of the presented loops were measured on the {111}-side of the sample.

Samples with 0.25 and 0.5ML effective Co coverage demonstrate similar tendencies (see figures 6.9 (a), (b) and (d)): the coercive field decreases and the loops become more S-shaped with increasing miscut angle. This trend is consistent with the rough mode of the step decoration growth discussed in part 5.1 for 0.075 and 0.25ML samples. The gradual transition to the superparamagnetic behavior shows that the islands get smaller (in average) in the smaller terraces and therefore they are not connected.

In contrast the loops measured for the 1ML sample stay rectangular (see figure 6.9 (c)), the remanent magnetization is close to its saturation value, and only the coercive field decreases. Our STM data show that in the wide central terraces of the 1ML sample Co grows as separated 2ML-high islands, whereas in thinner terraces it decorates the steps forming continuous stripes (edge-smoothening mode). The second Co layer nucleates on these stripes in the range of moderate terraces, but when terraces get narrower the amount of Co per unit length of the step decreases and the second layer disappears gradually. Therefore decreasing of the coercive field is explained by change of the Co layer morphology (transition from 2ML-high single domain islands to continuous 1ML-high stripes). It is worth to note that the coercive field of Co stripes in the lateral part is close to the coercive field observed in the central part of 0.25ML sample (see figure 6.9 (a)), which corroborates the observation that majority of Co islands in the central part of this sample are 1ML high.

Eventually the loops measured for the 2.9ML sample almost do not change with miscut angle α (see figure 6.9 (e)). Indeed, the Co film is continuous for this value of the effective coverage and there is no size (and therefore temperature) effect, that is why both coercive field and remanent magnetization stay almost intact along the miscut angle. It contrasts to the behavior of the thin Fe film grown on the curved Pt(111) where the easy-magnetization direction deviates gradually from the OOP direction with increasing density of steps of the substrate [88].

Variation of the atomic Co properties with α miscut angle is shown in figures 6.10 (a), (b) and (c) where the orbital moment mL, effective spin moment m_S and their ratio are plotted as a function of α. These dependencies are not monotonous which reflects complex combination of different phases in the step decoration growth mode. However there is a clear trend: both m_L and m_L/m_S grow with increasing miscut angle for the 0.25 and 0.5ML samples (where the rough step decoration mode was observed) and both of these values remain almost constant for the 1.0 and 2.9ML samples where the step decoration was continuous (edge-smoothening in 1ML sample) or where the film is continuous (2.9ML sample).

6.2 Magnetism of cobalt on curved Ni(111)

Two different Co wedges have been grown on the curved Ni(111) crystal. The total number of the studied Co coverages is eight (see table 6.1). The first wedge has five different zones with effective Co coverage from 0.25 to 1.25ML and second has three zones. Furthermore one segment of the substrate was always left clean to measure the background absorption spectra. Each zone of the constant cobalt thickness is 1.5 mm wide and covers all the curvature of the crystal.

The shape of the wedge and the positions of the different zones were probed using the XAS intensity measured at two constant energies as a function of the coordinate. Figure 6.11 shows the difference between the XAS measured at the energy of L_3 Co edge and pre-edge in the central part of the crystal (miscut angle $\alpha=0^0$). Since the value of this difference is proportional to the effective thickness of the Co layer the presented curve can be considered as a profile of the wedge. Vertical lines show the points chosen to measure the XAS spectra. The homogeneity of the Co coverage for each zone was checked using the XAS edge minus XAS pre-edge curves measured along the z direction.

c_Ni (111)	Cobalt coverage (ML)					
Sample 1	clean	0.25	0.5	0.75	1	1.25
Sample 2	clean	0.2	0.6	1		

Table 6.2 Cobalt coverages of the two wedges on the curved Ni(111)

Figure 6.12 shows XMCD magnetization loops measured at the L_3 Co edge (a) and L_3 Ni edge (b) in the OOP configuration for the sample with 1ML of effective Co coverage. Both loops are almost identical which demonstrates that magnetic moments of Co are exchange-coupled to the moments of the Ni substrate. Since the total moment of Ni crystal is much bigger than the moment of the thin Co film its interaction with external field is stronger and it follows the field direction dragging the coupled Co moments. The shape of the Ni magnetization loop (zero remanent magnetization, zero coercivity) is characteristic of the sample with the easy-magnetization direction perpendicular to the applied field. It matches up with the form of the substrate which possesses in-plane shape anisotropy

Atomic properties of the Co were calculated using the experimental XMCD spectra by means of the Sum Rules (see part 2.4). Orbital moment m_L, effective spin moment m_S and their ratio are plotted as a function of the effective Co coverage in figures 6.13 (a), (b) and (c), respectively. These data were collected in the central part of the curved Ni(111) crystal (miscut angle $\alpha=0^0$). Both orbital and effective spin moments slowly grow with increasing effective Co coverage which reflects progressive nucleation of the second layer. Nevertheless, the variation of these values is smaller than in the case of

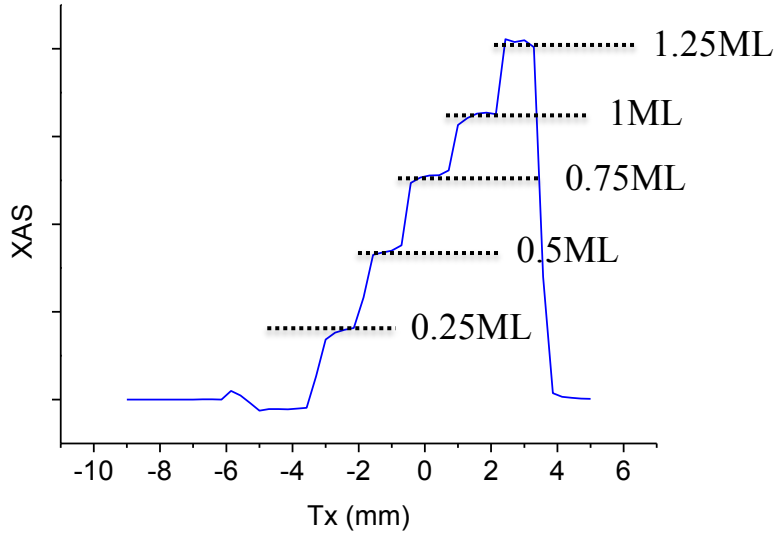

Figure 6.11: Thickness profile of Co wedge 1, grown on the curved Ni(111) surface

Co/cPd(111) (see figure 6.8). The ratio m_L/m_S remains almost constant in the whole studied range of coverages.

Variation of the atomic Co properties with α miscut angle is shown in figures 6.14 (a), (b) and (c) where the orbital moment m_L, effective spin moment m_S and their ratio are plotted as a function of α. The most striking result is that the orbital moment m_L does not increase with increasing miscut angle but instead it slowly decreases and the ratio m_L/m_S again remains almost constant for all studied samples. Meanwhile Co growth in the step decoration mode on terraces of 0.25 and 0.5ML samples is close to percolation, forming almost a continuous film in the 1ML sample. It means that the growth of the orbital moment m_L with decreasing terrace width observed in Co/cPd(111), and also reported in the Co/Pt(997) [86], is not concerned with reduced coordination in the thin Co stripes but it rather originates from stronger deformation of less rigid thin objects. Increasing of the orbital Co moment accompanying transition from 2ML-high to 1ML-high Co islands growth in the wide central terraces of Pd(111) (see figures 6.8 (a) and (c)) corroborates this conclusion.

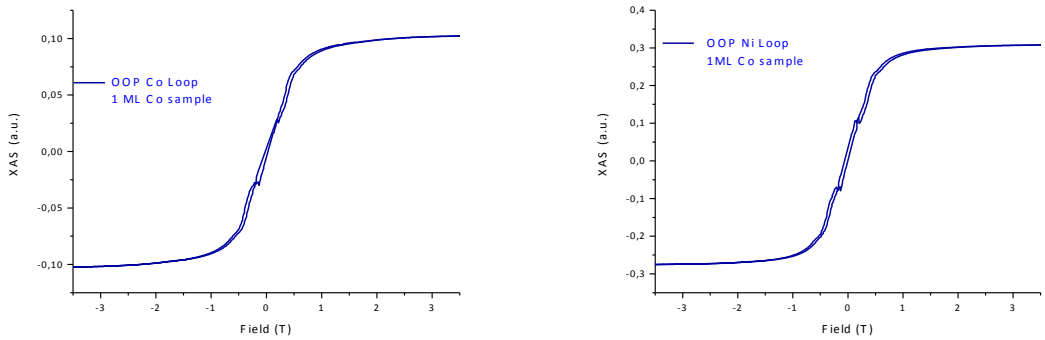

Figure 6.12: XMCD magnetization loops measured on the L_3 Co edge a) and L_3 Ni edge b) in the OOP configuration for the sample with 1ML of effective Co coverage

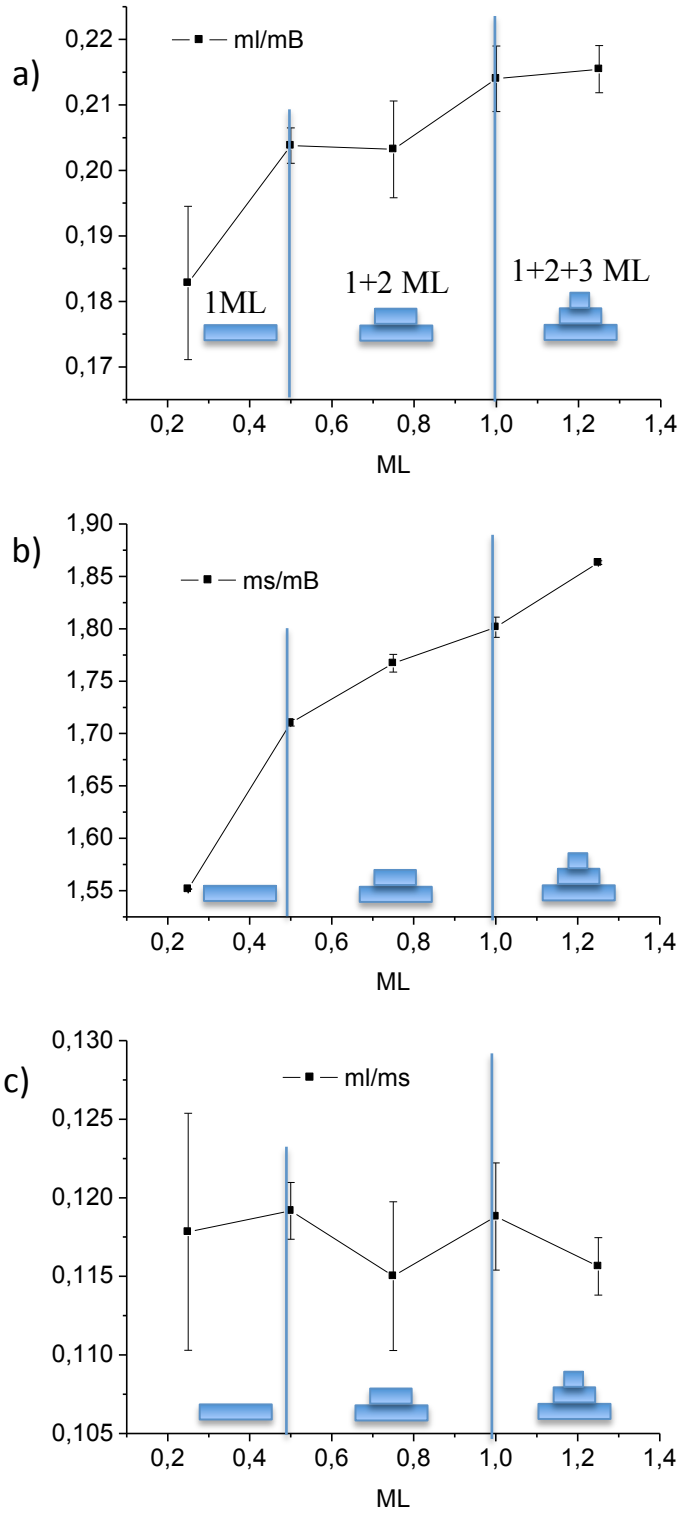

Figure 6.13: Orbital moment m_L a), effective spin moment m_{Seff} b) and the ratio c) as a function of the effective Co coverage, measured in the center of the Ni(111) sample (miscut angle $\alpha=0^0$)

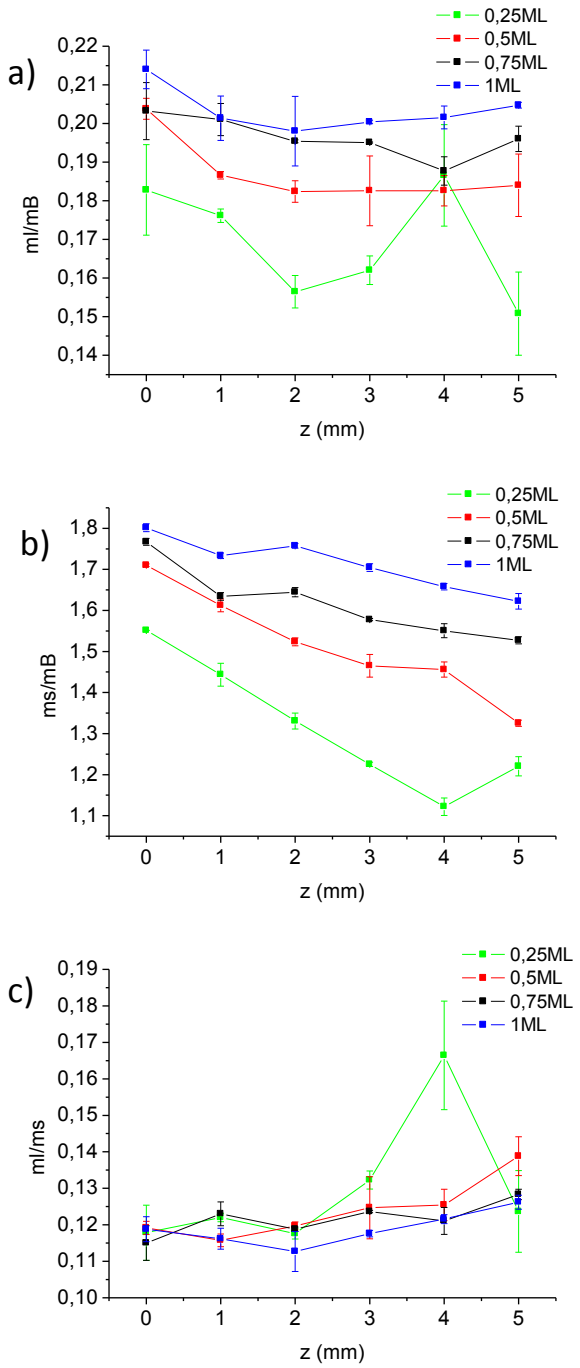

Figure 6.14: Orbital moment m_L a), effective spin moment m_{Seff} b) and their ratio c) measured at different miscut angles of the curved Ni(111). 1mm of z corresponds to a change in α of 2.4^0

7. Conclusions

Summarizing the results obtained in this work following major achievements should be mentioned:

1. A set of tools has been manufactured and the procedure of polishing has been developed to produce curved Pd(111) and Ni(111) single crystals. Other crystals, namely Bi and Cu were also testes successfully. Established technology has been transferred to the spin-off company where it was further developed up to the commercial production level.

2. The ordered microstructure of the variable vicinal surfaces of curved Pd(111) and Ni(111) single crystals was studied in-situ by means of STM and LEED. The surface of both crystals was found to be made of flat (111) terraces separated by monoatomic steps. Minor formation of diatomic steps in cPd(111) did not break the symmetry of the {111}- and {100}-type steps sides of the crystal. However in the cNi(111) the majority of steps is diatomic for miscut angles larger than 6^0 on the {100}-side of the crystal.

3. Growth of cobalt on curved Pd(111) and Ni(111) was studied by means of STM. Formation of separated Co islands was observed in the big central terraces, and step decoration growth in terraces smaller than a characteristic critical size. Change of the step decoration mode from the rough growth to the edge-smoothening regime was observed in cPd(111), as a function of both the effective Co coverage and the average terrace width.

4. The investigation of the magnetic properties of cobalt nanostructures by means of the XMCD technique revealed that the gradual transition from 2D islands to 1D stripes with decreasing average terrace width leads to the growth of the orbital moment of cobalt for Co/cPd(111), but practically does not change its value for Co/cNi(111). Thus implies that it is a substrate-induced stress rather than reduced coordination that affects the value of the orbital moment in these systems.

Other contributions not included in this thesis:

5. Construction of the MOKE/STM setup

6. Assembling and test of the low temperature manipulator and cryostat/compressor

References

[1] H. C. Jeong and E. D. Williams. *Steps on surfaces: experiment and theory*. Surface Science Reports **34**, 171 (1999).

[2] B. Joós, T. L. Einstein, and N. C. Bartelt. Phys. Rev. B **43**, 8153 (1991).

[3] E.D. Williams and N. C. Bartelt. *Thermodynamics of Surface Morphology*. Science **251**, 393 (1991).

[4] F. Tao, S. Dag, L.-W. Wang, Z. Liu, D. R. Butcher, H. Bluhm, M. Salmeron and G.A. Somorjai. Break-Up of Stepped Platinum Catalyst Surfaces by High CO Coverage.Science **327**, 850 (2010).

[5] J. G. Wang, W. X. Li, M. Borg, J. Gustafson, A. Mikkelsen, T. M. Pedersen, E. Lundgren, J. Weissenrieder, J. Klikovits, M. Schmid, B. Hammer, and J. N. Andersen. One-Dimensional PtO2 at Pt Steps: Formation and Reaction with CO. Physical Review Letters **95**, 256102 (2005).

[6] S. Rousset, V. Repain, G. Baudot, Y. Garreau and J. Lecoeur. J. Phys.: Condens. Matter **15**, S3363 (2003).

[7] K. Kuhnke, K. Kern J. Phys.: Condens. Matter **15**, S3311 (2003).

[8] A. Mugarza and J. E. Ortega. J. Phys.: Condens. Matter **15** S3281 (2003).

[9] A. Mugarza, F. Schiller, J. Kuntze, J. Cordon, M. Ruiz-Oses and J. E. Ortega. J. Phys.: Condens. Matter **18**, S27 (2006).

[10] J. E. Ortega, M. Corso, Z. M. Abd El-Fattah, E. A. Goiri and F. Schiller. Interplay between structure and electronic states in step arrays explored with curved surfaces. Physical Review B **83**, 085411 (2011).

[11] M. Corso, F. Schiller, L. Fernández, J. Cordón, and J. E. Ortega. Electronic states in faceted Au (111) studied with curved crystal surfaces. J. Phys.: Condens. Matter **21**, 353001 (2009).

[12] W. Ranke, Y. R. Xing and G. D. Shen. Surf. Sci. **122**, 256 (1982).

[13] W. Ranke and Y. R. Xing. Surf. Sci. **157**, 339 (1985).

[14] H. J. Kuhr and W. Ranke. Surf. Sci. **187**, 98 (1987).

[15] R. K. Kawakami, E. J. Escorcia-Aparicio and Z. Q. Qiu. Phys. Rev. Lett. **77**, 2570 (1996).

[16] E. J. Escorcia-Aparici, H. J. Choi, W. L. Ling, R. K. Kawakami and Z. Q. Qiu. Phys. Rev. Lett. **81**, 2144 (1998).

[17] H. J. Choi, R. K. Kawakami, E. J. Escorcia-Aparicio, Z. Q. Qiu, J. Pearson, J. S. Jiang, D. Li and S. D. Bader. Phys. Rev. Lett. **82**, 1947 (1999).

[18] H. Nakanoa, S. Kawakamia, T. Fujitanib and J. Nakamura. Surface Science **295**, 454 (2000).

[19] L. Vattuone, L. Savio and Mario Rocca. Surface Science Reports **63**, 101 (2008).

[20] A. Loui and S. Chiang. Applied Surface Science **237**, 555 (2004).

[21] M. T. Johnson, P. J. H. Bloemen, F. J. A. den Broeder and J. J. de Vries. Rep. Prog. Phys. **59**, 1409 (1996).

[22] M. Gottwald, S. Andrieu, F. Gimbert, E. Shipton, L. Calmels, C. Magen, E. Snoeck, M. Liberati, T. Hauet, E. Arenholz, S. Mangin, and E. E. Fullerton. Phys. Rev. B **86**, 014425 (2012).

[23] M. Wasniowska, N. Janke-Gilman, W. Wulfhekel, M. Przybylski and J. Kirschner. Surface Science **601**, 3073 (2007).

[24] H. Luth. Solid Sufaces, Interfaces and Thin Films. Springer, 2011.

[25] J. S. Hong, W. Jo, K. J. Ko, N. M. Hwang, D. Y. Kim. Philosophical Magazine **89**, 2989 (2009).

[26] A. Mugarza. *Electronic Structure of Low-Dimensional Systems Analyzed by Angle*-Resolved Photoemission Spectroscopy. PhD thesis. University of the Basque Country, 2002.

[27] H. Ibach. Physics of surfaces and interfaces. Springer, 2006.

[28] E. D. Williams and N. C. Bartelt. Science **251**, 393 (1991).

[29] M. Giesen. Progress in Surface Science **68**, 1 (2001).

[30] S. Rousset, F. Pourmir, J.M. Berroir, J. Klein, J. Lecoeur, P. Hecquet, B. Salanon Surface Science **422**, 33 (1999).

[31] M. Giesen. Step step interaction energy on Cu (111) vicinal surfaces. Surf. Rev. Lett. **6**, 17 (1999).

[32] M. Giesen and T. L. Einstein. Surface Science **449**, 191 (2000).

[33] T. L. Enstein. Appl. Phys. A **87**, 375 (2007).

[34] A. Chame, S. Rousset, H. P. Bonzel, J. Villain. Bulgarian Chemical Communications **29**, 398 (1997).

[35] H.-C. Jeong and J. D. Weeks. Scanning Microscopy **12**, 17 (1998).

[36] T. Ihle, C. Misbah and O. Pierre-Louis. Phys. Rev. B **58**, 2289 (1998).

[37] “http://www.virginia.edu/ep/SurfaceScience/electron_interactions.htm”.

[38] “http://www.hk-phy.org/atomic_world/stm/stm03_e.html”.

[39] G. Moulas. Growth and Magnetism of 2D Bimetallic Nanostructures. PhD thesis. École Polytechnique Fédérale de Lausanne, 2008.

[40] P. Gambardella. *Growth, Electronic Structure and Magnetism of Supported Metal Nanowires*. PhD thesis. École Polytechnique Fédérale de Lausanne, 2000.

[41] G. Binning, H. Rohrer, Ch. Gerber, and E. Weibel. Phys. Rev. Lett. **58**, 1 (1982).

[42] E. Goiri. *Structure and Electronics of Donor-Acceptor Blends*. PhD thesis. University of the Basque Country, 2014.

[43] F. Besenbacher. Rep. Prog. Phys. **59,** 1737 (1996).

[44] R. C. O'Handley. Modern Magnetic Materials. New York, Wiley, 2000.

[45] E. C. Stoner and E. P. Wohlfarth. *A Mechanism of Magnetic Hysteresis in Heterogeneous Alloys.* Phil. Trans. Lond. Ser. A, 1948.

[46] B. D. *Cullity and* C. D. *Graham. Introduction to Magnetic* Materials. New York, Wiley-IEEE Press, 2008.

[47] S. Bedanta and W. Kleemann. J. Phys. D: Appl. Phys. **42**, 013001 (2009)

[48] A. H. Morrish. *The Physical Principles of Magnetism*. New York, Wiley, 1965.

[49] H. N. Bertram and H. J. Richter, J. Appl. Phys. **85**, 4991 (1999).

[50] J. Stöhr, H. C. Siegmann. *Magnetism – From Fundamentals to Nanoscale Dynamics*. Berlin, Springer, 2006.

[51] C. T. Chen, Y. U. Idzerda, H. -J. Lin, N. V. Smith, G. Meigs, E. Chaban, G. H. Ho, E. Pellegrin, and F. Sette. Phys. Rev. Lett. **75**, 152 (1995).

[52] F.M.F. de Groot and A. Kotani. *Core Level Spectroscopy of Solids*. New York, Taylor & Francis, 2008.

[53] T. Y. Lee. Growth and magnetism of low-dimensional metallic nanostructures on the Pt (997) surface. PhD thesis. École Polytechnique Fédérale de Lausanne, 2005.

[54] E. Beaurepaire, H. Bulou, F. Scheurer, J. P. Kappler. Magnetism: A Synchrotron Radiation Approach. Lect. Notes Phys. 697. Berlin, Springer Heilderberg, 2006.

[55]"http://www.synchrotronsoleil.fr/Recherche/LignesLumiere/DEIMOS#TechnicalData.pdf"

[56] "https://www.cells.es/en/beamlines/bl29-boreas".

[57] "http://www.scientaomicron.com/en/products/variable-temperature spm/instrument-concept**"**

[58] "http://www.scientaomicron.com/en/products/spectaleed-/instrument-concept"

[59] L. Bjerregaard, K. Geels, B. Ottesen and M. Rückert. Metalog Guide. Denmark, Struers, 1992.

[60] L. Niu, D.D. Koleske, D.J. Gaspar, S.F. King, S.J. Sibener. Surf. Sci. **356**, 144 (1996)

[61] T.P. Pearl and S.J. Sibener. Chem. Phys. **115**, 1916 (2001).

[62] T.P. Pearl, S.B. Darling, L. Niu, D.D. Koleske, D.J. Gaspar, S.F. King and S.J. Sibener. Chem. Phys. Lett. **364**, 284 (2002).

[63] R.C. Cinti, T.T.A. Nguyen, Y. Capiomont and S. Kennou. Surf. Sci. **134**, 755 (1983).

[64] G. Cosma, G. Mechtersheimer and B. Poelsema. Surf. Sci. **119**, 159 (1982).

[65] G. Hoogers and D.A. King. Surf. Sci. **286**, 306 (1993).

[66] R. V. Mom, C. Hahn, L. Jacobse and L. B.F. Juurlink. Surface Science 613, 15 (2013).

[67] M. Wasniowska, W. Wulfheke, M. Przybylski and J. Kirschner. Phys. Rev. B 78, 035405 (2008).

[68] A. Atrei, G. Rovida, M. Torrini, U. Bardi, M. Gleeson, C.J. Barnes. Surf. Sci. **372**, 91 (1997).

[69] S.J. Oh, W. Kim, B.H. Choi, J.Y. Kim, H. Koh, H.J. Kim and J.H. Park. Appl. Surf. Sci. **169**, 127 (2001).

[70] A. Murdoch, A.G. Trant, J. Gustafson, T.E. Jones, T.C.Q. Noakes, P. Bailey and C.J. Baddeley. Surface Science **608**, 212 (2013).

[71] S. Boukari, E. Beaurepaire, H. Bulou, B. Carriere, J.P. Deville, F. Scheurer, R.Baudoing-Savois and M. De Santis. Surf. Sci. 430, 37 (1999).

[72] S.T. Purcell, M.T. Johnson, N.W.E. McGee, J.J. Devries, W.B. Zeper and W. Hoving. J. Appl. Phys. **73**, 1360 (1993).

[73] J. Kim, J.-W. Lee, J.-R. Jeong, S.-K. Kim, S.-C. Shin. Appl. Phys. Lett. **79**, 93 (2001).

[74] J. Kim, J.-W. Lee, J.-R. Jeong, S.-K. Kim, S.-C. Shin, J. Appl. Phys. **89**, 7147 (2001).

[75] P. Gambardella, M. Blanc, L. Burgi, K. Kuhnke and K. Kern. Surface Science **449**, 93 (2000).

[76] P. Gambardella, M. Blanc, H. Brune, K. Kuhnke and K. Kern. Phys. Rev. B **61**, 2254 (2000).

[77] M. T. Johnson, J. J. de Vries, N. W. E. McGee, J. de Stegge, F. J. A. den Broeder Phys. Rev. Letters **69**, 3575 (1992).

[78] H.Y. Ho and C.S. Shern. Japanese Journal of Applied Physics **50**, 083001 (2011).

[79] S. Girod, M. Gottwald, S. Andrieu, S. Mangin, J. Mc Cord, E. E. Fullerton, J. M. L. Beaujour, B. J. Krishnatreya, and A. D. Kent. Appl. Phys. Lett. **94**, 262504 (2009).

[80] B. Voigtlander, G. Meyer and N. M. Amer. Phys. Rev. B **44**, 10354 (1991).

[81] N. Weiss, T. Cren, M. Epple, S. Rusponi, G. Baudot, S. Rohart, A. Tejeda, V. Repain, S. Rousset, P. Ohresser, F. Scheurer, P. Bencok, and H. Brune. Phys. Rev. Lett. **95**, 157204 (2005).

[82] S. Rohart, V. Repain, A. Tejeda, P. Ohresser, F. Scheurer, P. Bencok, J. Ferre and S. Rousset. Phys. Rev. B **73**, 165412 (2006).

[83] T. Koide, H. Miyauchi, J. Okamoto, T. Shidara, A. Fujimori, H. Fukutani, K. Amemiya, H. Takeshita, S. Yuasa, T. Katayama, and Y. Suzuki. Phys. Rev. Lett. **87**, 257201 (2001)

[84] C. Clavero, L. Martínez, A. García-Martín, J. M. García-Martín, Y. Huttel, N. D. Telling, G. van der Laan, A. Cebollada, and G. Armelles. Phys. Rev. B **77**, 094417 (2008).

[85] V. Grolier, J. Ferre, A. Maziewski, E. Stefanowicz and D. Renard. J. Appl. Phys. **73**, 5939 (1993).

[86] P. Gambardella, A. Dallmeyer, K. Maiti, M. C. Malagoli, W. Eberhardt, K. Kern, C. Carbone Nature **416**, 301 (2002).

[87] R. Wu, C. Li and A. J. Freeman. J. Mag. Magn. Mater. **99**, 71 (1991).

[88] R. Cheng, S. D. Bader and F. Y. Fradin. Phys. Rev. B **77**, 024404 (2008).

Publications/Contributions

- L. Fernández, M. Blanco-Rey, M. Ilyn, L. Vitali, **A. Magaña**, A. Correa, P. Ohresser, J.E. Ortega, A. Ayuela and F. Schiller. *Nano Lett.*, **2014**, 14 (6), pp 2977–2981.
- A. Cavallin, L. Fernández, M. Ilyn, **A. Magaña**, M. Ormaza, M. Matena, L. Vitali, J.E Ortega, C. Grazioli, P. Ohresser, S. Rusponi, H. Brune, and F. Schiller. *Phys. Rev. B* **2014**, *90*, 235419.
- M. Ilyn, L. Fernandez-Recuero, **A. Magaña**, P. Ohresser, J. Enrique Ortega, and Frederik Schiller "Magnetic properties of the ultrathin Co films grown on the curved Ni(111) and Pd(111) single crystals". Accepted for oral presentation in the 13th Joint MMM-Intermag Conference. January 2016 San Diego, USA.
- M. Ormaza, M. Ilyn, L. Fernandez-Recuero, **A. Magaña**, B. Xu, M. Diakhate, M. J. Verstraete, L. Vitali, A. Ayuela, M. Blanco-Rey, F. Schiller, and J. E. Ortega. "High temperature ferromagnetism in a $GdAg_2$ monolayer nanotemplate" (in preparation).
- L. Fernandez, M. Ilyn, **A. Magaña**, L. Vitali, J. E. Ortega, and F. Schiller. "Enhanced magnetic anisotropy in Co nanodots on a Au(111) trigon network" (in preparation).
- AUSE: Congress (2013). Poster: Transition from superparamagnetic to film-like behaviour for Co nanodots grown on a $GdAu_2$ surface *compound.*
- *Fuerzas y Tunel: Congress (2014). Poster:* The mode of growth and magnetic properties of ultrathin Co films grown on curved the Pd(111).

SYNCHROTRON STAYINGS

- 3 months at Boreas beamline (Alba Synchrotron).
- Synchrotron ALBA, Spain. Granted beam time. Co-investigator. June 2014, 2 weeks.
- Synchrotron SOLEIL, France. Granted beam time. Co-investigator. May 2014, 2 weeks.
- Synchrotron SOLEIL, France. Granted beam time. Co-investigator. March 2013, 2 weeks.

Aknowledgements

First of all, I would like to thank Enrique Ortega for giving me the opportunity to do my PhD in the group and also for the support during this time.

I am especially grateful to Maxim Ilin for all his daily help during my PhD. Even in the hardest days, working with him has been really easy and he has been a great guide in all this experience.

I can not forget all the members of the Nanophysics lab. It has been really nice all the help and support. I would like to give thanks also to Fred because all his previous work during the master in nanoscience.

I would like to thank Spanish ministry because of the four years grant which made possible to do my PhD and also the Materials Physics Center for the final support to finish my work.

Last and the most important! Thanks to my family, especially my parents, my friends ("petunias"..) and all the people that supported and encouraged me in the hardest days. Thank you very much!!!